Characterization of Soft Tissue Cutting for Haptic Display: Experiments and Computational Models

A Thesis

Submitted to the Faculty

of

Drexel University

by

Teeranoot Chanthasopeephan

in partial fulfillment of the

requirement for the degree

of

Doctor of Philosophy

May 2006

Acknowledgement

I am deeply grateful to my advisors Dr. Jaydev P. Desai and Dr. Alan C.W. Lau, whom I have learn tremendous amount during the time I was doing my research. Their advice and guidance were invaluable. In addition to that, I would also like to thank the thesis committees Dr. Wei Sun, Dr Bradley Layton, and Dr. Andres Castellanos for their time and their comments which helped improve my thesis. I would like to also acknowledge Dr. Ari Brooks for allowing me to use the C-arm setup for the experiment. Most importantly, I would like to thank the Royal Thai Government scholarship which supported my education since undergraduate and the Link Foundation Fellowship which awarded me during my final year of Ph.D. I would not have got this far without helps and supports from my colleagues in Prism Lab Chris Kennedy, Tie Hu, Greg Tholey, Anand Pillarisetti, James Hing, and Edward Esteager along with Dr. Justin Chandler and Dr. Maxim Pekarev. I thank you all for the friendship and a good time in the lab.

I am in debted for the courage and support I got from my good friends Swisa, Woottiporn, Alisa, Vi, Soraya, and Nite who have always been with me during difficult time. Lastly, my family, I thank them all for their great love. From the bottom of my heart, I thank my parents, my sister, my brother, and my aunt, without them I would not have made it.

Table of Contents

Lists of Tables

Lists of Figures

Abstract

Characterization of Soft Tissue Cutting for Haptic Display: Experiments and Computational Models

Teeranoot Chanthasopeephan
Jaydev P. Desai Ph.D. and Alan C.W. Lau, Ph.D.

Real-time medical simulation for robotic surgery planning and surgery training requires realistic yet computationally fast models of the mechanical behavior of soft tissue. This work presents a study to develop such a model to enable fast haptics display in simulation of soft-tissue cutting. An apparatus was developed and experiments were conducted to generate force-displacement data for cutting of soft tissue such as pig liver. The force-displacement curve of cutting pig liver revealed a characteristic pattern: the overall curve is formed by repeating units consisting of a local deformation segment followed by a local crack-growth segment. The modeling effort reported here focused on characterizing the tissue in the local deformation segment for fast haptic display. The deformation resistance of the tissue was quantified in terms of the local effective modulus (LEM) consistent with experimental force-displacement data. An algorithm was developed to determine LEM by solving an inverse problem with iterative finite element models. To enable faster simulation of cutting of a three-dimensional (3D) liver specimen of naturally varying thickness, three levels of model order reduction were studied. Additionally, the variation of the LEM with cutting speed was determined. The values of LEM decreased as the cutting speed increased. This thesis also includes the characteristic response of soft tissue to the growth of a cut (cracking) with a scalpel blade. The experimentally measured cut-force versus cut-length data was used to determine the soft tissue's resistance to fracture (resistance to crack extension) in scalpel cutting. The resistance to fracture of the soft tissue is defined as the amount of mechanical work needed to cause a cut (crack) to extend for a unit length in a soft-tissue sample of unit thickness. The equipment, method, and model are applicable for all soft tissue.

Finally, the method of determining the property of the pig liver tissue during cutting was verified. Dual C-arm fluoroscopes were used to obtain the motion of the beads embedded inside the specimen during cutting. The experimentally measured displacement field was compared to the displacement field obtained through finite element model based on the LEM values at each localized area.

Chapter 1: Introduction

1.1 Motivation

Surgical simulation and virtual reality in medicine has been widely explored. Just as flight simulator trains pilots, surgical simulation is a potentially useful tool where medical students can first expose themselves to surgery in less stressful and more controlled environment. The simulator allows one to learn and correct their mistakes without negative consequences compared to working on real patients. Due to the risk and costs associated with surgical training, having a realistic simulation is a very convincing solution. The advanced technology in surgical simulation and training methodology encompasses technical skills, judgment and medical decision-making. Computer based real-time surgical simulation is a challenging multidisciplinary problem, it combines advanced software, special hardware such as a force feedback device, along with knowledge in medicine and mathematics.

Modeling the response of a deformable soft tissue during cutting is a fundamental scientific problem, an understanding of which can be used to develop **realistic surgical simulators for providing accurate force feedback to the surgeon during surgical training and simulation for soft-tissue cutting procedures** (such as biopsies, which do not use electrocautery [1, 2] to avoid cellular damage). Scalpel cutting is a fundamental art required of residents in training in surgery. Most commonly scalpel cutting is useful for lower abdominal cutting of the skin to access the internal organs in open procedures such as Caesarean section (C-section) deliveries. Scalpel cutting in such procedures aids in minimizing the regional tissue distortion and destruction and aids in better wound healing and better scar after the incision is closed by either sub-cutaneous sutures or external staples. In particular, we are interested in hepatic (liver) tumor biopsies and simulating the cutting forces for surgical residents. The liver is composed of lobules held together by an extremely fine areolar structure and covered by a serous and a fibrous coat. Tumors appearing in the liver are either primary or secondary tumors.

While electrocautery and ultrasonic dissection are the most preferred approach for cutting in liver surgery, our surgeon collaborators indicate that there are specific circumstances where the use of a scalpel is necessary. One of those specific circumstances is liver biopsies. Cutting with a scalpel allows better identification of margins without cellular distortion (as is caused in electrocautery). The surgeon should have opportunities to practice and familiarize themselves with the complexities of a surgical procedure before operating on patients. As a result, it is necessary to develop models based on actual experimental data.

The goal of this thesis is thus to develop a reality-based model of soft tissue interaction with a cutting blade for real-time or near real-time simulation. In the past, most modeling efforts are focused towards assuming the mechanical properties and developing methods to efficiently solve the tissue simulation problem for robot-assisted surgery / training [3, 4]. The models in the past are spring mass model [5] or hybrid elastic model [6] which require low computation time while trading off tissue behavior complexities and realism. Since soft tissue structure is very complex and nonlinear, modeling a simulation of the deformable tissue for real time update is very challenging. In real time simulation, the graphical update required is at least 30 Hz while the force update should be at least 1000 Hz. Most of the works in literature search are either trading of the expense of the computation time to the realism of the model.

1.2 Solution approach

The main focus of this thesis is to characterize the properties of soft tissue for reality based haptic display specifically cutting soft tissue during surgery. Our goal is thus to develop a model of soft tissue interaction with a cutting blade while working with the liver in particular. In the literature, most modeling efforts are focused towards assuming the mechanical properties and developing methods to efficiently solve the tissue simulation problem for robot-assisted surgery / training.

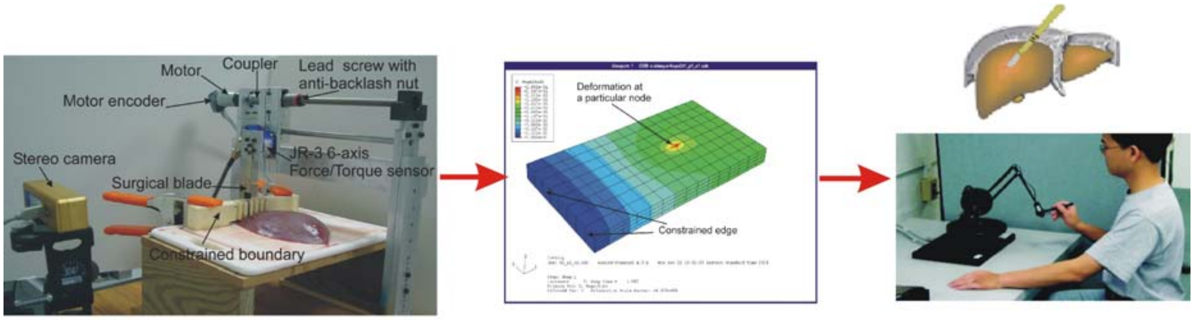

Obtain properties of deformable tissue during experiment

Finite element has been used as a tool to determine force feedback based on the experimentally measured properties

The model can be used for surgical simulation or robot assisted surgery through virtual environment

Figure 1.1: Framework for reality-based modeling of tool-tissue interaction for surgical training and simulation.

Modeling of deformable tissues is critical for providing accurate haptic feedback to the surgeon in common surgical tasks such as grasping, cutting, and dissection. Models constructed through FEM, for example, should be able to accurately represent the surgical task based on the physics of the task. We propose a cutting experiment which helps determine the force and displacement in real time during cutting. The finite element method is used as a tool for an inverse problem to determine the local properties of soft tissue called local effective modulus. The fracture resistance of the liver tissue is determined through the energy balance method. The approach allows fracture analysis with no limitation or any assumptions i.e. nonlinear tissue property or large deformation.

The novelty of our experimental system for measuring the cutting forces is that we are able to measure the cutting forces and the displacement of the blade as it cuts the tissue in real-time. Additionally, the system has three degrees of freedom to facilitate the cutting depth and angle of cut, in addition to the linear travel guide for the cutting mechanism. The cutting equipment is stiff and the cutting blade is attached directly to the force sensor for measuring the cutting forces. The set up is also capable of studying of fracture mechanics of soft biological tissue during tool-tissue interaction between a surgical blade and liver tissue. The tissue toughness is also determined and along with the deformation of soft tissue to the cutting blade, we are able to model the whole cutting process based on the study of tool tissue interaction in both micro and macro scale (local and global).

During a cutting experiment, the force-displacement curve of cutting pig liver revealed a characteristic pattern formed by repeating units consisting of a local deformation segment followed by a local crack-growth segment. The deformation resistance of the tissue was quantified in terms of the local effective modulus (LEM) consistent with experimental force-displacement data. An algorithm was developed to determine LEM by solving an inverse problem with iterative finite element models. To attain fast but realistic force-feedback in real time simulation, we developed techniques for coarse-mesh finite element models while still retaining the realistic overall force displacement behavior through model order reduction techniques. In parallel to the deformation of the liver tissue during cutting process, the fracture or resistance of soft tissue during cutting or crack growth was analyzed. The total work applied externally was applied in the analysis for determination of the fracture resistance of the liver tissue to the cutting blade.

The work in this thesis clearly identifies the correlation between the cutting velocity, cutting angle, and the depth of the blade in the soft-tissue with the cutting forces. Such an analysis can be used to represent the tissue behavior during surgical simulation of the cutting process. The model will provide realistic force-feedback along with graphical update in real-time or near real-time for the surgeon and resident to practice and familiarize their skills before operating on patients. In future work, it is important to include the evaluation of haptic feedback in surgical simulation through an open-loop versus closed-loop haptic feedback. This will involve clinical studies involving resident training with the new surgical simulation system.

1.3 Thesis organization

The thesis chapters are organized as follow:

Chapter 2: The first part of the chapter discusses different approaches in estimating the properties of soft tissue. The second part corresponds to modeling soft tissue for surgical simulation along with graphics-based model and physics-based model are presented. The last part corresponds to the work in fracture mechanics of deformable soft tissue.

Chapter 3: This chapter includes the cutting experiment, the experimental equipment which was used to obtain force and displacement during cutting liver tissue. Matlab image processing toolbox was used to determine the depth of cut analyzed during experiments.

Chapter 4: In this chapter, finite element model was developed as a tool to solve the inverse problem in order to determine the properties of the liver tissue during cutting. In this chapter, 2D plane-stress and plane-strain model and 3D along with different type of element were analyzed. The analysis includes finite element model at Poisson's ratio of 0.3 and 0.5

Chapter 5: In this chapter, we analyzed the effect of cutting speed and cutting angles on the local effective modulus.

Chapter 6: This chapter presents characterizing the fracture resistance of liver tissue (crack growth after tissue deformation) during scalpel cutting. The resistance of soft tissue to the blade or fracture resistance of the liver tissue was determined.

Chapter 7: This chapter presents model verification through displacement field by an experiment in which the fiducial markers were inserted into the liver tissue prior to the cutting experiment. The bead motion was tracked and then was compared to the displacement field obtained from the finite element model.

Chapter 8: This chapter presents the thesis contribution and future work.

Chapter 2: Literature Survey

Modeling of deformable soft tissue for surgical simulation has not been fully explored. The work in this thesis was aimed toward an application in medical simulation. In surgery class for residents, the cost of training with animal tissue or cadaver is very expensive. New technology allows the doctors to practice their surgical skill anytime and anywhere through the use of surgical simulation. The advantage of using surgical simulation over traditional animal lab practice is less risk associated with the animal disease while the user can analyze their performance along with developing a new surgical technique. An example of surgical simulation which has been used widely is simulators minimally invasive surgery where the long narrow surgical instruments are inserted through small incisions and visual feedback is obtained through a rod shaped telescope attached to a camera. With this surgery, the patients' organs are examined with minimal trauma while post operative pain is less –allowing patients to get out of bed sooner and reduce post-procedure morbidity. However, the major issue is the need for surgeons to take special training in performing the many operations that are available by this means. The laparoscopic procedure allows the surgeons to work under two dimensional flat video display instead of three dimensional operating field. The shift requires some practice moving around long laparoscopic instruments while handling patients' organs. Laparoscopy [7] and endoscopic simulations[8] are therefore the most advanced simulations and have been commercialized by Surgical-Science, Mentice, and Immersion to name a few. The simulators have been clinically validated to improve performance in the operating room[9]. Simulators for needle based procedures[10-17] are also studied. The simulators allows user to train the proper techniques for procedures such as needles and catheters. For larger incisions such as open surgery [18, 19], several works are focusing on cutting [20] and suturing [21] simulator for incisions and wounds. The challenges in simulating 3D cutting in surgical simulator is developing physical based tissue model that can estimate the interaction forces along with geometry and topological changes occur during the tool/tissue interaction. In addition, updating the haptic or force feedback in parallel to the graphical update in real time is a challenging problem.

The study of soft tissue cutting has been widely explored using electrocautery [1, 22]. However, electrocautery is useful where it is not important to preserve the surrounding tissue structure and blood cauterization is of primary concern. While there is still a debate about advantages and disadvantages of electrocautery over scalpel cutting, there is limited published work in the literature which has analyzed scalpel cutting in detail. While electrocautery and ultrasonic dissection are the most preferred approach for cutting in liver surgery, our surgeon collaborators indicate that there are specific circumstances where the use of a scalpel is necessary. With tissue ablation, mechanical properties of the tissue also plays significant role[23]. Cutting with a scalpel allows better identification of margins without cellular distortion (as is caused in electrocautery). The liver is composed of lobules held together by an extremely fine areolar structure and covered by a serous and a fibrous coat. Tumors appearing in the liver are either primary or secondary tumors. It is critical that the surgeon does not cut the area around the tumor too deep and too long by applying excessive force (with each cut) as the serous and fibrous coat will rapidly tear leading to excessive bleeding and life threatening conditions. As a result, the surgeon should have opportunities to practice and familiarize themselves with the complexities of a surgical procedure before operating on patients. One of the main challenges in simulating three-dimensional cutting is developing a physically based tissue model that can estimate the interaction forces and dynamically re-form the mesh during a tissue cutting task. Additionally, the model should be able to update geometry and topological changes due to cutting.

Previous work related to the work in this thesis was divided into five parts. The first step toward modeling is to understand the mechanical properties of soft biological tissue along with tool/tissue interaction. The first part involves the study of mechanical properties of soft biological tissue. The second part corresponds to the modeling of soft deformable tissue. The third part is devoted to fracture mechanics in soft tissue. Even though the theory of fracture has been widely explored in the past, fracture mechanics of soft biological tissue has not been investigated. The fourth part focuses on finite element analysis and solving an inverse problem. Finally, the last part of the survey is related to haptic rendering for surgical simulation of soft tissue cutting.

2.1 Mechanical properties of soft tissue

Property of soft biological tissue is very complicated and the mechanical property of the tissue is highly nonlinear. Measuring the properties of the tissue is therefore not a trivial task. Previous works in the past focused toward studying soft tissue stress and strain relationship. Fung [24] extended the animal tissue and explored the properties in term of relationship between stress and strain. Properties of soft tissue has been explored in the past in compression or tension experiments [25, 26]. Constitutive models were established for soft tissue or abdominal organ based on experimental data [27-29]. Brain tissue has been studied by [27, 30] which came up with constitutive model for brain tissue and abdominal organ. Most of the experiments relating to determination of the soft tissue properties are uniaxial extension as well as biaxial extension. An example of which the combined compression and elongation experiments [31] were applied on porcine livers to determined the stress and strain along with Poisson’s ratio. However, no one has explored biological tissues or the effect of cutting on global deformations. Scissors cutting data was gathered for biological tissues by Greenish and Hayward, but not modeled [32]. The most common task during surgery is organ palpation using blunt instruments or palpating probes. The approach found in previous literatures for measuring the soft tissue mechanical properties is the indentation test. Various experiments were tested during the in-vivo [33-36] and ex-vivo [37-39] of the soft tissue. A robotic device along with a force transducer [40-42] was used to obtain the response of soft tissue in intra-abdominal organs including the liver and lower esophagus of pigs during the in-vivo through static and dynamic indentations. Human liver and kidney properties during in-vivo experiments were examined through aspiration experiments [43]. Stress-Strain data was obtained from pig liver and spleen using static compliance probe [44], they studied the Young's modulus of the human liver which appeared to have a mean elastic modulus of about 0.27MPa. Zhang et al [45] performed indentation tests for estimating the effective Young's modulus of soft tissue. An experiment by Kerdok et al [46] took into account the studied of the effects of perfusion on the viscoelastic characteristics of liver tissue. Another noninvasive approach used during an in-vivo measurement of the properties of soft tissue is called elastography. Elastography or the measurement of the elasticity of soft tissue with images such as ultrasound, MRI was studied for a noninvasive and this method also is applicable during the in vivo measurement [47]. MRT is another non-invasive measurement of the local elasticity of the tissue based on the observed wave propagation.

"Global" elastic deformations of real and phantom tissues have been studied extensively in previous work, through simple poking interactions [35, 48-51]. However, these methods are simplistic since they do not take into account the complex boundary conditions that are normally present, both internal to the organ and on the exterior surface. Howe and colleagues [29, 52] developed a "truth cube" for validation of models. There have also been studies on estimating the mechanical properties of the tissue through high-frequency shear deformations of the tissue sample [53], and elastography techniques [54]. A variety of other techniques exist in the literature for estimating viscoelastic characterization of tissues [55, 56] (triaxial measurement device for soft tissue)[57]. Modeling tissue cutting has also been explored to a limited extent. However, there does not exist a standard methodology for modeling cutting. Most of the work in the literature does not involve the physics behind cutting (such as energy exchange) [58, 59]. Resolved-force haptic devices, such as the PHANToM from SensAble Technologies (Woburn, MA), have been used to display external cutting forces of a single blade in surgical procedures [20, 60]. In addition, cutting with scissors has been modeled, without the display of internal cutting forces[4, 32]. However, no one has explored biological tissues or the effect of cutting on global deformations.

Scissors cutting data was gathered for biological tissues by Greenish and Hayward, but it has not been accurately modeled [61, 62]. The integration of local grasping forces measured from real tissues into larger global models has not been studied. Recently, there has been some work on modeling cutting in surgery and also understanding the role of vision and force feedback in grasping tasks [63].

Terzpoulos and Fleischer [64] modeled inelastic deformation for computer graphic application. However, there has been very little work on modeling the cutting process based on observed experimental data. Mahvash and Hayward [65] studied the cutting process in one dimension and applied a fracture mechanics formulation to understand the cutting process. However, they did not quantify the cutting process based on experimental data from soft-tissue cutting.

2.2 Modeling of deformable soft tissue

Modeling of deformable tissues is critical for providing accurate haptic feedback to the surgeon in common surgical tasks such as grasping, cutting, and dissection. Models constructed through FEM, for example, should be able to accurately represent the surgical task based on the physics of the task. Current approaches to modeling deformation of organs are either geometry-based or physics-based. In geometry-based methods, the deformations are purely based on geometric manipulations without considering the dynamic interactions within the object. Significant work in geometry-based models using either the vertex-based approach [66, 67] or spline-based [67-69] approach has been done.

2.2.1 Graphic-based model

In computer aid design and computer graphic, method such as B-splines, rational B-splines, non-uniform B-spines (NURBS) are normally used for modeling of deformable objects.

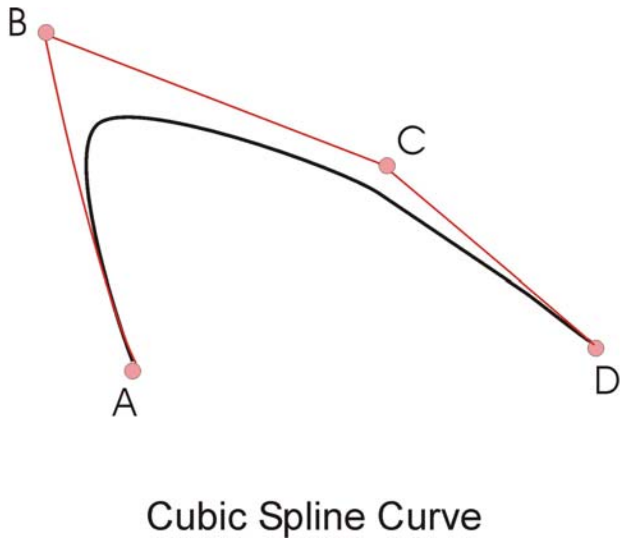

Figure 2.1: Cubic spline curve for geometrical changes

An example is shown in Figure 2.1 cubic spine curve, the curve a and d is edited by control point a, b, c, and d. Moving the control points change the curve in a predictable manner. This method is computationally efficient and supports interactive modification.

Using only graphic modeling is definitely not enough for modeling of an object as complex as human organs for surgical simulation. Physics-based models simulate the physical behavior of objects and involve the internal and external forces.

2.2.2 Physics-based model

Physics based models are computationally more intensive and utilize particle-based schemes [70-72], finite element method [73-76], or meshless methods [77]. However, most of these methods assume a linear elastic model and hence the computations are done offline before the actual simulation begins. Linear elastic models do not represent an accurate model for finite strains; however, it is a good starting point in modeling tissue interaction.

Spring –mass model is a simple and efficient physically-based [69] technique which is widely used for modeling deformable objects. Most of the simulation was done based on linear spring (Hookean). Dynamic spring-mass systems is applied on facial modeling by Terzopoulos and Waters [64]. The model is constructed by layers of mesh of mass points which were connected to each other through springs, while different spring constants were used to model different layers.

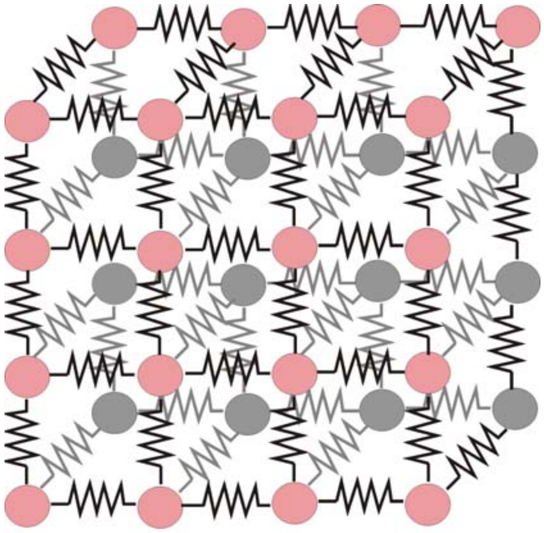

Spring-mass model

Figure 2.2: Spring mass model

Spring-mass model consists of point mass (m) each of them being linked to the neighbor by mass less spring (Figure 2.2). The system is governed by basic Newton's law F=ma, where F is the total force, m is the mass of each point, and a is the acceleration.

The model is feasible for real-time computation during surgical simulation. The drawback of using spring-mass for modeling deformable object is that spring-mass cannot accommodate the continuum of the model. In soft tissue modeling, using spring-mass model basically trades off the realism of the model with the computation time during the simulation. Especially during tool/tissue interaction such as cutting, spring-mass model does not allow topological changes.

2.3 Finite element method

General Finite element method

Finite element method (FEM) is the method in which the object, the continuum, is divided into elements joined at discrete node points. FEM generally is the procedure that reduces the continuous system mathematical model to a discrete idealization that can be solved. Representing the desired function within each element as a finite sum of element interpolation functions or shape functions does the discretization.

The displacement based FEM is derived from minimizing the system potential energy with respect to the material displacement over the object. Finite element method (FEM) [73] had been used as a tool to determine the physical behavior in soft tissue simulation under mechanical constraints. Bro-Nilsen and Cotin et al [3, 78, 79] used 3D volumetric finite element model for surgery simulation. To render the 3D continuum FE model of tetrahedral elements capable for real time simulation, they reduced the order of the model by statically condensing out the internal degree of freedom while keeping only the degree of freedom associated with surface nodes. James and Pai [76] used boundary integral formulation and discretized the geometry with boundary element method (BEM) in real-time simulation of the deformation of linear elastic objects. For linear elastic deformation, the solution can be attained by the superposition of pre-determined response of unit loading (influence functions or Green's functions) and James and Pai implemented this feature with a low order updating algorithm. Zhuang and Canny [80] proposed finite element models to speed up the simulation of the large deformation of 3D objects subject to dynamic and static loads. For static analysis, their model achieved model reduction primarily with the use of a graded mesh consisting of small elements at the exterior but large element in the interior. De and co-workers [77] proposed to use finite spheres method (FSM) as a meshless scheme for real-time medical simulation. The governing equations of elasticity were numerically solved by the method of collocation at the nodal points, which were placed near the surgical tool tip [81].

Zhuang and Canny [80, 82] achieve real-time dynamic simulation through modeling the global deformation using geometrically nonlinear finite element methods. They preprocessing the LU factorization of a small number of large matrices to reduce the time and space required. In the past, people reduce the finite element based computation time by consider only the surface nodes where nodes located inside is relatively insignificant. Bro-Nielsen et al [78, 79] use a condensation technique to reduce the complexity during the linear elastic material analysis.

Method based on stiffness matrix inverse pre-computation [6] cannot be used to simulate soft tissue cutting or tearing performed cutting elastic object using finite element method. In a survey of deformable modeling in computer graphic done by Gibson and Mirtich [83], several reduced method were introduced for less complexity continuum model.

Though FEM allows the change of topology during the deformation, there is a disadvantage of using FEM in real-time simulation. Since the stiffness matrices and the force vectors are computed by integrating over the object and re-evaluated during the deformation, the process is therefore very time consuming. In addition, the linear elastic theory used to derive the potential energy equation applied to small deformation of the objects. Soft biological tissue usually observed as large deformation. By assuming quasi-static analysis, the mass and stiffness matrices remain constant over a single time interval but they are re-evaluated at each time step. Example of inverse approach based [84] on the load/deformation analysis or the pressure/volume relationships [85] to determine the passive material properties was described. They performed experiments to determine the heart material parameters that describe in vivo myocardial material behavior. The inverse problem was solved by adjusting the parameters in FE model until the model predicted strains most closely match the measured strains.

Another method was proposed lately in 20th century called mesh-less method [86]. The method employs particles or point mass instead of elements (Figure 2.3). Meshing a medical image could be very expensive and time consuming. The advantage of using the mesh free method over the finite element method is that mesh free is more robust and uses less computational time.

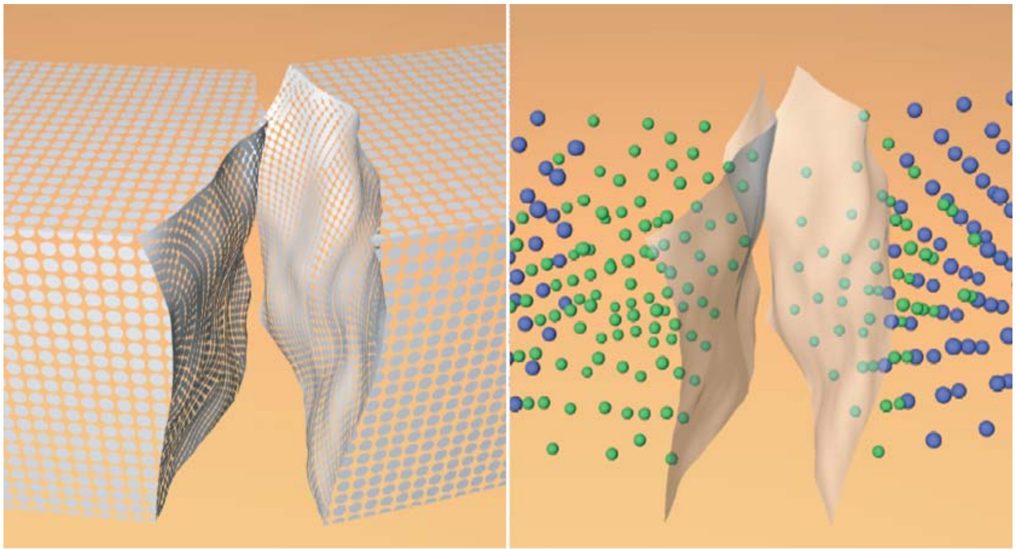

Figure 2.3: Mesh-less method for soft tissue modeling by CO-ME Computer aided and image guided medical interventions ZTH Swiss Federal Institute of Technology Zurich http://co-me.ch/projects/phase2/p09/p09_03.en.html

The computational analysis performed on point nodes without requirement of the connections among the nodes. With no use of element (element distortion), the method allows better non-linear analysis. However, this method only applies to 2D analysis, the 3D analysis is still too complicated.

2.4 Fracture mechanics during soft tissue cutting

Cutting deformable soft tissue such as liver as viewed through force-displacement relationship is a process consists of tissue deformation followed by cutting (crack growth). Since biological tissue has complex structure, understanding the mechanism of the fracture or the crack growth of soft deformable tissue is a real challenge. While property of soft tissue is not uniform and nonlinear, it is crucial to model the mechanical properties or the resistance of soft tissue to the cutting blade during the crack growth of cutting within the local area. In general, fracture can be viewed as the exchange between the external and the internal energy.

Since there is fluid inside the tissue during the cutting process; it is therefore reasonable to neglect friction in this process. In this paper, we describe several tests in the past for testing of fracture toughness.

2.4.1 Introduction to fracture resistance of biological tissue

Property of soft biological tissue is known as highly nonlinear, viscoelastic and incompressible [24]. In non-linear biological tissue such as liver, [38] the deformation of the soft tissue of pig liver was shown to exhibit a nonlinear J-shape relationship between stress and strain. To study the resistance of soft tissue to the blade, one important property of interest is the resistance to fracture (the toughness or resistance to cracking).

Griffith described fracture mechanics as a balance between the external work and the internal strain energy [87]. Three main approaches for fracture mechanics in soft tissue are 1) energy based fracture mechanics and 2) stress intensity factor during fracture, and 3) crack tip opening displacement (CTOD). Eighty percent of the previous work in this field applied energy based method to determine the fracture toughness of soft tissue. Doran et al [88] experimentally measured the resistance to fracture “J” of then biological membrane. They used a simplified model of stress/strain behavior of the tissue where it was assumed that no strain energy was stored in the skin until a certain level of strain was reached. The membrane deformed in front of the blade until cutting occurred. Oyen-Tiesma and Cook [89] determined fracture resistance of cultured neocartilage using energy based method. The experiment was done on cyclic tension tests for notched and un-notched samples. The dissipated energy was calculated through the integration of the area under the load-displacement curve during loading and unloading of each cycle. The amount of energy dissipated due to fracture was determined by the total measured dissipated energy minus the energy dissipated due to viscoelasticity (predicted). Fracture resistance then was calculated from fracture energy per cycle over the thickness times crack-length while viscoelastic work was estimated through the actual load curve and an estimated unload curve. Purslow [90] studied the non-linear elasticity on the toughness of soft tissue measured by tear tests. The test was done on specimens of J-shape stress/strain material such as the mesogloea, rat skin, pig aorta and R-shape stress/strain material which was cooked meat. The nature of load-deformation curve of a tear test appeared to influence the behavior of the fracture. The strain energy stored in the legs of specimen during the tear test was also studied and found to be a critical factor during crack growth.

Kendall and Fuller [91] found that the non-linearity had little influence on certain cracking test such as trouser tear test but the contribution part was instead from fracture surface energy. Mai and Atkins performed a similar test on tear test to study the nonlinear fracture toughness of material. However, they believed that the deformation of the legs before fracture effects the nonlinear stress-strain properties on fracture toughness. On the other hand, the assumption in [91] was that the strain energy stored in the legs of a deformed tear test specimen was insignificant during the fracture process.

With regard to fracture characteristics in cutting of soft tissue, Mai and Atkins [92] performed guillotine cutting in order to study mechanics during cutting with blade. Darvell and co-workers [93] proposed a portable fracture toughness tester using scissors or wedge tests. Mahvash and Hayward presented an analytical method based on fracture mechanics approach to calculate the force obtained during cutting of soft tissue for haptic rendering of cutting. Pereira et al [94] studied fracture mechanics of soft tissue during scissor cutting test. Scissor cutting is different from blade cutting by adding the shear mode into fracture. The energy method was also used to determine the fracture resistance during scissor cutting. The viscoelastic effect was negligible in this case. Ahsan et al [95] used energy based method to study the fracture of biological material. They studied the fracture mechanics of biological material using the (Modified Single Edge Notch) or MSEN. MSEN is a method based on energy required during crack extension. Ahsan et al performed peel test, shear test (Mode II), tear test (Mode III) along with estimated fracture toughness from energy release rates. During the test, the crack analysis was record by video camera and therefore the path of crack propagation is known. Chin-Purcell et al[96] applied two test methods which were MSEN and tear test for the fracture of articular cartilage. One advantage of using MSEN is that fracture process can be viewed under microscope and the Young's modulus and strain energy "G" can be determined. However, there is a difficulty in the method of identifying the critical fracture point. They compared the MSEN method to the trouser tear test. The trouser tear test method allowed fracture analysis for mode III crack growth.

A stress intensity approach for fracture mechanics was also done by Adeeb et al [97]. They studied the fatigue behavior of tendon tissue based on tension testing and cyclic loading experiment. The nonlinearity was negligible along with the fracture process zone at flaw tip. The stress intensity was assumed constant throughout the tendon. The fracture toughness of the tendon was related to its ultimate tensile stress.

Fracture toughness was also determined using a novel micropenetration technique introduced by Simha et al [98]. The toughness of the material (in this experiment cartilage) was the resistance of the tissue to penetration. They defined the toughness as the ratio of the penetration work to one-half of the surface area of a cone with depth pen, the penetration depth. Most of the analyses done were in quasi-static analysis. Viscoelastic or the time dependency plays significant role during fracture, therefore more work need to be done in term of exploring the role of viscoelasticity during crack growth. Large deformation is also another important aspect which has to be taken into consideration because the linear elastic theory does not apply.

2.4.2 Fracture mechanics of biological tissue

Energy based fracture toughness

With the energy based method, the strain energy stored in the specimen is used for crack growth. However, the previous work proposed:

External work = Elastic Potential energy + Irreversible work+ Plastic Potential energy

In 1952, Rivlin and Thomas extended the energy balance concepts of Griffith to tearing of rubbers. Ideally, rubber is nonlinear and therefore the analysis is not dependent on linear elastic theory.

Linear elastic fracture mechanics

Linear elastic fracture associates with the small plastic deformation. The material obeys Hook’s law stress/strain relationship. Atkins and Mai introduced experimental determined fracture toughness in biological tissue such as skin. Tearing and guillotining cutting are proved to be a reversible process. In general case for elastic fracture, the cycle OLMN shows a single loading-->cracking-->unloading cycle. The unloaded displacement is ON =U_r. In this case, cracking takes place along LM.

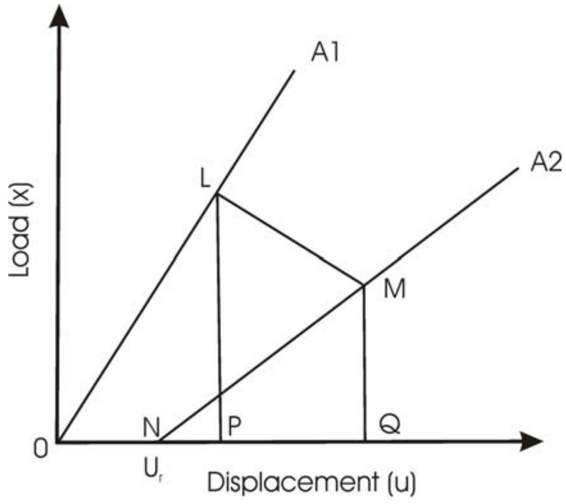

Figure 2.4: The load-displacement of general case elastic fracture

$$\Delta OLMN = \frac{1}{2}X_L u_p + \frac{(X_L + X_M)}{2}(u_Q - u_p) - \frac{1}{2}X_M(u_Q - u_N) \ldots\ldots (2.1)$$

$$\text{compliance} \qquad C_1 = \left(\frac{u}{X}\right)_{A1} \ldots\ldots (2.2)$$

$$C_2 = \left(\frac{u}{X}\right)_{A2} \ldots\ldots (2.3)$$

$$\Delta OLMN = \frac{1}{2}X_1 X_2 (C_2 - C_1) + \left(\frac{X_1 + X_2}{2}\right)u_r \ldots\ldots (2.4)$$

Assume work in the area OLMN is used during fracture:

$$d(OLMN) = \frac{1}{2}X^2 dC + X\,du_r \ldots\ldots (2.5)$$

$$R = G_c = d(OLMN)/dA$$

$$= \frac{1}{2}X^2\, {}^{dC}\!/_{dA} + X\, {}^{du_r}\!/_{dA} \ldots\ldots (2.6)$$

Fracture toughness is R while the elastic strain energy release rate (with respect to crack area). For quasi-static cracking, R = J is measured as the crack growth per unit crack length.

Stress intensity approach

An alternative approach of fracture mechanics is based on stress at point near tip of a crack described by term “stress intensity factor”. When stress field reaches a critical dimension, crack will start growing. The critical dimension is called “fracture toughness”. High stress results in yielding and plastic deformation at crack tip.

The fracture toughness “K_{IC}” can be calculated by: $\sigma_{yy} = \frac{K}{\sqrt{2\pi a}}$

Experimental techniques for determining the geometric stress intensity factor:

1) Photoelastic methods
2) Optical approach through caustics
3) Strain gages
4) Local collocation

5) Interference patterns
6) Moire patterns

Stress intensity factor technique is also based on energy release rate.

Crack tip opening angle (CTOA), crack tip opening displacement (CTOD)

Another geometric analysis for stress/strain during fracture is called crack tip opening angle. CTOA is basically a measure of toughness of material which could be done experimentally through the measure of driving force. Since our specimen (soft tissue) is deformable, it is very complicate and difficult to determine the geometry of the crack angle at the crack tip.

2.5 Haptic rendering for cutting deformable tissue

The *Spring* surgical simulation, real time collaborative performed by Montgomery et al [99], is an example of multi user, multi performance, and networked haptics. The group developed the model for c++ based in both UNIX and window platform.

An important work in the past has been focusing on the deformation technique to simulate cutting in deformable tissue such as ChainMail. Spring and mass model was widely used because the spring was used to represent the potential energy stored before cutting along with releasing the nodes after splitting the cut. Nienhuys et al [100] proposed an iterative algorithm for a linear FE deformation. The method requires less pre-computation along with less matrix updated.

Chapter 3: Cutting experiments

Understanding the mechanical property of the tissue is important for modeling a realistic soft deformable tissue for surgical simulation. In order to study the tool/tissue interaction specifically during surgical cutting, we designed an equipment which is capable of measuring the force and displacement in real time. This section is divided into three parts, namely: 1) design and development of the liver tissue cutting equipment, 2) experimental procedure for measuring the liver cutting forces and 3) determination of depth of cut by image processing.

3.1 Design and development of the liver tissue cutting equipment

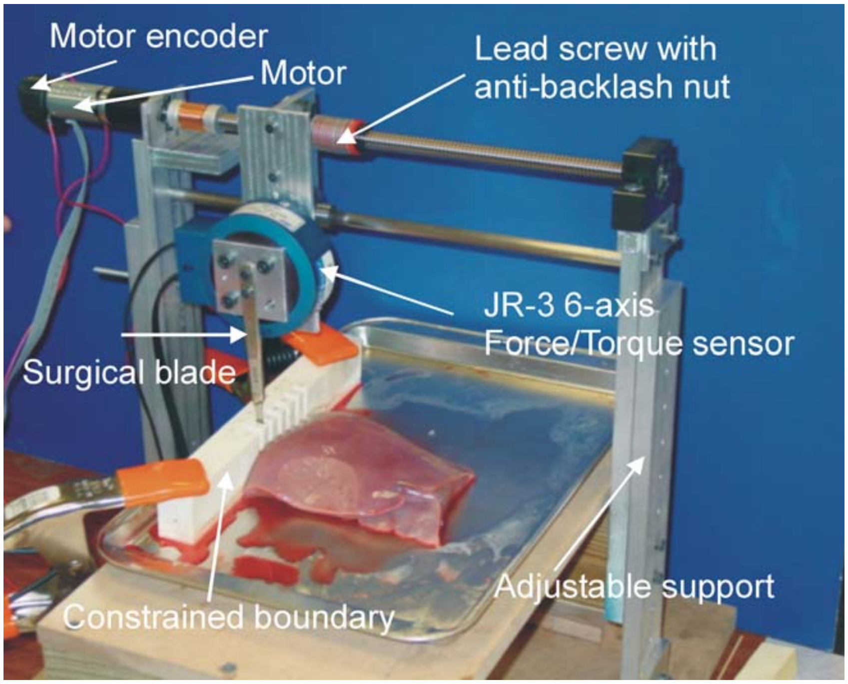

Figure 3.1: Experimental setup for measuring the cutting forces in the pig liver.

The equipment consists of a scalpel-blade cutting subsystem, a computer control subsystem, a digital data-acquisition subsystem, and a data post-processing subsystem (see Figure 3.1). The test equipment to measure the liver cutting forces was designed to have multiple capabilities such as: a) varying the angle of cutting the liver (the machine allows the angle variation from zero to ±90 degrees), b) adjust the height of the scalpel by moving the cutting mechanism over a vertical column to control the depth of cut (the vertical supports can be adjusted in the range of 30 to 50 cms from the base), and c) variable cutting speed to measure the effect of cutting speed on cutting forces and strain rates within the specimen. In our experimental setup, we can vary the speed from 0 to 3.81cm/sec, however all our experiments were done by varying the speed from 0 to 2.54cm/sec. We have analyzed the data for the cutting force vs. the displacement from the fixed end of the constrained boundary of the specimen (see Figure 3.1). The constrained boundary shown in the figure was designed to simulate the attachment of the liver on one end as in a human body (such as the attachment to the diaphragm). The entire cutting mechanism consists of two vertical supports, a lead screw assembly with a geared DC motor and an incremental encoder (manufactured by Maxon Motors, model A-max32 with planetary gearhead GP 32C and digital encoder HEDL 55 with line driver RS 422), and a JR3 precision 6-axis force/torque sensor (model 85M35A-I40, with worst case resolution of 0.05 N in Fx and Fy, 0.1 N in Fz and 0.00315 Nm in Tx, Ty and Tz) to which a surgeon's scalpel is attached. We use the number 10 Bard-Parker stainless steel surgical blade in our experimental studies, consistent with what is used by surgeons. The cutting blade traverses linearly based on the rotary motion of the DC motor. An anti-backlash nut connects the lead screw to the force sensor. The purpose of the anti-backlash nut was primarily to connect the vertical force sensor assembly to the lead screw, while a coupler connects the output of the planetary gearhead to the lead screw. The scalpel is screwed to the force sensor and the force sensor is mounted on an aluminum plate with one end attached to the anti-backlash nut traveling along the lead screw and the other end on a lower guiding shaft (parallel to the lead screw) with a linear bearing to provide low friction linear travel. The entire assembly has been designed to provide 20cm of travel distance for cutting the liver specimen. The design and construction of the cutting assembly ensures that the system is sufficiently rigid with no backlash so that the forces recorded by the force sensor are those obtained by cutting the tissue alone. The dSPACE DS1103 controller board (manufactured by dSPACE, Inc.) records the position and force data from the motor's encoder and force sensor in real-time. We have implemented a proportional + derivative (PD) controller to enable precise movement of the motor (and hence the cutting blade during cutting tasks).

3.2 Experimental procedure for measuring liver cutting forces

Since the experiment is performed on ex-vivo liver tissue, the preparation of the tissue before the experiment helps maintain the properties of the tissue as close as possible to the in-vivo properties. To maintain the properties, we transported the liver from freshly slaughtered pigs to our laboratory within 2 hours post mortem. During the experimental setup, the liver was placed on a bed of saline soaked gauze, sprayed with saline and sealed in a container. The saline solution was prepared at room temperature. The liver tissue sample was not preconditioned because in surgery, the cutting forces experienced by the surgeon are on non-preconditioned tissues.

Before starting the experiment, we cut the pig's liver into specimens of size 8x12x2.5 cm. The outer encapsulated surface was not cut since we were interested in measuring the cutting forces on the liver. The outer rim of the specimen was covered with petroleum jelly to minimize moisture loss during the experiment. A bar of rectangular shape made of machineable plastic with an array of small nails clamped at the bottom end penetrated through one edge of the liver specimen to simulate a single constrained boundary surface. While this is not an exact replication of the boundary conditions for a human liver (which is partially attached on one end to the diaphragm) this is none-the-less a valid simplification for our initial tests and model (based on our discussions with surgeon collaborators).

3.3 Results

We conducted several experiments to confirm the capability of our liver tissue cutting equipment. The velocity of the cutting blade ranged from: 0 to 2.54cm/sec. We performed three sets of experiments, one at low cutting speed (0.1cm/sec) to estimate the quasi-static properties, the second set at intermediate cutting speed of 1.27cm/sec and the last set at normal speed cutting (2.54cm/sec) to simulate realistic cutting of the liver tissue in actual biopsy. In each cutting speed, we captured the force vs. displacement data and used this data to determine the local effective modulus for the specimen. Based on the estimated local effective modulus values, we also studied the effect of the cutting speed on the local effective modulus. Each liver sample (size of 8x12x2.5 cm) could accommodate four parallel cutting lines. We were interested in studying the changes in the liver's properties during the interaction with the cutting blade at various cutting speeds.

3.3.1 Experiment 1:

To definitely conclude that the controller was working satisfactorily and that the cutting forces are those due to cutting the tissue alone, we monitored the actual velocity profile of the surgical blade during the cutting of the liver tissue. The actual velocity profile for each trial of cutting shows constant velocity, consistent with that of the desired velocity. This verifies: a) the controller works satisfactorily, b) the stiffness of the cutting machine is significantly larger than the stiffness of the liver sample, and c) the motor drive is sufficiently powerful. Figure 3.2 shows the plot of desired and actual velocity of the cutting blade. Based on the figure, we can conclude that the cutting forces obtained during the experiment are indeed those arising from the interaction forces of the blade with the liver specimen and that the recorded cutting forces are not reduced by the compliance of the structure on which the cutting equipment is positioned.

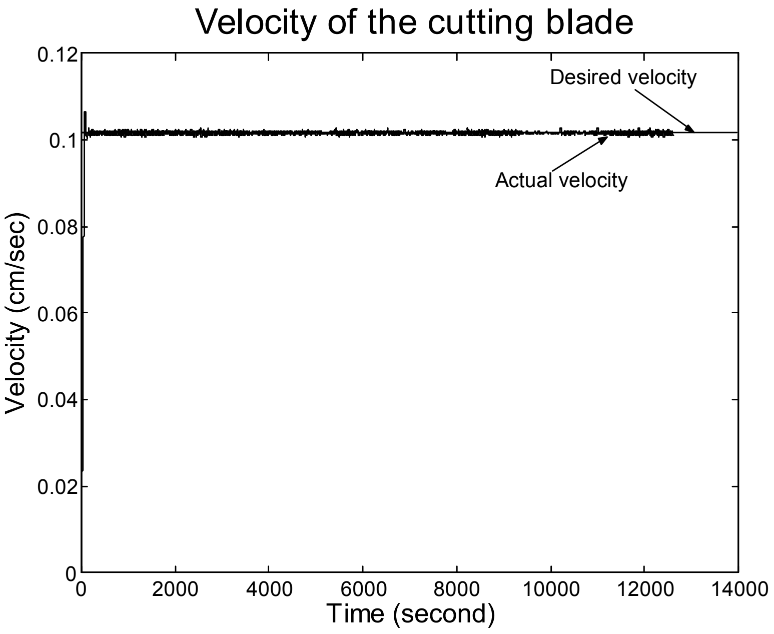

Figure 3.2: Plot of the desired and actual velocity of the cutting blade during the liver cutting experiment.

3.3.2 Experiment 2:

During the cutting process, we captured the data of force vs. distance from the constrained boundary of the liver tissue. The cutting blade was programmed to move at constant velocity for the travel distance of 12cm. We used the JR3 force sensor to measure the X, Y, and Z components of the cutting force and the norm of these forces was plotted versus the displacement of the cutting blade for speeds of 0.1cm/sec, 1.27cm/sec, and 2.54cm/sec (Figure 3.3a-c). We conducted 12 liver cutting experiments for each of the cutting speed. In each set, we used 3 liver samples and each sample was cut into 4 stripes spaced approximately 2cm apart. Our experimental data revealed that the cutting path appeared to be formed by a repeated sequence of localized deformation followed by localized fracture (onset of localized crack growth). The measured force versus cut-length (distance traveled by the cutting blade, starting from the constrained boundary) curves were repeatable in the way that it started from small force during tissue deformation and increased to a higher force as impending localized fracture was about to take place. Then the force suddenly dropped as onset of localized crack extension occurred. Each visually observed localized blade cut on the tissue clearly corresponded to a sudden drop of the force measured by the force sensor. A filtering procedure was developed to post-process the data to produce a force versus cut-length curve clearly illustrating the “hilltops” and “valleys” of the sequence of localized loading and unloading in the tissue specimen during cutting (Figure 3.4).

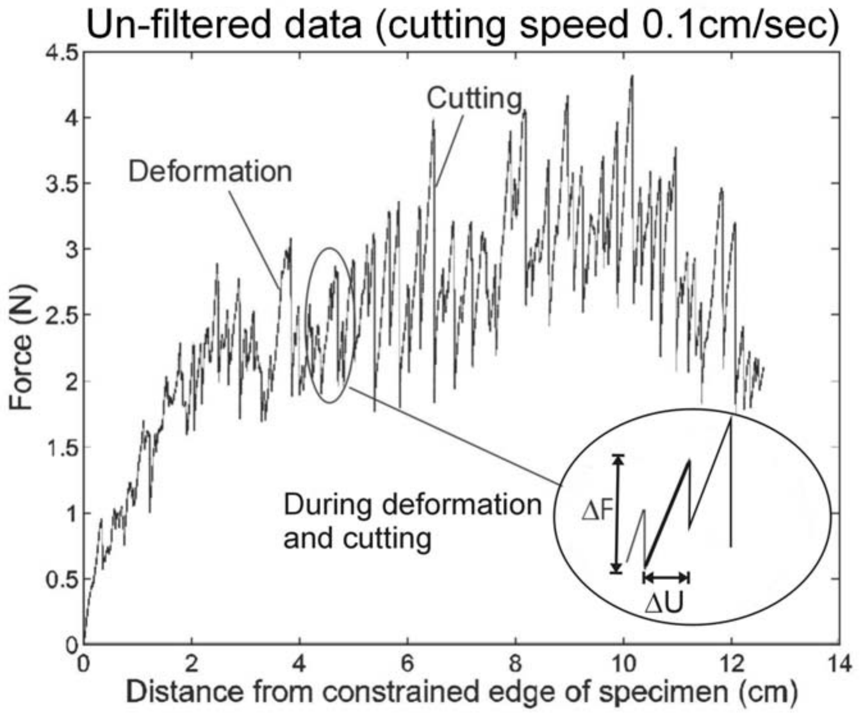

Figure 3.3-A: Experimental data from liver cutting at 0.1cm/sec cutting speed.

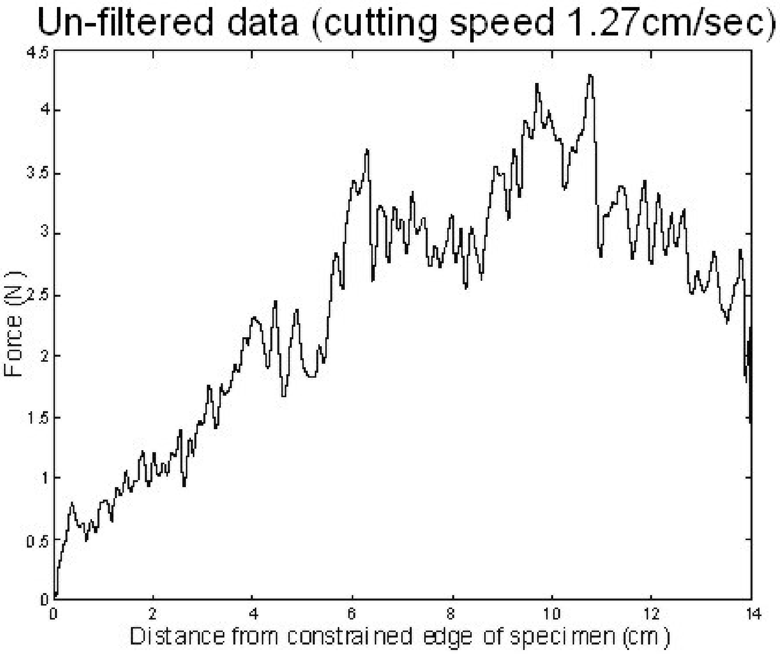

Figure 3.3-B: Experimental data from liver cutting at 1.27cm/sec cutting speed.

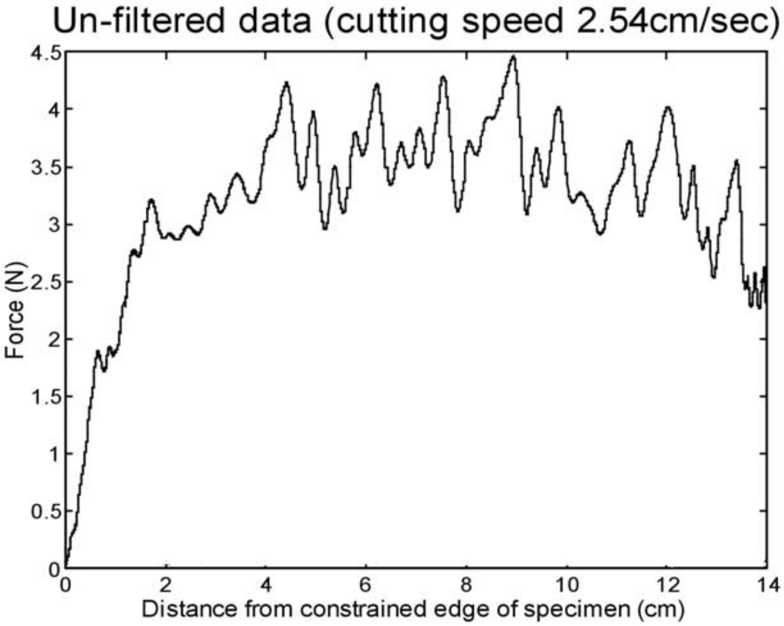

Figure 3.3-C: Experimental data from liver cutting at 2.54cm/sec cutting speed.

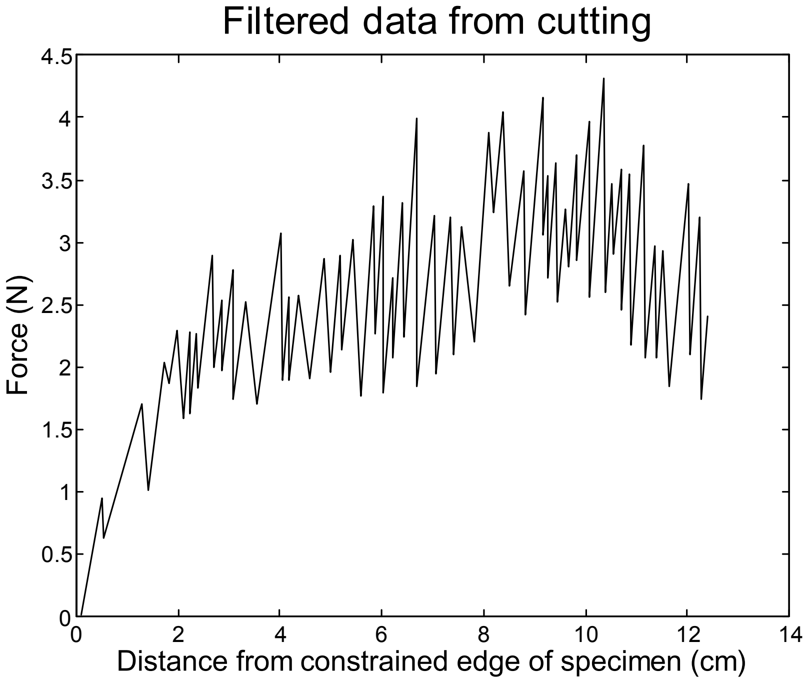

Figure 3.4: Filtered data from liver cutting to identify the significant localized deformation regions. The localized cut occurs at the peak of each localized deformation.

As seen from Figures 3.3-a, 3.3-b, and 3.3-c, there is a rise in the cutting force as the cut-length (distance from the constrained boundary) increased. We also observed more loading and unloading process in quasi-static cutting (Figure 3.3-a), compared to intermediate and normal speed cutting (Figures 3.3-b and 3.3-c). All the liver samples had a characteristic bulge, which lead to more liver tissue being encountered by the blade as the cutting progressed (see liver sample in Figure 3.1). It is important to note that the liver specimens were not cut into exact right parallelepipeds because we wanted to preserve the capsule of the liver during the cutting process. Our hypothesis was that the magnitude of the cutting force directly correlated to the depth of cut. However, we have yet to prove this claim through construction of a testing system, which can monitor the depth of the blade in the liver specimen during the cutting process.

It is desirable to construct a predictive computational model that can simulate the cutting process and predict the mechanical response (cutting force versus cutting-blade displacement characteristics) of liver cutting. To be of real-time application, this predictive model should not be computationally intensive. Since the thickness of the liver specimen in the cutting experiments was much smaller than its other dimensions, it was appropriate to consider a two-dimensional plane-stress finite element (FE) model. In addition, since hepatic cells are more or less of spheroidal form with sizes varying from 1/1000 to 1/2000 of an inch in diameter [101], we were therefore focusing on the mechanical properties of the liver on a macro scale. The mechanical response we measured is the volume average of the response from the liver microstructure. Hence, the analysis presented in the paper is for normal cutting tasks and not to model the cutting phenomenon on a microscopic scale.

As discussed before, the cutting force versus cut-length data showed many repeating segments of localized monotonic loading deformation followed by sudden unloading during liver cutting. During each of the localized loading deformation segment, the cutting force increases linearly with the displacement of the cutting blade (see Figures 3-a, 3-b and 3-c). A good simulation model should be able to predict this localized linear response consistent with the experimental observations. To simulate the cutting process in a computationally efficient manner, our goal was to use as coarse FEM mesh during virtual simulation of cutting, but still be able to predict the actual force-displacement response measured in the experiments. This was accomplished by determining the local effective macro material properties that is self-consistent with experimental data and the FEM model. The elastic modulus of a biological tissue is not constant and it can vary from location to location [102]. To simulate each of the linear monotonic loading segments (see Figure 3.3-a insert for example), we conducted linear elastic FEM analysis with Poisson's ratio 0.3 and an initial local effective modulus of arbitrary magnitude E_1. Then we applied the experimentally-measured ΔU^{exp} (see insert of Figure 3.3-a) of that loading segment to the FEM node that models the cutting blade. We performed the FEM analysis and compared the FEM computed force ΔF^{FEM} of that node to the experimentally measured ΔF^{EXP}.

In the first iteration, ΔF^{FEM} will not be equal to ΔF^{EXP}, and we systematically updated the new value of the local effective modulus to E_2 and repeated the process, until ΔF^{FEM} of the new iteration was within the neighborhood of the experimentally measured ΔF^{EXP}. The final E value so determined is the local effective modulus, $E^{effective}$. We systematically iterated $E^{effective}$ by:

$$E_{i+1} = E_i \left(\frac{\Delta F^{EXP}}{\Delta F^{FEM}}\right) \qquad \text{for } i = 1,2,..... \qquad (3.1)$$

The iteration convergence criterion was:

$$\frac{\left\| \Delta F^{FEM} - \Delta F^{EXP} \right\|}{\Delta F^{EXP}} \le 0.01 \qquad (3.2)$$

This iteration procedure is schematically shown in Figure 3.5. Subsequently, we formed an FEM mesh of the liver, assigned the elements in the FEM model with their respective $E^{effective}$ and used that FEM model to virtually simulate various patterns of liver cutting. Such an FEM model embedded with self-consistent modulus would be able to predict a cutting-force versus cut-length characteristics in each of the monotonic loading segments consistent with experimentally-measured values, should actual experiment of that particular cutting pattern be performed.

A plane-stress FEM model is most appropriate for simulating the cutting of thin liver specimens in which the through-thickness stress is negligible. To cover the range of liver thickness in actual operation, we also conducted analyses with plane-strain FEM models. A plane-strain FEM model is most appropriate for very thick liver specimens in which the through-thickness strain can be idealized as negligible. Finite element results from both plane-stress model and a plane-strain model will bracket the actual mechanical response of liver specimens with varying thicknesses.

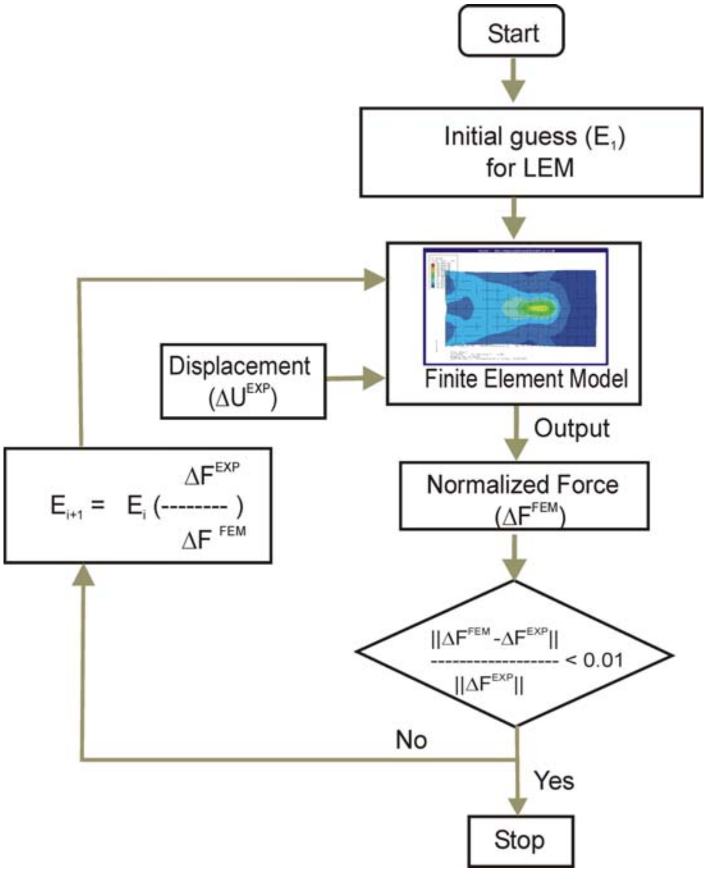

Figure 3.5: Flow chart for determining the local effective modulus.

In Figure 3.6, we show sample local monotonic loading segments that we used in estimating the local effective modulus for the specimen. Based on the procedure outline above, and also summarized in Figure 3.5, the results for the local effective modulus for a typical liver cutting experiment are shown in Figure 3.7 as the cutting progresses. It depicts the effective modulus computed from local deformation data measured at different distances from the constrained boundary. Figure 3.7 presents the local effective modulus based on plane-stress and plane-strain FEM model. At each location, the modulus values derived from plane stress and plane strain models were very close to each other. As a result, it is reasonable to expect that if a more complicated three-dimensional FEM model featuring the exact thickness of the liver is used, its computed modulus will be of very similar magnitude as those determined by our two dimensional FEM models. Figure 3.8 shows a plot of the average local effective modulus at a given cutting speed as four cuts are made on the same liver sample. As seen from the figure the local effective modulus estimated by plane stress and plane strain analysis were within reasonable bounds.

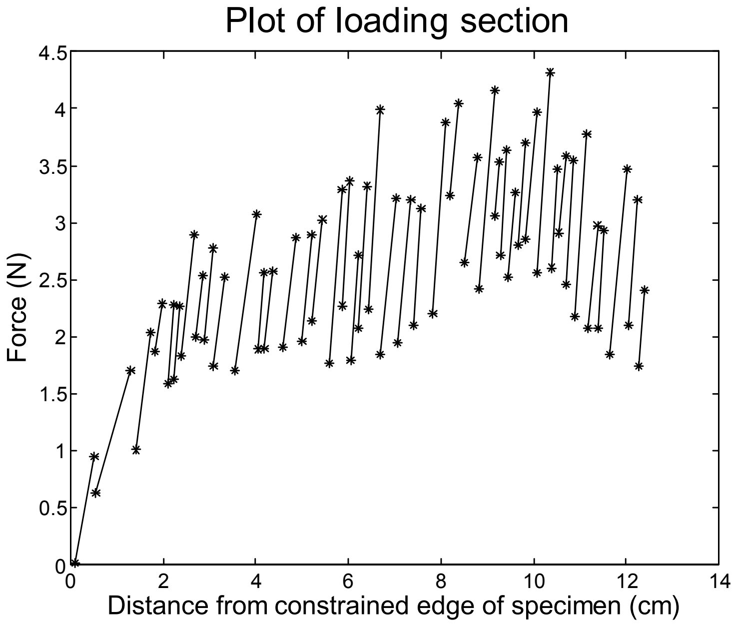

Figure 3.6: Loading segments during cutting showing linear monotonic deformation.

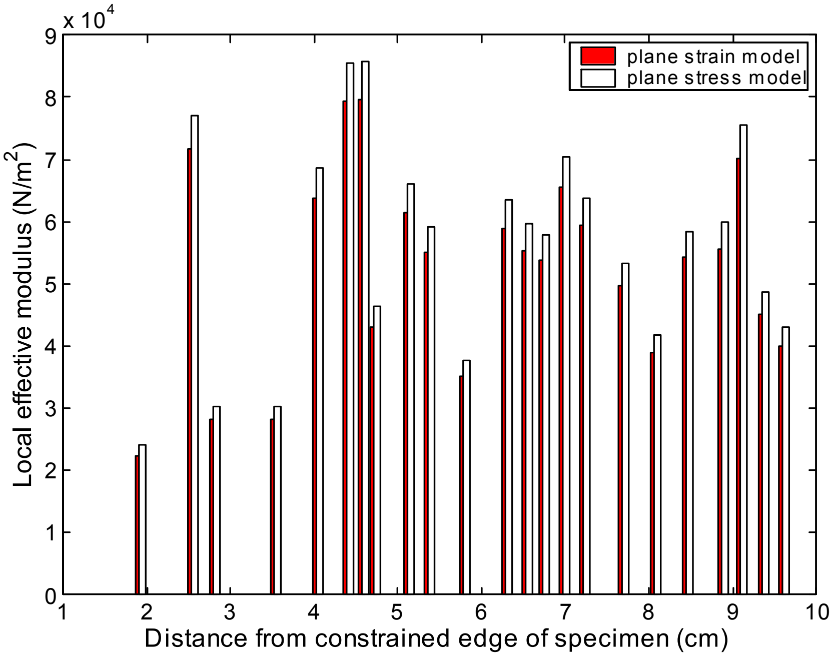

Figure 3.7: Local effective modulus for the loading segments for a typical cut (plane stress and plane strain analysis).

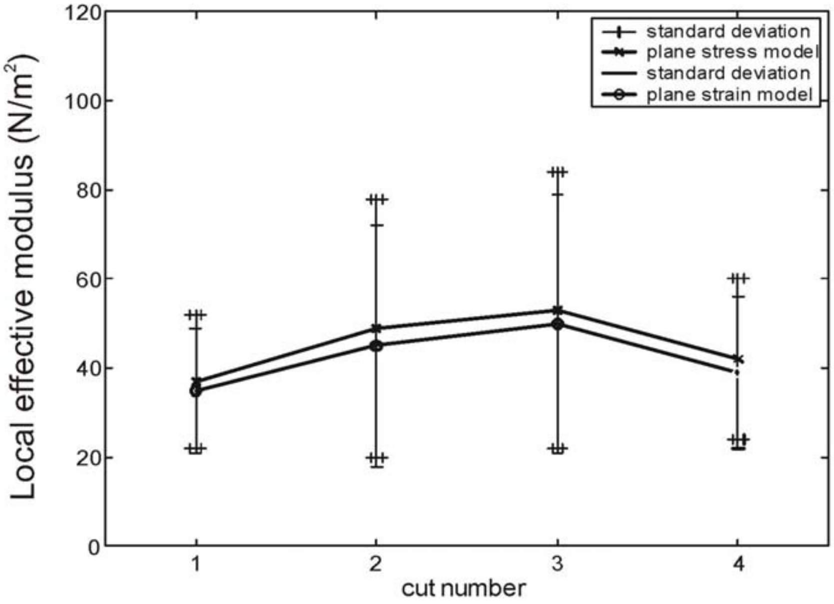

Figure 3.8: Local effective modulus in four cuts for a typical liver specimen.

3.4 Determine the depth of cut and evaluate the normalized local effective modulus

To enable estimation of the depth of the blade embedded in the tissue, a Bumblebee stereo camera system (manufactured by Point Grey Research) utilizing two Sony ICX204 1/3" CCDs with 1024x768 pixels, 10 bit A/D, and maximum of 15 frames per second was used. The camera system is placed close to the experimental setup to capture the image of the cutting blade and the tissue as the cutting progresses (Figure 3.9). Digital image processing was used to determine the depth of the blade embedded in the tissue at each instant of the cutting history.

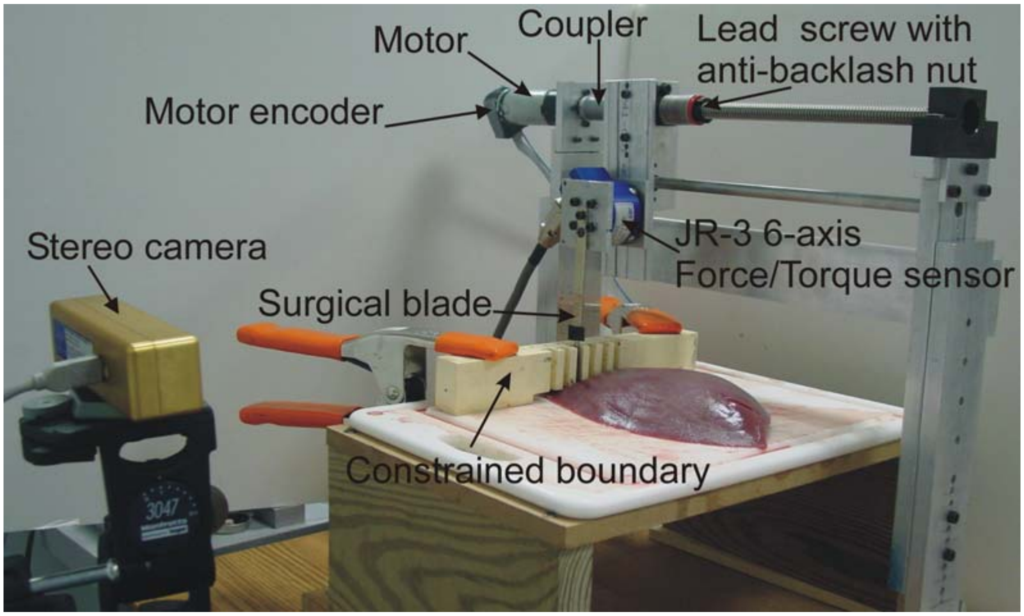

Figure 3.9: Experimental setup for measuring the cutting forces and the depth of cut during liver cutting.

3.4.1 Determination of the depth of cut

All the liver samples had a natural bulge in the thickness direction, which lead to more liver tissue being encountered by the blade as the cutting progressed. The depth of cut played a significant role in the magnitude of the cutting force acting on the blade. In this part, we used image-processing techniques to determine the depth of the blade embedded inside the liver specimen during each instant of the cutting process. We used the Bumblebee system to capture the image of the cutting blade as it cut the tissue. The images were analyzed offline using Matlab 6.5 with the image processing toolbox.

We used the edge detection algorithm to outline the surface of the liver in the imaging window (Figure 3.10). As the images were acquired, we used offline techniques to estimate the distance from the marker black strip to the edge of the top surface of the liver (the exposed blade length) as shown in Figure 3.11. Edges are very important to any vision system. It is a boundary between two dissimilar regions in an image. We found that the process is fairly cheap to compute and it provides strong visual clues that identify the different surfaces of objects. However there is a drawback of using edge detection; edges are usually affected by noise present in the image.

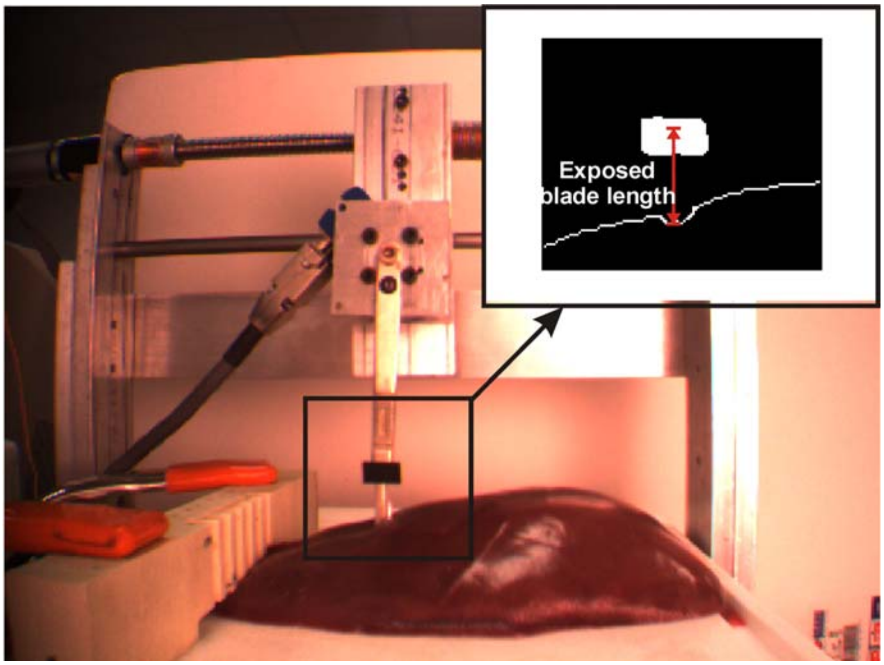

Figure 3.10: Snapshot from the stereo camera.

Many edge extraction techniques can be broken up into two distinct phases:

- Finding pixels in the image where edges are likely to occur by looking for discontinuities in gradients. Candidate points for edges in the image are usually referred to as *edge points*, *edge pixels*, or *edgels*.

- Linking these edge points in some way to produce descriptions of edges in terms of lines, curves *etc.*

In our experimental setup, the distance from the center of the marker black strip to the end of the blade) is 4.25 cm (total blade length). The difference in the total length of the blade and the exposed length of the blade provided us with the depth of the blade embedded in the tissue (Depth of cut = Embedded blade length = Total blade length – Exposed blade length).

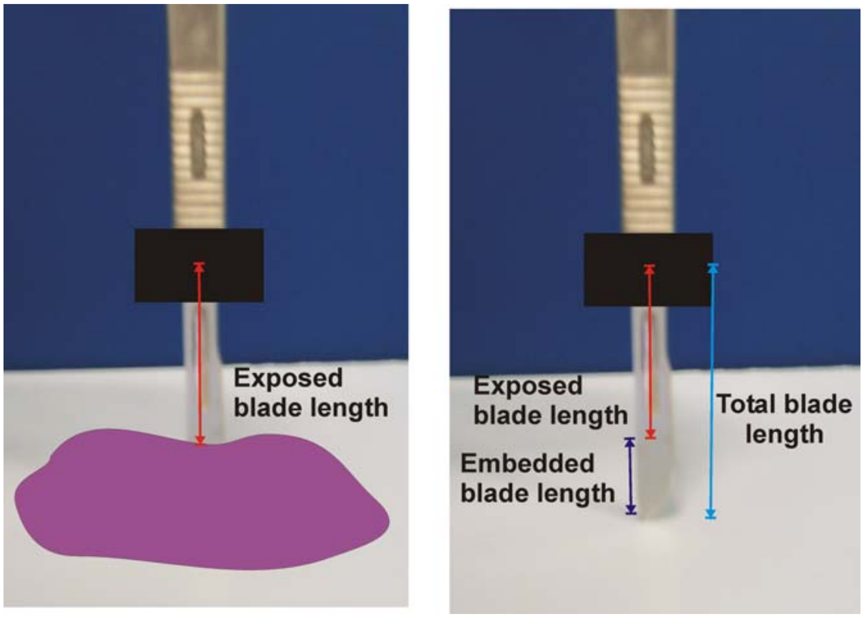

Figure 3.11: Determination of the depth of cut using image processing.

The force and displacement profile during a particular cut is shown in Figure 3.12 along with the depth of cut profile. The normalized force (Force per unit depth of cut) and displacement was therefore used in order to eliminate the influence of the depth of cut to the cutting force.

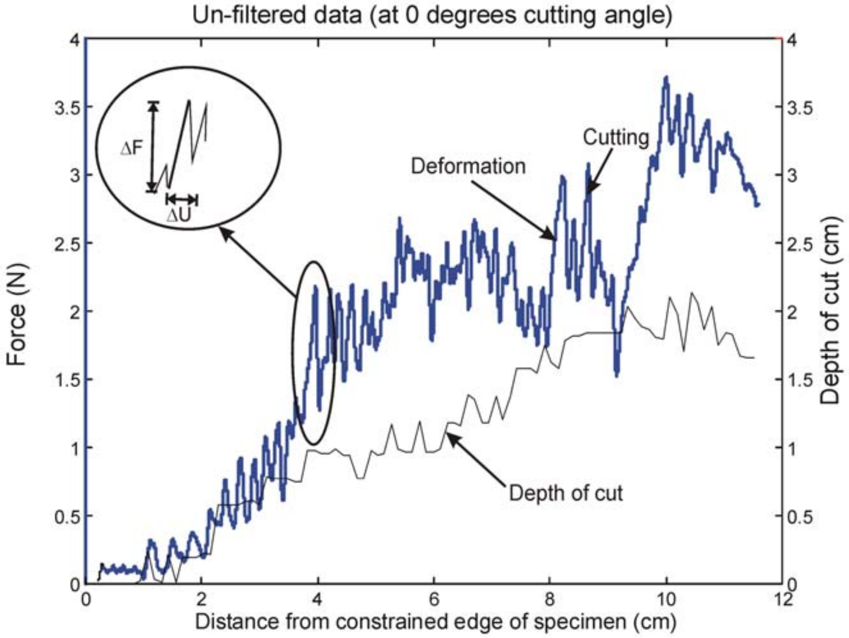

Figure 3.12: Un-filtered data and depth of cut profile.

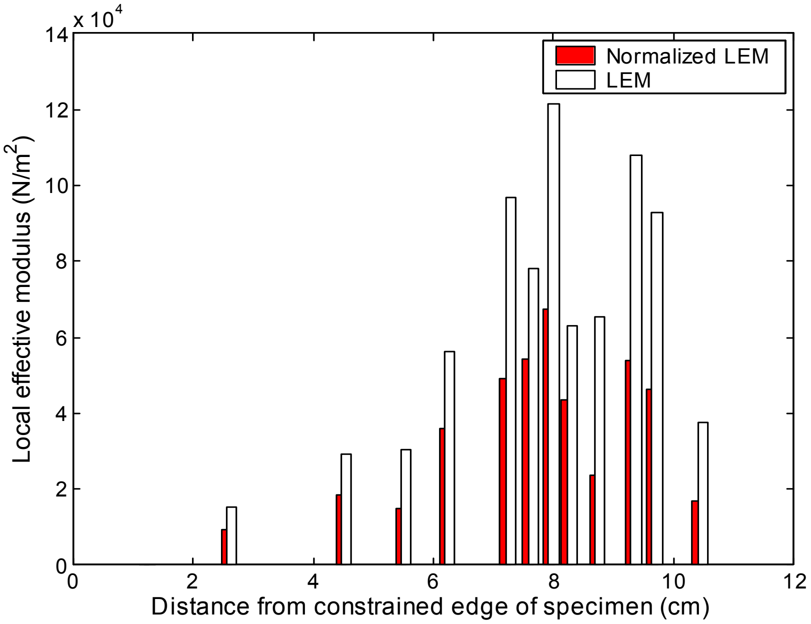

Figure 3.13: The comparison between local effective modulus determined base on normalized cutting force and the LEM determined based on regular cutting force at a particular cutting path

In Figure 3.13, the LEM vales were compared to the normalized LEM values. These two LEM values could be used during the tissue simulation in different way. The normalized LEM could be used to scale up the force feedback when the depth of cut is known while the normal LEM could be applied when the depth of cut is unknown. The force feedback provided based on the normal LEM would represent the force feedback which one would obtained from cutting a non-uniform liver specimen or liver organ with an unknown depth.

3.5 Discussion

In this chapter, the experimental setup and the method which was used to determine the local property during tissue deformation was presented. From the past literature in tissue biomechanics, many living tissues are nonlinear and inhomogeneous. Our apparatus and the post-processing method are tailored to determine the *local* mechanical properties in the liver specimen. The *local* effective modulus at a point in the liver is a measure of the liver's resistance to deformation at that *location.* As the cutting blade moves from location to location during a cut, a continuous stream of data is sampled. By examining the variation of the *local* mechanical properties in the liver specimen from location to location, one can sense the variation of the material heterogeneity in the tissue. This phenomenological measure of the apparent resistance to deformation lumps the overall effects of complex physical mechanisms of tissue deformation encountered by the cutting blade. It would be ideal if we can seek model the details of anisotropic elastic and visco-elastic responses, with time varying frictional-sliding contact, and incorporating locally large strains at tool-tissue interaction points (surface) and other physical mechanisms occurring in the soft tissue cutting process. However, with the current state of limited knowledge, it is prudent to proceed to build up one block at a time. At this stage, what we have done is used the effective measure of apparent deformation resistance, the LEM, as a vehicle to enable using simple elastic finite element analysis to capture and reproduce the experimentally measured overall force-displacement characteristics caused by complex mechanisms.

A modular liver tissue cutting apparatus was designed and developed to perform scalpel cutting of liver tissue and accurately record the liver tissue cutting forces and the motion of the cutting blade. Results from our experiments confirmed that all subsystems were functioning satisfactorily and that the integrated cutting system was significantly stiffer than the tissue specimen. The equipment was capable of measuring with high fidelity the intrinsic cutting forces versus the cut-length of the tissue specimen. The macroscopic force-displacement curve showed repeating self-similar units of localized loading followed by sudden unloading during the onset of each localized fracture. The modulus computed locally was used in the finite element model for simulating the deformation occurring prior to the intermittent cutting of liver. The values for the local effective modulus obtained under plane stress and plane strain analyses were very close to each other for a given cutting speed.

Our result shows that the depth of cut plays a significant role in the cutting forces. Using stereo camera system and image processing, is an effect way to measure the depth of the blade in the tissue as the cutting progress. The force-displacement data reveal that the cutting process consists of a sequence of repeating units each comprising of a localized deformation phase followed by localized crack extension phase in the tissue. The deformation resistance of the tissue during the localized deformation phases can be characterized by the local effective modulus (LEM) of the soft tissue.

Chapter 4: Finite element model analysis

In this chapter, we studied model order reduction during finite element analysis. Finite element was used as a tool to determine the properties of soft deformable tissue through solving an inverse problem. To have faster simulation yet have realistic force feedback, our goal is to use model order reduction to simplify the internal complexity of the model and simultaneously preserve the overall input-output (displacement-force) behavior. The realistic force feedback part is attained via using LEM. The speed of the simulation depends on how much order reduction the model can attain. We studied three levels of model order reduction.

We used three model order reduction which are 2D quadratic, 2D linear, and 3D quadratic element (Figure 4.1) to perform analysis in order to determine the local effective modulus (LEM).

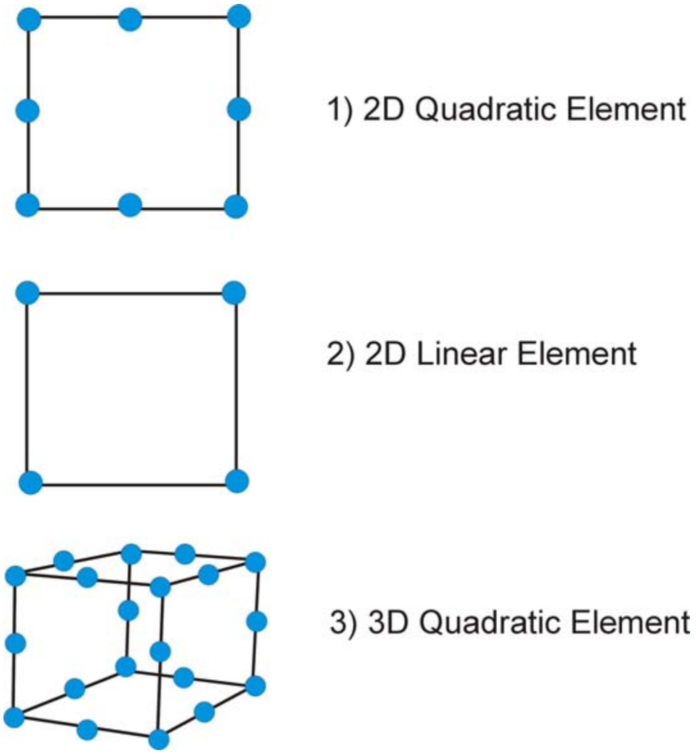

Figure 4.1: Serendipity element for finite element model

4.1 3D quadratic-element model with unit thickness

The common way to construct a 3D model of the liver is to generate a 3D continuum shape reflecting the actual shape of the liver and discretize the geometry into continuum elements. To provide haptic feedback in surgery simulation, it is most important that the surgeon trainee receive accurate force feedback and also sees the instantaneous length of the cut. It is less important to see the actual thickness of the liver. We can thus simplify the general 3D model into a 3D model with unit thickness, and use LEM derived from thickness-normalized ΔF^{exp}. Figure 4.2a shows such a model. The size of the specimen was 8 cm x 15cm while the element size was 1 cm x 1cm x 0.25cm. The model consists of 8 elements in the width dimension, 15 elements in the length dimension, and 4 elements in the thickness dimension. The 480-element model is constructed with quadratic continuum elements (20-node brick elements of the Serendipity family of isoperimetric elements). The displacements can vary quadratically, and strain and stress can vary linearly, in each element. The cutting path with the “tied” double nodes (section 3) along the cut plane (the plane along which the scalpel with travel in the liver) is along the center line. There are four columns of elements to its left of the cutting path and four columns of elements to its right. This mesh has 2830 nodes and 8490 degrees of freedom (8490 equations).

During the simulation of the cutting process, the tied nodes on the cutting path were untied once the cut already occurred. Since the model should replicate the behavior of the liver during cutting as much as possible, the un-tied nodes were constrained to move along the axis so that the two cut parts would not overlap. At the leading edge, the model was constrained by fixed nodes along the edge. The constraints were intended to replicate how we constrained the liver specimen during cutting experiment through the nails array clamped at the leading edge.

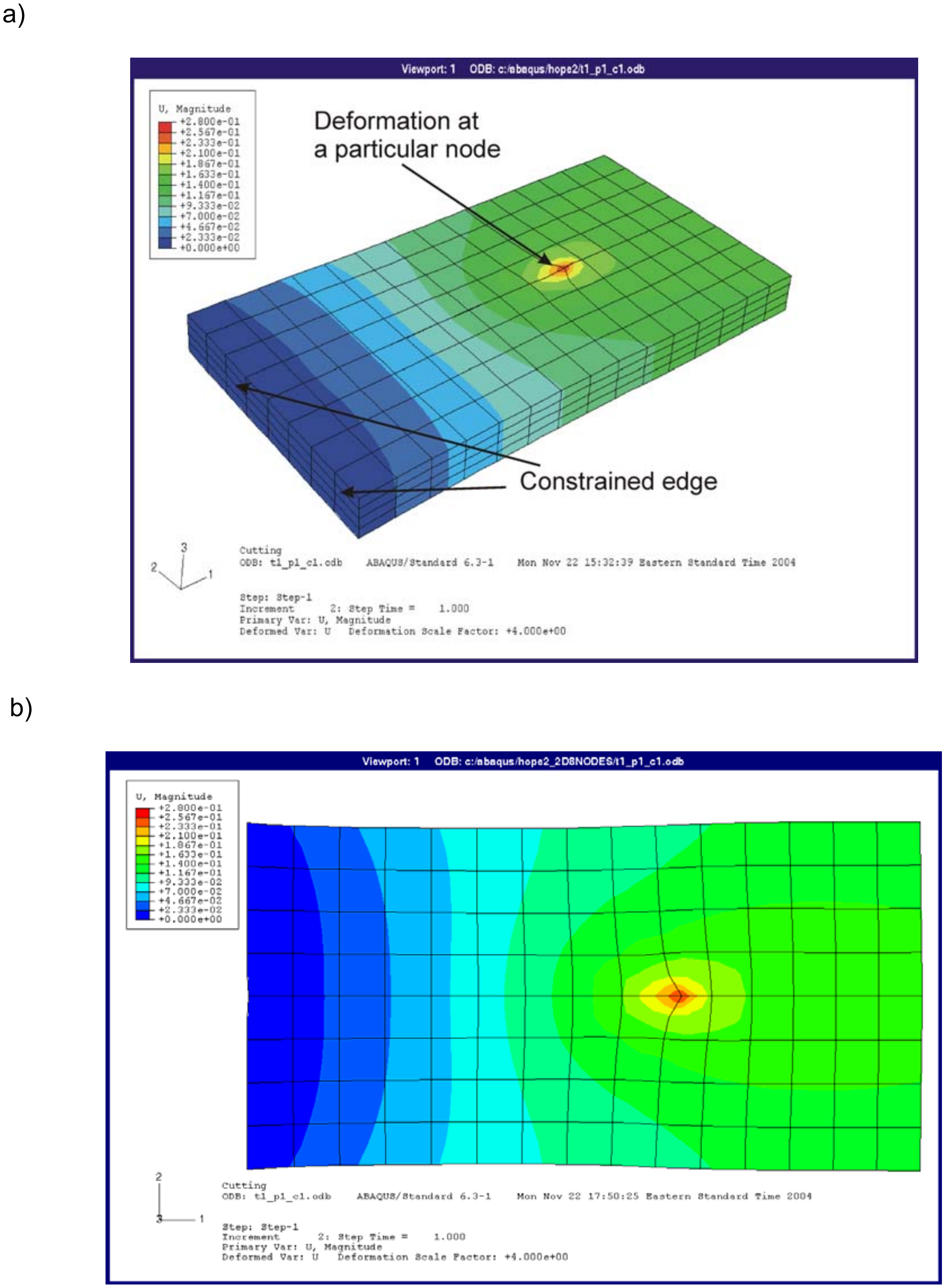

Figure 4.2: Displacement profile from: a) 3D quadratic-element model, b) 2D quadratic-element plane-stress model

4.2 2D quadratic-element models

To reduce the model order further, we reduced the 3D quadratic model to a 2D model with quadratic elements. These are 8-node quadrilateral elements of the Serendipity isoparametric element family. The in-plane displacement can vary quadratically, and the in-plane strains can vary linearly, in the element. We conducted analysis both with a plane-stress elements and plane strain elements. The 2D mesh (Figure 4.2b) consists of 120 elements of 1cm x 1cm size filling the 8cm x15cm x 1cm specimen. The mesh has 8 elements in the width dimension, and 15 elements in the length dimension. There are 438 nodes and 876 degrees of freedom (876 equations).

4.3 2D linear-element models

To further reduce the 2D models above, we conducted plane-stress analysis and plane-strain analysis with 2D linear elements. The mesh looks identical to that in Figure 4.2b. The difference with section 4.2 is the elements do not have mid-side node. Four-node quadrilateral elements of the Serendipity element family are used. The displacements can vary linearly, and the strains and stress are constant, in each element. The model has 120 elements, 160 nodes and 320 degrees of freedom (320 equations).

4.4 Model analysis

We performed a quasi-static analysis using ABAQUS finite element software version 6.3-1. Since the deformation during deformation segment appeared to be linear, we conducted isotropic linear elastic analysis. In this part, we assume two analyses correspond to Poisson's ratio of 0.3 and 0.5.

With experimental force-displacement data from 0.38cm/sec cutting speed, we performed analysis to determine LEM using the 3D-quadratic-element model (20-nodes element) and 2Dquadrtic-element model (8-node elements). Along a cutting path, we determined the LEM corresponded to each deformation segment. The values of the LEM so determined are shown in Figures 4.3, 4.4, and Table 4.1.

Distance from constrained edge (cm)	**LEM from 3D quadratic FE model (N/m^2)**	**LEM from 2D quadratic FE models**		**Ratio of LEM from 2D to that from 3D model**	
		Plane-stress (N/m^2)	**Plane - strain (N/m^2)**	**Plane-stress / 3D model**	**Plane-strain / 3D model**
2.15	3200	3400	3100	0.97	1.1
2.90	7300	7900	7300	1.0	1.09
4.08	9700	10100	9200	0.96	1.04
4.75	36900	37800	35000	0.94	1.02
5.14	29700	30500	28100	0.94	1.02
5.64	37400	38900	35700	0.95	1.04
6.09	18200	18600	17200	0.94	1.0
6.61	60400	61500	56700	0.94	1.02
6.90	50000	50800	46900	0.94	1.02

Table 4.1 Comparison of LEM determined from 3D quadratic-element model and 2D-quadratic-element plane-stress model and plane-strain model.

With the same force-displacement during the deformation, we performed similar analysis using 2D-linear-element (4-node elements) in plane-stress model and plane-strain model. Results are shown in Figures 4.3, 4.4 and Table 4.2. Results from Figures 4.3, 4.4, Tables 4.1 and 4.2 show that the LEM based on 3D model falls in the bracket between the LEM from 2D plane-stress and plane-strain models. The results help verify that the 2D plane-stress and plane-strain model can produce equally good results for LEM as the 3D model.

Distance from constrained edge (cm)	**LEM from 3D**	**LEM from 2D linear FE models**	**Ratio of LEM from 2D to that from 3D model**

	quadratic FE model (N/m^2)	**Plane-stress (N/m^2)**	**Plane - strain (N/m^2)**	**Plane-stress/3D**	**Plane-strain/3D**
2.15	3200	5000	4700	1.57	1.47
2.90	7300	8800	8100	1.21	1.12
4.08	9700	10500	9700	1.09	1.00
4.75	36900	39000	36100	1.06	0.98
5.14	29700	31300	28800	1.05	0.97
5.64	37400	39100	36000	1.04	0.96
6.09	18200	18900	17500	1.04	0.96
6.61	60400	62500	57600	1.04	0.95
6.90	50000	51600	47600	1.03	0.95

Table 4.2 Comparison of LEM determined from 3D quadratic-element model and 2D linear-element plane-stress model and plane-strain model.

From the perspective of computational effort, there is a significant difference among these models – the size (or order) of the model and the computational efforts needed to solve them. Table 4.3 shows a comparison among these models in terms of the total number of elements, total number of nodes and total number of equations. Using the number of equations as a measure of the size (or order) of the model, the relative size of the 3D-quadratic-element model to 2D-quadratic-element model to 2D-linear-element model is 1.0:0.3:0.04. It is expected that compared with the 3D-quadratic-element model, the 2D-quadratic-model will be one order of magnitude less computational-intensive. Further, the 2D-linear-element model is only about 4% as computational intensive as the 3D-quadratic model. Indeed, our computation time for the 2D-linear-model is about 4% of that of the 3D-quadratic-element model.

FE Model	**3D quadratic elements**	**2D quadratic elements**	**2D linear elements**
Number of elements	480	120	120

Number of nodes	2830	438	160
Number of equations	8490	876	320
Relative model size	1.0	0.1	0.04

Table 4.3 Model analysis at different element sizes

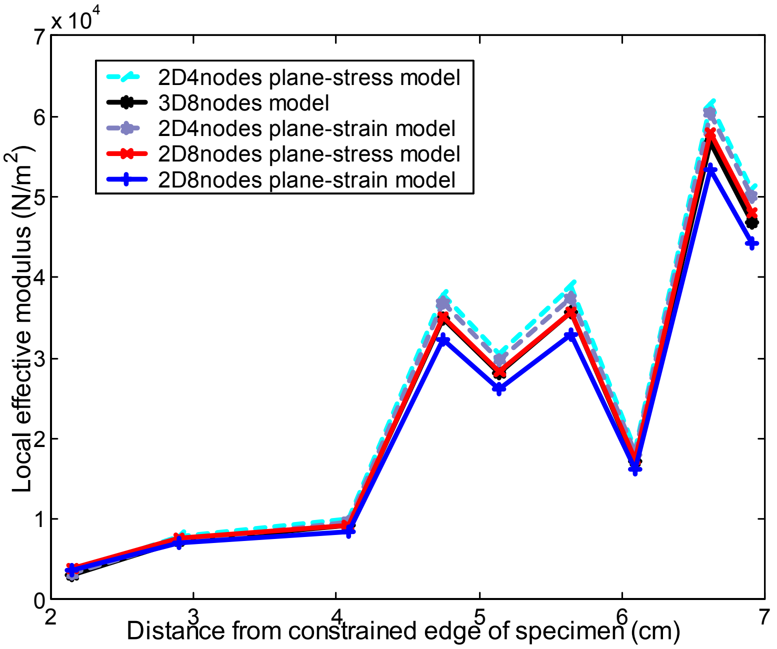

Figure 4.3: Comparison between the values of LEM from 3D-quadratic element model, 2D-quadratic-element models and the 2D-linear-element models

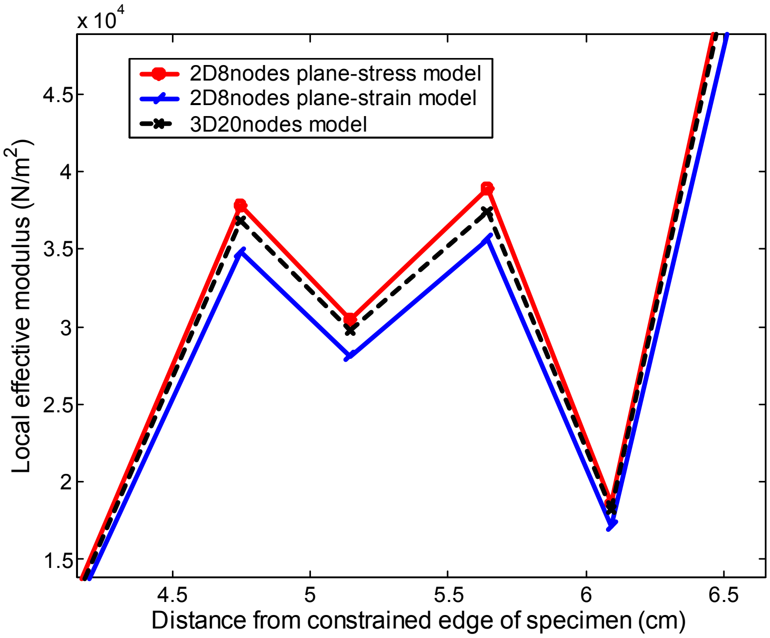

Figure 4.4: Magnified view of a portion of Figure 4.3 showing the LEM from quadratic-element model of 3D analysis is bracketed between LEM determined from 2D plane-stress analysis and plane-strain analysis.

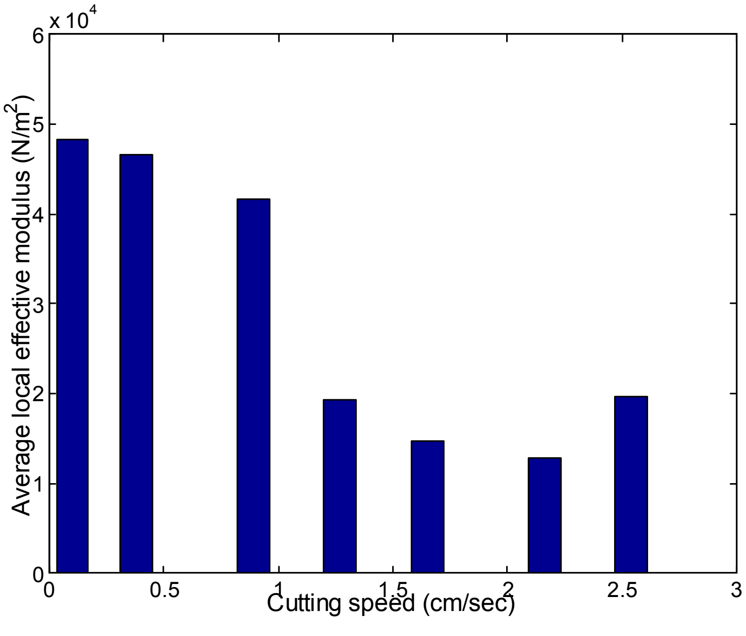

Figure 4.5: Average LEM based on 3D model at various cutting speeds.

Additionally, we used the 3D-quadratic-element model to conduct a parametric study for the effect of cutting speed on the deformation resistance (the LEM) of the liver tissue. Experimental force-displacement data were collected for seven cutting speeds (0.10cm/sec, 0.38cm/sec, 0.89cm/sec, 1.27cm/sec, 1.65cm/sec, 2.16cm/sec, and 2.54 cm/sec). LEM were determined for each of these cutting speeds. The average value of the LEM for each cutting speed was calculated. Figure 4.5 shows the average of the LEM for each of the cutting speeds. It is apparent that the deformation resistant as measured by LEM decreases as the cutting speed increases.

4.4.1 Effect Poisson's ratio

In this part, we studied the effect of the Poisson's ratio on the local effective modulus values. We applied the Poisson's ratio values which are 0.3, 0.4, 0.45, and 0.499 to determine the local effective modulus using 2D-quadratic model. We found that the values of the LEM appeared to be within the same range. The values of Poisson's ratio therefore does not play significant role on the property of the liver tissue.

Distance from constrained edge (cm)	**LEM from 2D quadratic FE models Ratio of LEM from 2D to that from 3D model**			
	P=0.3	**P=0.4**	**P=0.45**	**P=0.499**
	Plane- stress (N/m^2)	**Plane- stress (N/m^2)**	**Plane- stress (N/m^2)**	**Plane- stress (N/m^2)**
2.15	3400	3400	3400	3400
2.90	7900	7980	7960	7900
4.08	10100	10200	10200	10100
4.75	37800	38200	38300	38200
5.14	30500	30800	30900	30900

5.64	38900	39150	39200	39100
6.09	18600	18840	18900	18900
6.61	61500	62200	62300	62400
6.90	50800	51400	51600	51600

Table 4.4 Comparison of LEM determined from 3D quadratic-element model and 2D-quadratic-element plane-stress model at Poisson's ratio of 0.3,0.4,0.45, and 0.499

Since soft tissue is described as nonlinear, incompressible material. We therefore studied the values of LEM at Poisson's ratio ranging between 0.3-0.5. In plane-stress model the LEM values appeared to be approximately the same when the Poisson's ratio was varied between 0.3-0.5. However, in plane-strain model, the value of LEM varies once the Poisson's ratio is varied.

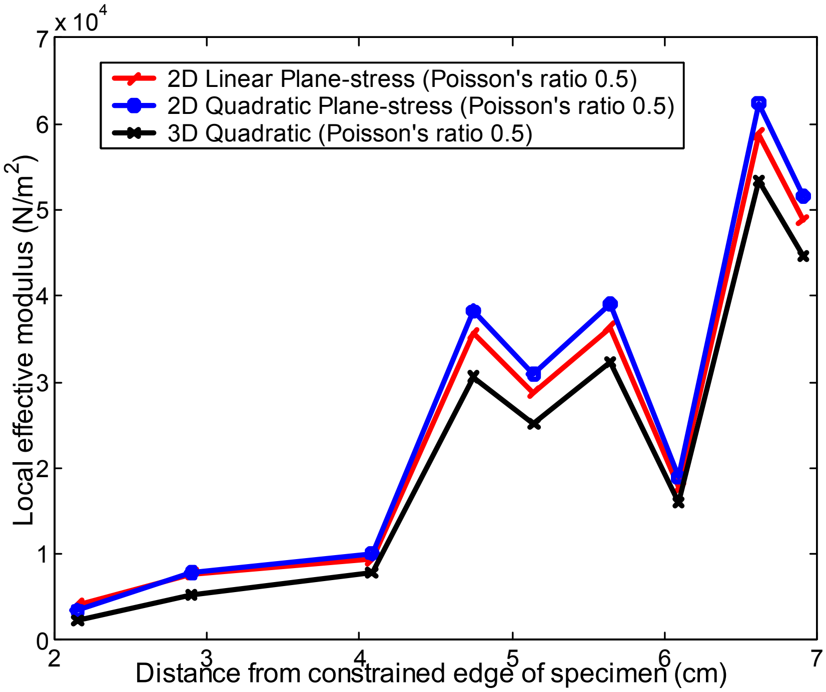

Figure 4.6: Comparison of local effective modulus determined from 2D plane-stress model and 3D model (Poisson's ratio = 0.5)

Results for Poisson's ratio of 0.5

Distance from constrained edge (cm)	LEM from 3D quadratic FE model (N/m^2) reduce Integration	LEM from 2D quadratic FE models and Ratio of LEM from 2D to that from 3D model		LEM from 2D linear FE models and Ratio of LEM from 2D to that from 3D model	
		Plane-stress (N/m^2)	Plane-stress / 3D model	Plane-stress (N/m^2)	Plane-stress / 3D model
2.15	2300	3400	1.48	4100	1.79
2.90	5300	7900	1.50	7700	1.45
4.08	7800	10100	1.30	9400	1.20
4.75	30600	38200	1.25	35600	1.16
5.14	25200	30900	1.22	28800	1.14
5.64	32300	39100	1.21	36300	1.13
6.09	16000	18900	1.19	17700	1.11
6.61	53400	62400	1.17	58800	1.10
6.90	44700	51600	1.15	48800	1.09

Table 4.5 Comparison of LEM determined from 3D quadratic-element model, 2D-quadratic-element plane-stress model, and 2D-linear-element plane-stress model (Poisson's ratio 0.5)

A plane-stress model is a two-dimensional idealization of three-dimensional deformation by imposing the condition that deformation in the thickness direction is completely unconstrained and hence stress components associated with the through-thickness direction are zero. Hence, it is appropriate to use a plane-stress FE model to simulate behavior of thin liver specimens where the through-thickness deformation is unconstrained and hence the through-thickness stress is expected to be negligible. On the other hand, a plane-strain model is a two-dimensional idealization of three-dimensional deformation by imposing the kinematics condition that no deformation in the through-thickness is allowed and hence the through-thickness strain is zero. A plane-strain FE model is appropriate for very, very thick liver specimens which are not free to deform in the through-thickness direction. Since most of our liver samples are not very thick and the tissue can easily deform in the through-thickness direction, a plane stress model would be more appropriate for these cases.

4.4.2 Effect of element size on LEM values

The size of the element in FE model effects the values of the LEM. Since our goal is to minimize the computation time during finite element simulation, having coarse mesh helps simplify the equations and results in less computation time. We study the relationship between the element size and the LEM values. The analysis was done based on 6 cutting experiment at 90degrees cutting angle and cutting speed of 0.1cm/sec. The Poisson's ratio is 0.3 and the element used in this analysis is linear quadratic element (ABAQUS CPS8).

Experiment 1

	Number of nodes	Number of elements	Average LEM $x10^4$ N/m^2
1	440	120	3.03
2	838	200	3.10
3	1594	480	3.49
4	6066	1920	3.87
5	9382	3000	4.02

Table 4.6 Average LEM at various element size for experiment 1

Experiment 2

	Number of nodes	Number of elements	Average LEM $x10^4$ N/m^2

1	440	120	5.26
2	838	200	5.36
3	1594	480	6.02
4	6066	1920	6.62
5	9382	3000	6.82

Table 4.7 Average LEM at various element size for experiment 2

Experiment 3

	Number of nodes	Number of elements	Average LEM $\times 10^4$ N/m^2
1	440	120	4.90
2	838	200	5.04
3	1594	480	5.57
4	6066	1920	6.15
5	9382	3000	6.35

Table 4.8 Average LEM at various element size for experiment 3

Experiment 4

	Number of nodes	Number of elements	Average LEM $\times 10^4$ N/m^2
1	440	120	5.21
2	838	200	5.26
3	1594	480	5.91
4	6066	1920	6.51
5	9382	3000	6.72

Table 4.9 Average LEM at various element size for experiment 4

Experiment 5

	Number of nodes	Number of elements	Average LEM $\times 10^4$ N/m^2
1	440	120	6.33
2	838	200	6.50
3	1594	480	7.20
4	6066	1920	7.93
5	9382	3000	8.17

Table 4.10 Average LEM at various element size for experiment 5

Experiment 6

	Number of nodes	Number of elements	Average LEM $\times 10^4$ N/m^2
1	440	120	5.80
2	838	200	5.89
3	1594	480	6.62
4	6066	1920	7.28
5	9382	3000	7.51

Table 4.11 Average LEM at various element size for experiment 6

The result from 6 cutting experiments at different mesh size shows the value of the LEM increased as the element size got smaller and smaller.

Details about element size:

	Number of nodes	Number of elements	Area of each element (unit)	Number of element per unit area

1	440	120	1	1
2	838	200	0.5	2
3	1594	480	0.25	4
4	6066	1920	0.0625	16
5	9382	3000	0.04	25

Table 4.12 Element size per unit area

Refining the finite element mesh allowed us to be able to scale the LEM values once the size of the mesh is changed. In reality, very small element size would reflect the closest approximation to the real property of material. However, our goal is to use to most simplified finite element model (coarse mesh) to achieve real time simulation at the same time provide the end user with the realistic force feedback. As from our analysis, the LEM values are consistent with the element size. Therefore, the element size versus LEM values analysis in this part can be used as a scaling factor once the element size varied.

4.5 Discussion

For real-time medical simulation requiring accurate haptic feedback, it is important to have reality-based models that are fast (computationally non-intensive) but still preserve the actual overall force-displacement behavior. Several 3D and 2D finite element models with three levels of model order reduction were studied. These model order reductions simplify the internal complexities of the model while preserving the overall input-output (displacement-force) behavior. All these models can determine the local effective modulus equally well, and the results of the 3D model are bracketed by results from the 2D plane-stress model and 2D plane-strain model.

A plane-stress FE model is most appropriate for simulating the cutting of very thin liver specimens in which the through-thickness stress is negligible (i.e. completely unconstrained in the thickness dimension and allows free through-thickness deformation). A plane-strain FE model is most appropriate for very thick liver specimens in which the through-thickness strain is negligible (i.e. fully constrained in the thickness dimension and does not allowed to through-thickness deformation). It is reasonable that the results of the 3D model falls in-between the results from the two limiting case of plane-stress and plane-strain models. With regard to computation effort required, there is a significant difference among these models. The computation effort required for the 2D-quadratic-element model is one order of magnitude less that required for the 3D-quadratic-element model. The computation effort for the 2D-linear-element model is two orders of magnitude smaller than that of the 3D-quadratic-element model.

Chapter 5: Parametric study: Effect of cutting speed and cutting angle on the LEM

Characterizing and modeling of soft tissue deformation during cutting is important for developing a reality based haptic interaction model for surgical training and simulation. In this chapter, experiments were performed for soft tissue cutting (ex-vivo) monitoring the cutting forces and blade displacement for various cutting speeds (ranging from 0.1cm/sec-2.54cm/sec) and cutting angles (for 0^o and 45^o cutting angle). The measured force-displacement curves in all cases exhibit a characteristic pattern: repeating units formed by a segment of linear loading (deformation of tissue) immediately followed by a segment of sudden unloading (localized crack extension in the tissue). This chapter addresses the characterization of the deformation resistance during the deformation segment. The variation of this deformation resistance with cutting parameters is also determined. The deformation resistance to the cutting blade was characterized via a quantity designed as the local effective modulus (LEM) of the tissue.

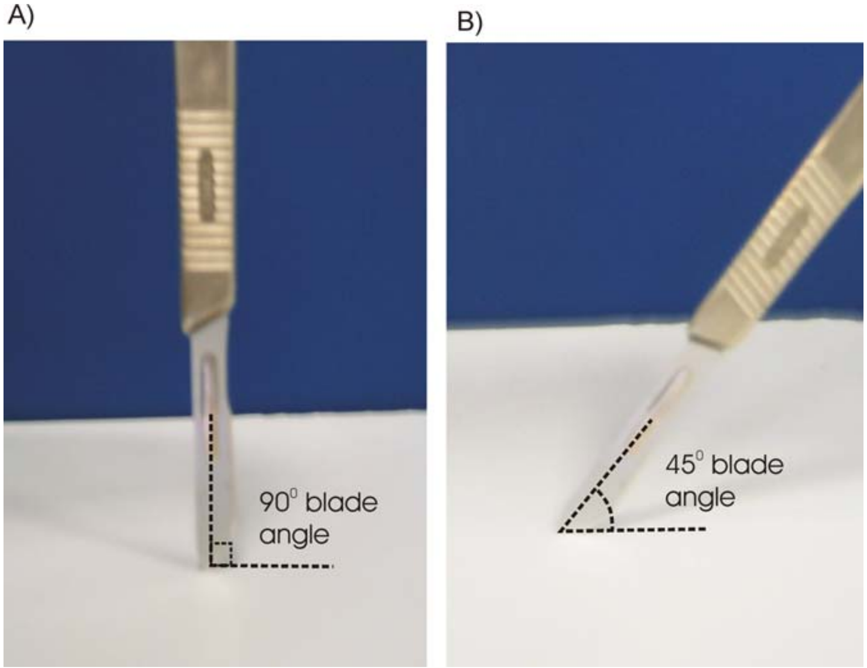

Figure 5.1: a) Cutting angle at 90^o (vertical) and b) Cutting angle at 45^o (conventional cut).

We studied the effect of cutting speed and cutting angles on the LEM. We conducted six liver cutting experiments at 90° cutting angle (see Figure 5.1) for each of seven cutting speeds (0.1cm/sec, 0.38cm/sec, 0.89cm/sec, 1.27cm/sec, 1.65cm/sec, 2.16cm/sec, and 2.54cm/sec.) Again, the force-displacement data revealed that the cutting process consisted of a sequence of repeating units each comprising of a linear loading deformation phase followed by a localized crack extension phase (load drop) in the tissue. We seek to characterize the deformation resistance of the loading deformation segment.

We first present results from our experiments for liver cutting with 45° cutting angle at quasi-static cutting speed (0.1cm/sec), intermediate cutting speed (1.27cm/sec), and normal cutting speed (2.54cm/sec). This is followed by presenting the analyzed data for multiple cutting speeds at 90° cutting angle (blade was vertical) and 45° cutting angle (preferred angle in surgery). Figure 5.1 shows the blade orientation of 90° and 45° used in the experiments.

5.1 Cutting at 45° blade angle

In this part, we performed 6 cuttings at 45° cutting angle (see figure 5.1b) at quasi-static cutting speed (0.1cm/sec), intermediate cutting speed (1.27cm/sec), and normal cutting speed (2.54cm/sec). Figure 5.2 shows the plot of LEM versus the distance from constrained edge of specimen for a typical liver cutting experiment. Results from cutting at 0.1cm/sec, 1.27cm/sec, and 2.54cm/sec are shown in Figure 5.3 and Table 5.1. Using the approach described in section 2.3, quasi-static cutting resulted in the average LEM in the neighborhood of 63,000 N/m^2 with standard deviation of 13,000 N/m^2 in the plane stress model and 59,000 N/m^2 with standard deviation of 14,000 N/m^2 in the plane strain model. At cutting speed of 1.27cm/sec, the average LEM value was 19,000 N/m^2 with standard deviation of 4,000 N/m^2 in the plane stress model and 18,000 N/m^2 with standard deviation of 4,000 N/m^2 in the plane strain model. Finally, at normal cutting speed of 2.54cm/sec, the average LEM value was 18,000 N/m^2 with standard deviation of 4,000 N/m^2 in plane stress model and 16,000 N/m^2 with standard deviation of 4,000

N/m^2 in plane strain model. It is apparent that the deformation resistance of the tissue decreases with increasing cutting speed.

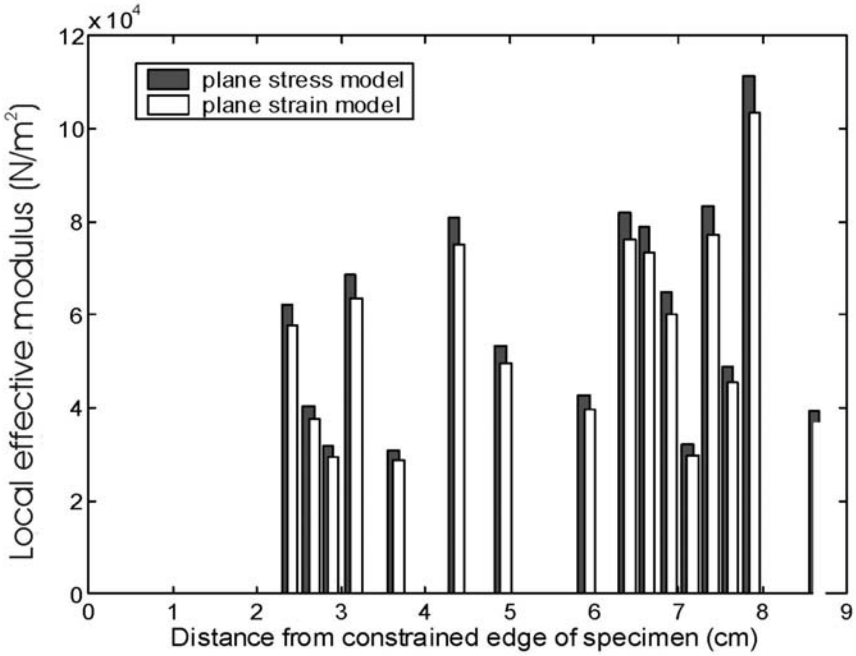

Figure 5.2: Local effective modulus for the loading segments for a typical cut at 45^0 blade angle (plane stress and plane strain analysis)

	Plane stress model V=0.1cm/sec		Plane strain model V=0.1cm/sec		Plane stress model V=1.27cm/sec		Plane strain model V=1.27cm/sec		Plane stress model V=2.54cm/sec		Plane strain model V=2.54cm/sec	
Test #	Average LEM $x10^3$ N/m^2	Standard deviation $x10^3$ N/m^2	Average LEM $x10^3$ N/m^2	Standard deviation $x10^3$ N/m^2	Average LEM $x10^3$ N/m^2	Standard deviation $x10^3$ N/m^2	Average LEM $x10^3$ N/m^2	Standard deviation $x10^3$ N/m^2	Average LEM $x10^3$ N/m^2	Standard deviation $x10^3$ N/m^2	Average LEM $x10^3$ N/m^2	Standard deviation $x10^3$ N/m^2
1	66	13	61	12	21	8	20	6	20	8	19	7
2	86	10	80	9	19	7	18	7	17	5	16	5
3	39	13	36	12	18	9	17	8	20	6	19	5
4	64	21	60	19	26	12	24	11	10	5	9	5
5	65	17	60	16	14	7	13	7	21	6	19	5
6	61	21	56	20	15	4	14	4	19	8	13	6
Avg	63.50	13.67	58.83	13.81	18.83	3.98	17.67	3.68	17.83	3.72	15.83	3.76

Table 5.1 Average LEM for each cut on the liver and the corresponding standard deviation for 3 cutting speeds at 45° blade angle.

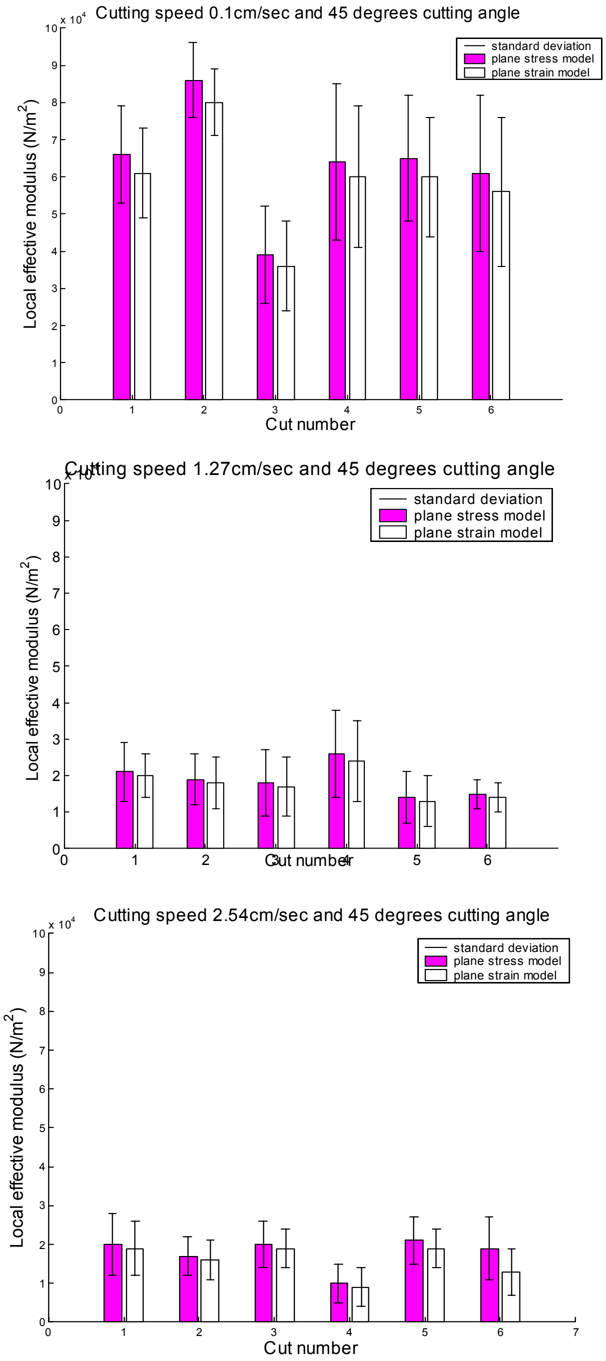

Figure 5.3: The average of the local effective modulus of six cuts and the corresponding standard deviation at 0.1cm/sec, 1.27cm/sec, and 2.54cm/sec cutting speed at 45° blade angle.

5.2 Cutting at 90° blade angle

At 90^{o} blade angle, we performed 12 liver cuttings at 0.1cm/sec, 1.27cm/sec, and 2.54cm/sec. The results are summarized in Figures 5.4. The associated numerical data is listed in Tables 5.2, 5.3, and 5.4. These results reveal that the local effective modulus varied from location to location in the liver, but the spatial variation was within reasonable bounds at each cutting speed.

	Plane stress model		**Plane strain model**	
Test #	**Average LEM X10^3 N/m^2**	**Standard deviation X10^3 N/m^2**	**Average LEM X10^3 N/m^2**	**Standard deviation X10^3 N/m^2**
1	59	24	55	23
2	48	15	44	14
3	64	24	60	23
4	72	23	67	21
5	62	23	57	22
6	52	16	49	15
7	100	34	94	33
8	57	21	53	19
9	65	23	60	21
10	56	20	52	19
11	40	19	37	16
12	37	21	34	19
Average	**59**	**16**	**55**	**15**

Table 5.2 Table of the average local effective modulus for each cut on the liver and the corresponding standard deviation for cutting speed of 0.1cm/sec.

	Plane stress model		**Plane strain model**	
Test #	**Average LEM X10^3 N/m^2**	**Standard deviation X10^3 N/m^2**	**Average LEM X10^3 N/m^2**	**Standard deviation X10^3 N/m^2**
1	57	29	53	27

2	59	25	55	23
3	46	22	43	21
4	68	32	63	30
5	58	30	54	28
6	55	23	51	22
7	72	40	67	37
8	52	27	48	25
9	52	28	48	26
10	49	20	46	19
11	31	12	29	11
12	26	13	25	12
Average	**52**	**13**	**49**	**12**

Table 5.3 Table of the average local effective modulus for each cut on the liver and the corresponding standard deviation for cutting speed of 1.27cm/sec

	Plane stress model		**Plane strain model**	
Test #	**Average LEM $X10^3$ N/m^2**	**Standard deviation $X10^3$ N/m^2**	**Average LEM $X10^3$ N/m^2**	**Standard deviation $X10^3$ N/m^2**
1	37	19	35	17
2	34	15	32	14
3	45	21	43	18
4	24	11	23	10
5	37	15	35	14
6	49	29	45	27
7	53	31	50	29
8	42	18	39	17
9	38	17	35	16
10	37	21	34	19
11	42	19	39	17
12	49	21	46	20

Average	**41**	**7.5**	**38**	**7**

Table 5.4 Table of the average local effective modulus for each cut on the liver and the corresponding standard deviation for cutting speed of 2.54cm/sec

To compare the local effective modulus estimated at 1.27cm/sec cutting speed, for example, we always performed two additional cuts on the same liver sample at 0.1cm/sec and 2.54cm/sec cutting speed. A similar protocol was followed at 2.54cm/sec cutting speed. Estimating the values of the local effective modulus from these two additional cuts to those determined by 12 cuts for a given cutting speed, provided us with a basis for comparing the LEM across different liver samples at different cutting speeds. We concluded that the LEM estimated from the additional cuts was within reasonable bounds compared to the data obtained from the 12 cuts for a given cutting speed of the blade. This procedure ensured that the comparison of the LEM at various cutting speeds from each sample and across samples was valid.

For cutting speed of 0.1cm/sec, the average LEM was in the neighborhood of 59,000 N/m^2 for use with plane-stress model, and 55,000 N/m^2 for use with plane-strain model. Table 5.2 shows that for a given liver specimen, the standard deviation of the average LEM ranged between 14,000 N/m^2 and up to 34,000 N/m^2 in some cuts. This is expected since the liver tissue is highly non-homogeneous and the initial model was two-dimensional.

For cutting speed of 1.27cm/sec, the average LEM was in the neighborhood of 52,000 N/m^2 in plane stress analysis with standard deviation of 13,000 N/m^2 and 49,000 N/m^2 in plane strain analysis with standard deviation of 12,000 N/m^2. For cutting speed of 2.54cm/sec, the results revealed that the average LEM was in the neighborhood of 41,000 N/m^2 in plane stress analysis

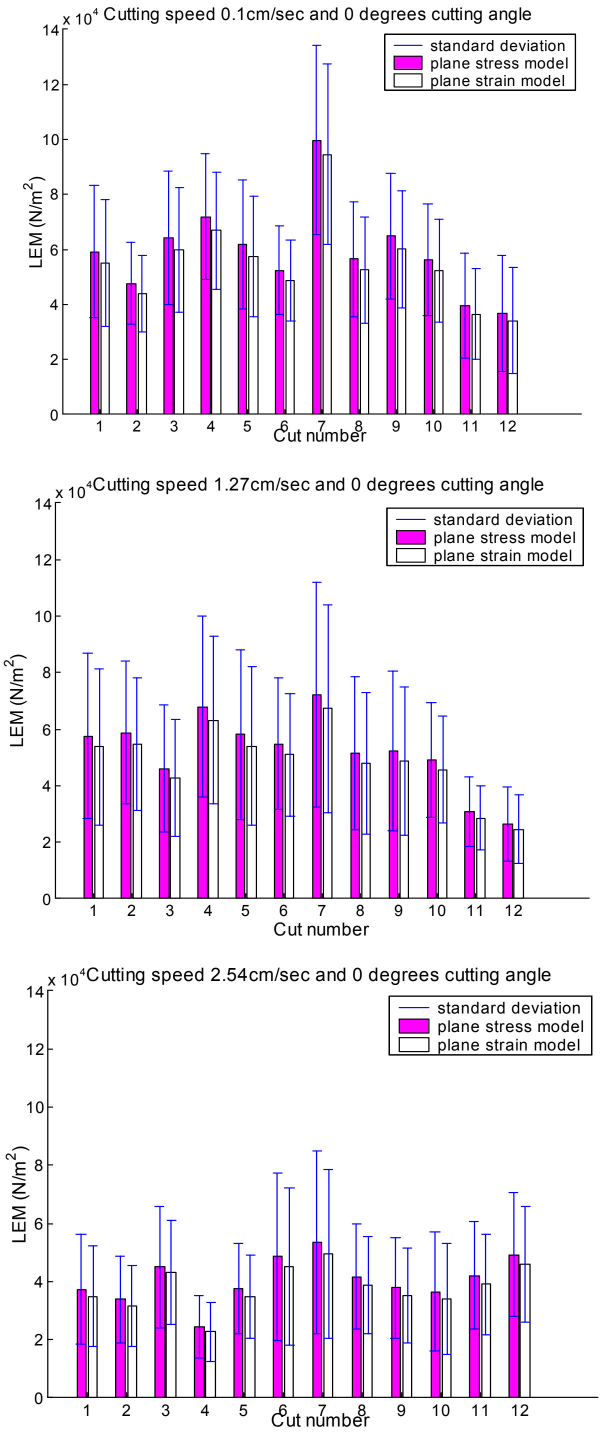

Figure 5.4: The average of the local effective modulus of twelve cuts and the corresponding standard deviation at 0.1cm/sec, 1.27cm/sec, and 2.54cm/sec cutting speed at 90° blade angle.

with standard deviation of 7,500 N/m^2 and 38,000 N/m^2 in plane strain analysis with standard deviation of 7,000 N/m^2. We also observed that as the cutting speed increased, the values of the LEM and the corresponding standard deviation decreased.

5.3 Cutting at 90^o versus 45^o without normalizing the cutting force

Without normalizing the cutting, we performed experiments at 7 preset cutting speeds of 0.1, 0.38, 0.89, 1.27, 1.65, 2.16, and 2.54cm/second with a blade angle of 90^o. Each liver sample (size of 8x12x2.5 cm) could accommodate four parallel cutting lines. During the cutting process, we obtained the force versus distance from the constrained boundary characteristics of liver tissue. We used the JR3 force sensor to measure the X, Y, and Z components of the cutting force and the norm of these forces was plotted versus the displacement of the cutting blade. We conducted 12 liver cutting experiments for 90^o cutting angle. Similar to cutting at 90^o blade angle, we performed 6 liver cutting experiments at 45^o cutting angle at various cutting speeds, namely, 0.1, 0.38, 0.89, 1.27, 1.65, and 2.54cm/sec. As shown in Figure 5.5, Figure 5.6, and Table 5.5, the LEM of the pig liver decreased with increasing cutting speed.

The relationship between LEM and cutting speed at 90^o angle was observed to be linear in both plane stress (Figure 5.5) and plane strain models (Figure 5.6). The observed linear relationship between the LEM ($E^{effective}$ x10^3 N/m^2) and cutting speed (v cm/sec) for 0^o cutting angle was observed to be:

$$E^{effective} = -9.21v + 63.26 \qquad 0.1 cm/sec \le v \le 2.54 cm/sec \qquad (5.1)$$

$$E^{effective} = -8.70v + 59.18 \qquad 0.1 cm/sec \le v \le 2.54 cm/sec \qquad (5.2)$$

This implied that during slow cutting, there was more deformation resistance encountered by the blade than at higher cutting speeds. The linear model could thus be used to predict the characteristic of the liver tissue for 90^o cutting angle at different cutting speeds. Results also show that the range of LEM values for both plane stress and plane strain analysis for 90 degrees cutting angle and variable cutting speeds were within close bounds.

	Plane stress model (90^o angle)		**Plane strain model (90^o angle)**		**Plane stress model (45^o angle)**		**Plane strain model (45^o angle)**	
Cutting speed cm/sec	Average LEM $x10^3$ N/m^2	Standard deviation $x10^3$ N/m^2	Average LEM $x10^3$ N/m^2	Standard deviation $x10^3$ N/m^2	Average LEM $x10^3$ N/m^2	Standard deviation $x10^3$ N/m^2	Average LEM $x10^3$ N/m^2	Standard deviation $x10^3$ N/m^2
0.1	59	16	55	15	64	14	59	14
0.38	61	13	57	12	40	11	37	10
0.89	58	13	54	12	24	13	22	8
1.27	52	13	49	12	19	4	18	4
1.65	50	9	47	9	20	2	18	5
2.16	39	10	36	9	-	-	-	-
2.54	41	8	38	7	18	4	16	4

Table 5.5 Average LEM values for various cutting speeds and cutting angles at Poisson's ratio of 0.3 based on non-normalized force

From results for 45^o cutting angle (see Table 5.5), it is apparent that the LEM decreases with increasing cutting speed. However, unlike the 90^o cutting angle results, the variation of LEM with cutting speed is nonlinear at 45^o cutting angle. The nonlinear relationship describing the variation of LEM ($E^{effective}$ $x10^3$ N/m^2) versus the cutting speed (v cm/sec) for 45^o cutting angle can be expressed as:

$$E^{effective} = 24.21(v^{-0.42}) \qquad 0.1cm/sec \le v \le 2.54cm/sec \qquad (5.3)$$

$$E^{effective} = 22.17(v^{-0.43}) \qquad 0.1cm/sec \le v \le 2.54cm/sec \qquad (5.4)$$

Equations (5.1) and (5.3) correspond to plane stress model for 90^o and 45^o cutting angle respectively, while equations (5.2) and (5.4) correspond to plane strain model for 90^o and 45^o cutting angle respectively. These models can be used for determining the LEM at other cutting speeds for either 90^o or 45^o cutting angle in surgical tissue cutting simulation.

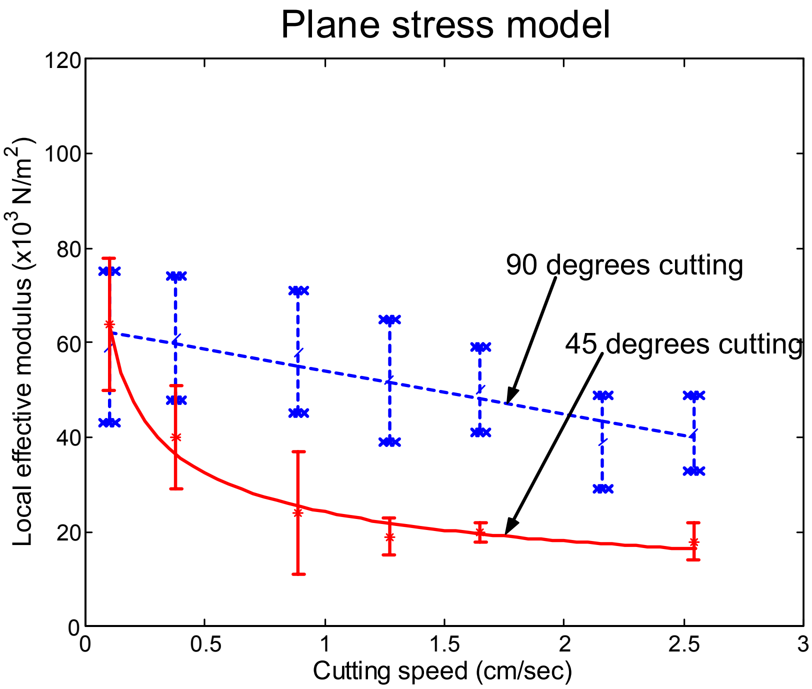

Figure 5.5: Plot of local effective modulus versus cutting speed for 90° and 45° cutting angle with plane stress model.

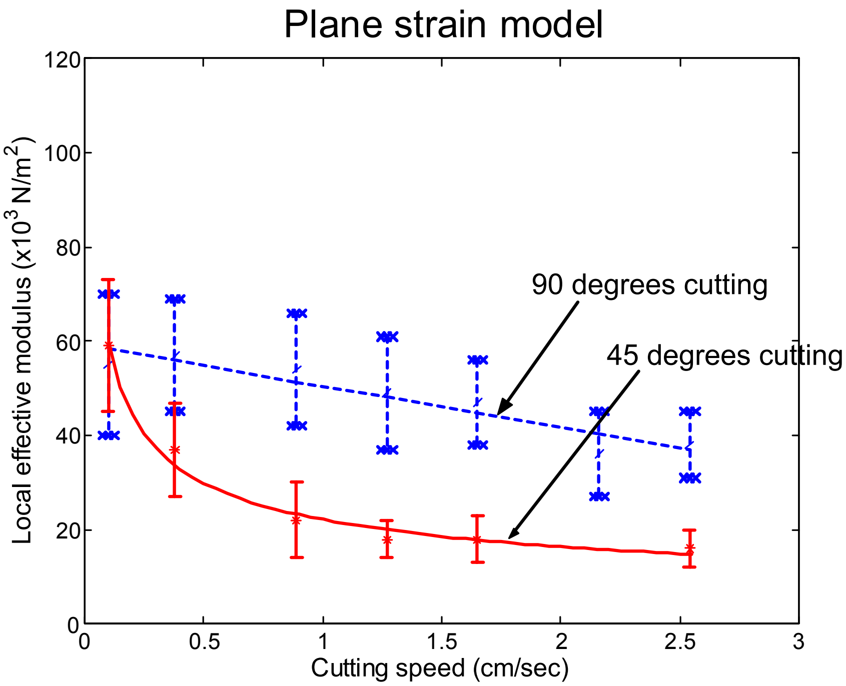

Figure 5.6: Plot of local effective modulus versus cutting speed for 90° and 45° cutting angle with plane strain model.

5.4 Cutting at 90^o versus 45^o based on normalized cutting force

In our experiments, the depth of cut (blade length embedded in the tissue) varied as the scalpel travels to different locations in the liver of non-uniform thickness. For a typical liver specimen, the depth of cut ranged from 0cm to about 2cm. To incorporate the depth of cut in the analysis, results presented in this section were based on depth-of-cut normalized cutting force increment. The deformation resistance of the soft tissue characterized was denoted as the normalized local effective modulus (LEM) of the soft tissue. The relationship between LEM and cutting speed at 90^o angle was observed to be linear in both plane stress (Figure 5.7) and plane strain models (Figure 5.8). The observed linear relationship between the LEM ($E^{effective}$ $x10^3$ N/m^2) and cutting speed (v cm/sec) for 90^o cutting angle was observed to be:

$$\text{Plane-Stress:} \qquad E^{effective} = -11.6v + 48.4 \qquad 0.1cm/sec \le v \le 2.54cm/sec \qquad (5.5)$$

$$\text{Plane-Strain:} \qquad E^{effective} = -7.2v + 30.9 \qquad 0.1cm/sec \le v \le 2.54cm/sec \qquad (5.6)$$

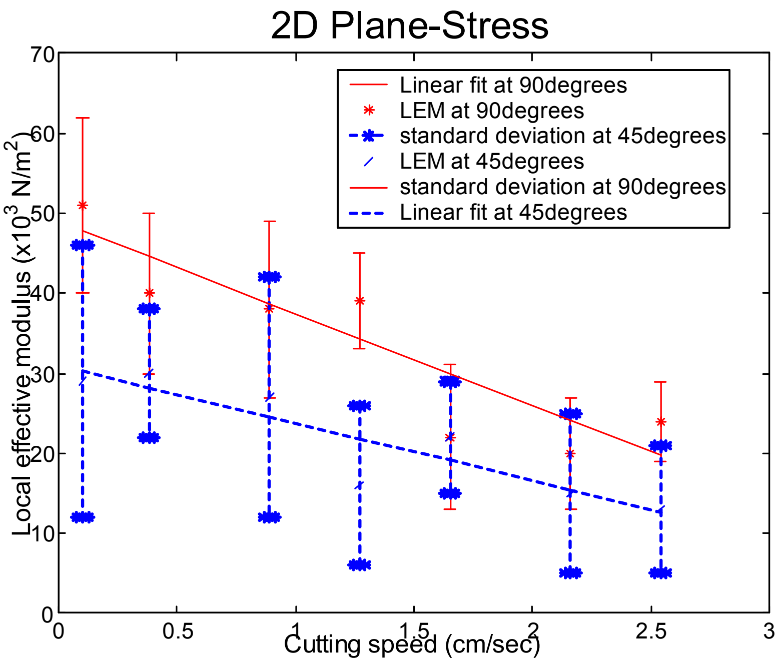

Figure 5.7: Plot of local effective modulus versus cutting speed for 90^o and 45^o cutting angle with plane stress model.

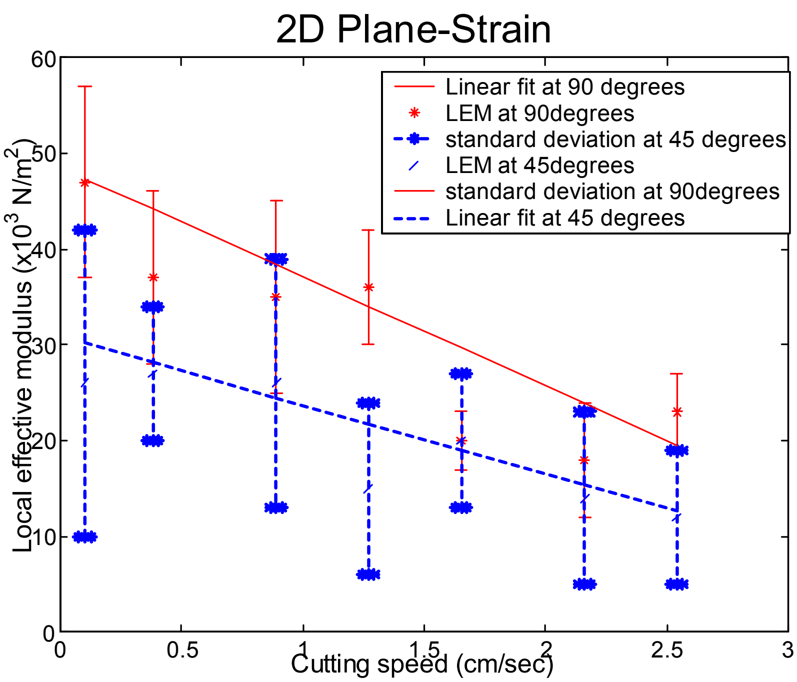

Figure 5.8: Plot of local effective modulus versus cutting speed for 90° and 45° cutting angle with plane strain model.

The results implied that during slow cutting, there was more deformation resistance encountered by the blade than at higher cutting speeds. The linear model could thus be used to predict the characteristic of the liver tissue for 90° cutting angle at different cutting speeds. Results also show that the range of LEM values for both plane stress and plane strain analysis for 90° cutting angle and variable cutting speeds were within close bounds. From results for 45° cutting angle (see Table 5.6), it was apparent that the LEM decreases with increasing cutting speed. Similar to the 90° cutting angle results, the variation of LEM with cutting speed was linear at 45° cutting angle. The linear relationship describing the variation of LEM ($E^{effective}$ x10^3 N/m^2) versus the cutting speed (v cm/sec) for 45° cutting angle can be expressed as:

$$\text{Plane-Stress:} \quad E^{effective} = -10.6v + 44.5 \quad 0.1cm/sec \le v \le 2.54cm/sec \quad (5.7)$$

$$\text{Plane-Strain:} \quad E^{effective} = -6.4v + 28.2 \quad 0.1cm/sec \le v \le 2.54cm/sec \quad (5.8)$$

Equations (5.5) and (5.7) correspond to plane stress model for 90° and 45° cutting angle respectively, while equations (5.6) and (5.8) correspond to plane strain model for 90° and 45° cutting angle respectively. These models can be used for determining the LEM at other cutting speeds for either 90° or 45° cutting angle in surgical tissue cutting simulation.

	Plane stress model (90° angle)		**Plane strain model (90° angle)**		**Plane stress model (45° angle)**		**Plane strain model (45° angle)**	
Cutting speed cm/sec	Average LEM $x10^3$ N/m^2	Standard deviation $x10^3$ N/m^2	Average LEM $x10^3$ N/m^2	Standard deviation $x10^3$ N/m^2	Average LEM $x10^3$ N/m^2	Standard deviation $x10^3$ N/m^2	Average LEM $x10^3$ N/m^2	Standard deviation $x10^3$ N/m^2
0.1	51	11	47	10	29	17	26	16
0.38	40	10	37	9	30	8	27	7
0.89	38	11	35	10	27	15	26	13
1.27	39	6	36	6	16	10	15	9
1.65	22	9	20	3	22	7	20	7
2.16	20	7	18	6	15	10	14	9
2.54	24	5	23	4	13	8	12	7

Table 5.6 Average LEM values for various cutting speeds and cutting angles at Poisson's ratio of 0.3 based on normalized force

5.5 Cutting at 90° versus 45° with normalized cutting force at Poisson's ratio 0.5

Since the liver tissue is considered incompressible, we repeated the similar analysis based on previous force/displacement data from cutting experiment at Poisson's ratio of 0.5. The Poisson's ratio of the pig's liver found [31] based on elongation experiment was 0.43±0.16 and compression experiment was 0.47±0.15.

Results show that, as the cutting speed increased, the tissue offered less apparent resistance to deformation. As a result the magnitude of LEM decreased. Figure 5.9 shows the values of LEM at seven cutting speeds. The average LEM is shown in Table 5.7. At 0.1cm/sec cutting speed, the average LEM was 82×10^3 N/m^2 with standard deviation of 17×10^3 as determined from plane-stress model. At cutting speed of 1.27cm/sec, the average LEM was 69×10^3 N/m^2 with standard deviation of 12×10^3as determined from plane-stress model. Finally, at cutting speed of 2.54cm/sec (1inch/sec), the average LEM value was 38×10^3 N/m^2 with standard deviation of 9×10^3 as determined from plane-stress model. In order to study the effect of cutting angle on the LEM, we performed additional experiments at 45 degrees cutting angle (see Figure 5.9). We conducted experiments at 7 preset cutting speeds of 0.1, 0.38, 0.89, 1.27, 1.65, 2.16, and 2.54cm/second with a blade angle of 45^o. As shown in Figure 5.9 and Table 5.7, the LEM of the pig liver decreased with increasing cutting speed.

The relationship between LEM and cutting speed at 90^o angle was observed to be linear (Figure 5.9). The observed linear relationship between the LEM ($E^{effective}$ $\times 10^3$ N/m^2) and cutting speed (v cm/sec) for 90^o cutting angle was observed to be:

$$\text{Plane-Stress:} \qquad E^{effective} = -18.22v + 79.12 \qquad 0.1 cm/sec \le v \le 2.54 cm/sec \qquad (5.9)$$

This implied that during slow cutting, there was more deformation resistance encountered by the blade than at higher cutting speeds. The linear model could thus be used to predict the characteristic of the liver tissue for 90^o cutting angle at different cutting speeds. Results also show that the range of LEM values for both plane stress and plane strain analysis for 90^o cutting angle and variable cutting speeds were within close bounds. From results for 45^o cutting angle (see Table 5.7), it was apparent that the LEM decreases with increasing cutting speed. Similar to the 90^o cutting angle results, the variation of LEM with cutting speed was linear at 45^o cutting angle. The linear relationship describing the variation of LEM ($E^{effective}$ $\times 10^3$ N/m^2) versus the cutting speed (v cm/sec) for 45^o cutting angle can be expressed as:

$$\text{Plane-Stress:} \qquad E^{effective} = -11.59v + 49.59 \qquad 0.1 cm/sec \le v \le 2.54 cm/sec \qquad (5.10)$$

These models can be used for determining the LEM at other cutting speeds for either 90^o or 45^o cutting angle in surgical tissue cutting simulation.

	Plane stress model (90^{o} angle)		**Plane strain model (90^{o} angle)**		**Plane stress model (45^{o} angle)**		**Plane strain model (45^{o} angle)**	
Cutting speed cm/sec	Average LEM $x10^3$ N/m^2	Standard deviation $x10^3$ N/m^2	Average LEM $x10^3$ N/m^2	Standard deviation $x10^3$ N/m^2	Average LEM $x10^3$ N/m^2	Standard deviation $x10^3$ N/m^2	Average LEM $x10^3$ N/m^2	Standard deviation $x10^3$ N/m^2
0.1	82	17	64	13	49	27	39	21
0.38	67	18	52	13	46	9	36	7
0.89	59	19	46	15	42	22	34	18
1.27	69	12	54	10	26	16	20	12
1.65	39	9	31	7	34	12	27	9
2.16	36	8	29	5	26	16	21	15
2.54	38	9	30	3	20	18	16	10

Table 5.7 Average LEM values for various cutting speeds and cutting angles at Poisson's ratio of 0.499

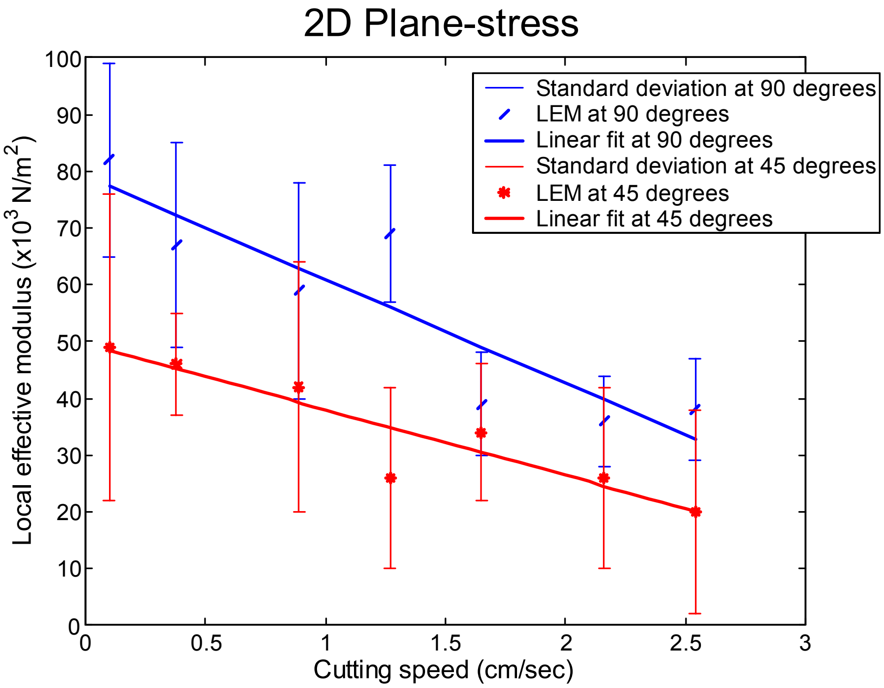

Figure 5.9: Variation of local effective modulus with cutting speed for 90^{o} and 45^{o} cutting angle (2D plane-stress model, Poisson's ratio = 0.5).

5.6 Discussion

Results from experiments reveal that the cutting force-displacement curves exhibit a characteristic pattern: repeating units formed by a segment of linear loading (deformation of tissue) immediately followed by a segment of sudden unloading (localized crack extension in the tissue). This chapter addresses the characterization of the deformation resistance during the deformation segment. A sequel chapter will characterize the fracture resistance during the localized crack extension segment. A self-consistent local effective modulus (LEM) has been used as a vehicle to characterize the deformation resistance during the monotonic deformation segment of each repeating unit of the cutting force-displacement curve. This phenomenological measure of the resistance to deformation can reflect the overall effects of different physical mechanisms of tissue deformation encountered by the cutting blade under varies cutting conditions. Results show that as measured in the form of LEM, the resistance to deformation of the tissue varies with cutting speed and the angle of cut. The deformation resistance decreases as cutting speed increases. For a fixed cutting speed, the resistance to deformation is lower at 45^o cutting angle than at 0^o cutting angle. This is consistent with visual observation that there was physically more tissue deformation encountered by the blade when the blade was perpendicular to the tissue surface (90^o cutting angle). The deformation resistance varies linearly with cutting speed for 90^o cutting angle, while it varies non-linearly for 45^o cutting angle. The values for LEM obtained with plane-stress finite element model and plane-strain finite element model were very close to each other, thereby justifying the use two-dimensional model to simulate cutting liver of various thickness. The deformation resistance as characterized via LEM can be used in future finite element models to simulate the deformation segment occurring prior to the onset each localized cut (crack) growth. On the other hand, to characterize the fracture resistance of the localized crack growth segment, a fracture mechanics formulation needs to be developed**.** Application of linear elastic fracture mechanics (LEFM) with small-scale yielding assumption will be a start but probably will not be sufficient. The energy release rate of traditional LEFM may not be a valid fracture characterizing parameter for nonlinear deforming soft tissue in surgery condition. For our circumstances, the fracture mechanics formulation also needs to accommodate tissue samples that are not preconditioned and maybe flexibly supported at its boundaries. This is because in surgery the cutting forces experienced by the surgeon are from non-preconditioned tissues connected to other deformable organs.

Chapter 6: Fracture mechanics of biological tissue

Fracture mechanics of soft biological tissue is analyzed based on energy balance between the external applied energy and the internal strain energy. In this case, liver tissue is highly nonlinear and non-uniform using the energy balance method allows the analysis in both linear and nonlinear.

6.1 Determination of fracture resistance

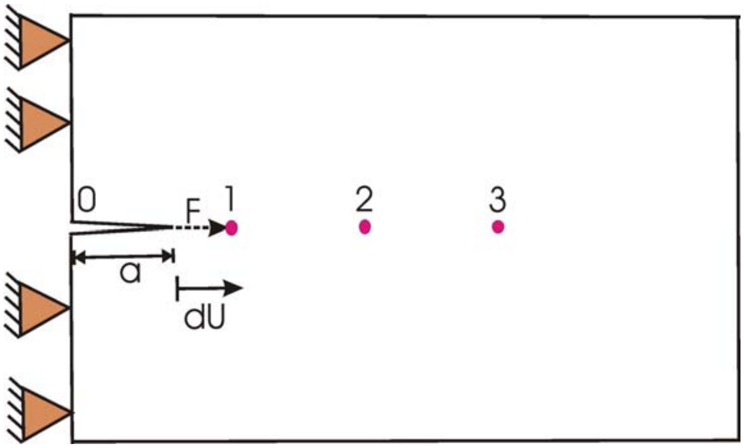

Figure 6.1: Schematic showing a liver specimen constrained at one end and the cutting path. Cutting starts from point 0, and proceeds to points 1, 2 and 3 etc. F denotes the force sensed at the blade, dU denotes an infinitesimal increment of blade displacement, and “a” denotes the current cut (crack) length.

Figure 6.1 shows schematically a liver specimen constrained at one end and the cutting path. Cutting starts from point 0, and proceeds to points 1, 2 and 3 etc. F denotes the force sensed at the blade, dU denotes an infinitesimal increment of blade displacement, and “a” denotes the current cut (crack) length.

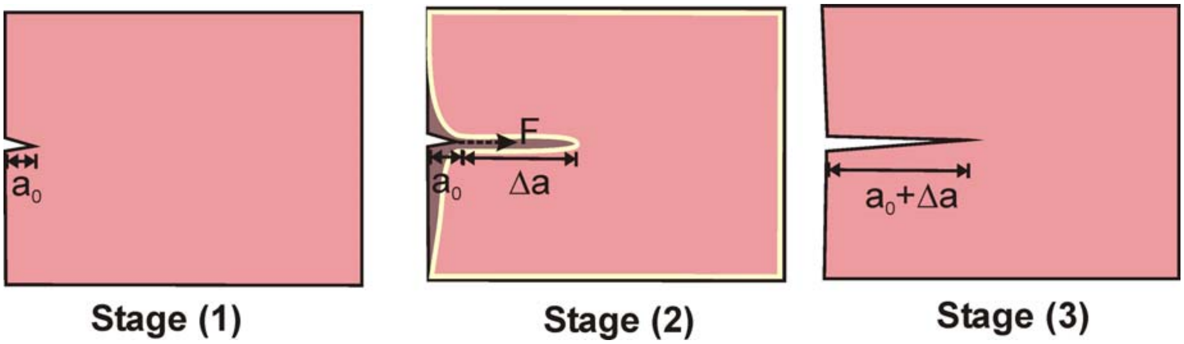

Figure 6.2: Three stages for modeling fracture resistance of soft deformable tissue

The fracture model was described by three stages starting from stage (1) which is the un-deform tissue. Stages (2) corresponded to the deformation of the tissue by the surgical blade. During this stage, the work done by the external force is stored as the internal strain energy stored in the liver specimen. Finally, at stage (3), the internal strain energy stored during tissue deformation in stage (2) is used up for fracture or crack growth.

Figure 6.2 shows the measured force versus the cut length (displacement of the blade). At stage(2) or during tissue deformation, at the instant when the cutting force “F” while the blade moves an additional infinitesimal displacement of dU, the increment of externally exerted work done dW_{ext} is given by:

$$dW_{ext} = FdU \text{..................................} (6.1)$$

The externally applied work to move the cutting blade from the starting point to a final point over a total displacement of length ‘a’ is

$$W_{ext} = \int dW_{ext} = \int_0^a FdU \text{......................} (6.2)$$

Graphically, W_{ext} is depicted by the area beneath the force versus displacement curve in Figure 6.2.

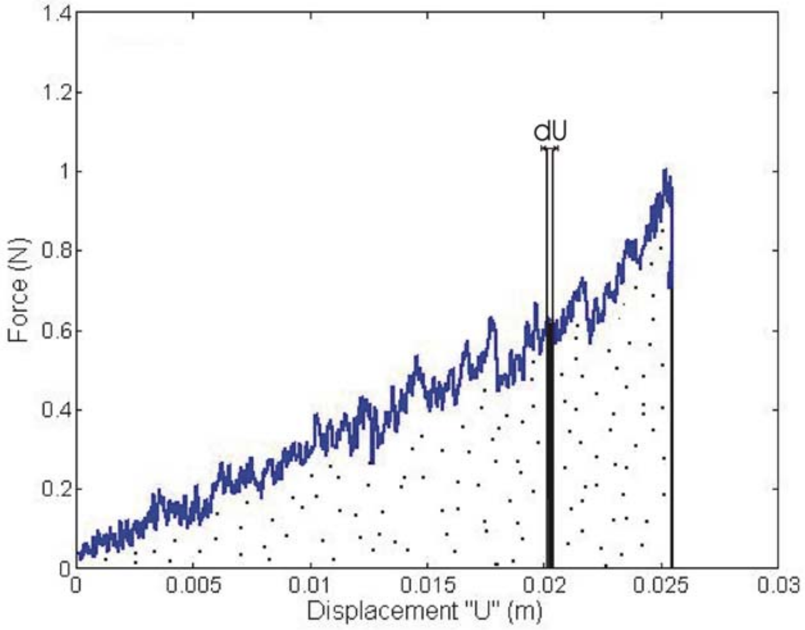

Figure 6.3: The measured force versus displacement (cut length) data during cutting

If we assume that all this externally applied work W_{ext} is used to pay for the fracture work (energy) barrier (stage 3) $W_{fracture}$ that is required to enable the crack (the cut) grow from zero length to the length of 'a', then

$$W_{fracture} = W_{ext} = \int_0^a FdU \text{.......................(6.3)}$$

The force F shown in Figure 6.3 is from raw experimental data where the blade was embedded at different depths in the soft tissue during cutting. We can normalize the magnitude F with the instantaneous depth of cut to obtain the normalized cutting force for a soft tissue sample of unit thickness. From the resulting plot, we can obtain the work of fracture for cutting a crack of length 'a' in a soft tissue sample of *unit* thickness, W^*. The resistance to fracture of the soft tissue, R, can be defined as the amount of required fracture work to cause a cut (crack) to extend for a unit length in a soft-tissue sample of unit thickness.

$$R = \frac{W^{*}_{fracture}}{a} \qquad \text{.................................}(6.4)$$

The resistance to fracture, R, is a measure of the materials resistance to the extension (propagation) of a crack. The fracture resistance of a material is frequently also labeled as the fracture *toughness* of the material.

6.2 Results

We performed 40 cutting experiments for various cutting lengths ranging from 0.5-4 inches. These experiments were designed to determine the magnitude of the fracture resistance (fracture toughness), and to study whether the fracture resistance in this soft tissue varies with the crack length (the length of cut) as is the case in some ductile engineered materials.

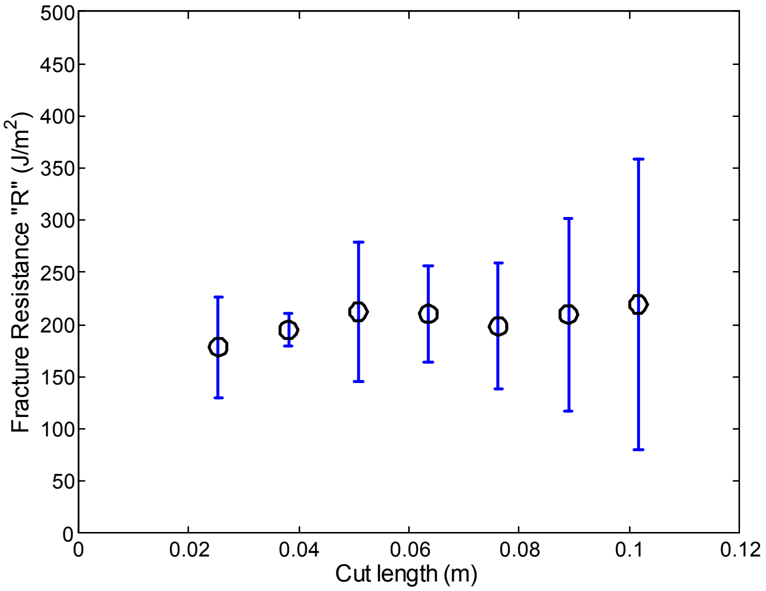

Figure 6.4: The relationship between cut length and the fracture resistance

Figure 6.4 and Table 6.1 depict results of the fracture resistance of 40 liver cuttings determined at various cut length ranging between 0.127-0.1016 m (0.5-4 inches). The results show that the magnitude of the average fracture resistance of the liver is ranging between 187

J/m^2 and 225 J/m^2. It is also apparent that the fracture resistance of this soft tissue is not sensitive to crack length.

Cut length		**Average fracture resistance “R” (J/m^2)**	**Standard deviation**
Inch	**m**		
1	0.0254	186.98	48.26
1.5	0.0381	201.72	13.67
2	0.0508	223.06	68.93
2.5	0.0635	216.64	47.24
3	0.0762	207.08	57.60
3.5	0.0889	215.39	93.35
4	0.1016	224.83	142.01

Table 6.1 The average fracture toughness and the standard deviation from 40 cutting experiments

Next we performed 10 experiments in each of which the blade traveled forward and backward for two cycles. In each experiment, we first let the blade move forward to cut the liver for 1 inch. After the blade moved forward and reached the specified cut length of one inch, the blade reversed its direction of travel and backward moved along the previous path to the starting point. In the backward (return) trip, the blade was not cutting but was traveling in the previously created one-inch “crack”.

After reaching the starting point, the blade then moved forward a second time ---- this time to travel forward for 2 inches. During this second forward travel, the blade first traveled for 1 inch in the previously-created “crack”, and then the blade cut for 1 inch in previously uncut liver tissue. At the end of the 2 inches travel, the blade stopped. The blade then reversed its direction of travel and returned to the starting point by traveling along the two-inch “crack” just created.

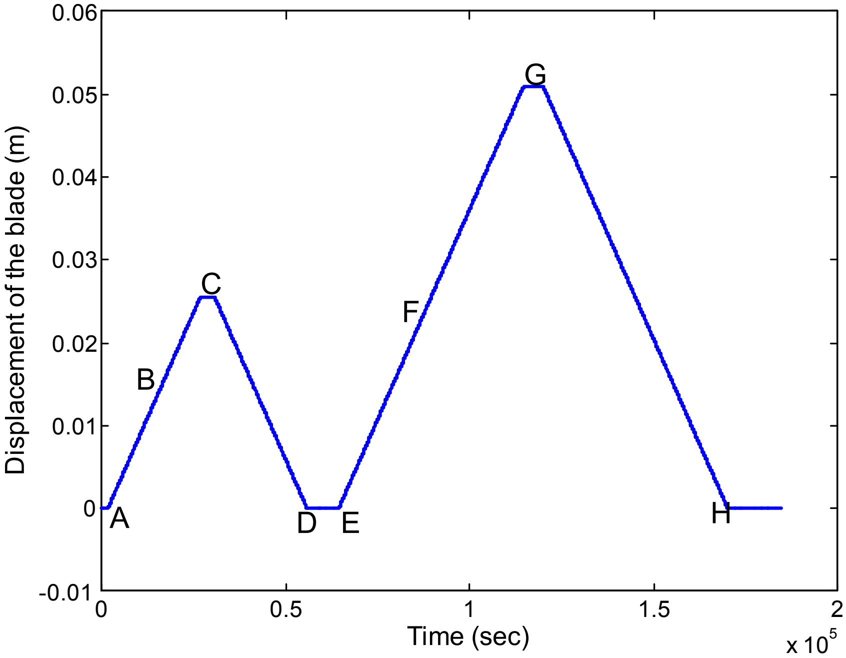

Figure 6.5: The travel profile of the displacement of the blade

Figure 6.5 shows the travel profile of the blade displacement. The corresponding force versus displacement profiles is portrayed in Figure 6.6 and 6.7. The red lines depict the first 1-inch loading-unloading (forward-backward movement) cycle. The blue curve corresponded to the second cycle with a travel distance of 2 inches. Figures 6.6 and 6.7 reveal two interesting features. During the return travel in the first cycle, the blade was traveling in a previously created crack, but there was still force sensed by the blade. Apparently, the crack surfaces were in contact with the blade surface and exerted frictional force on the blade.

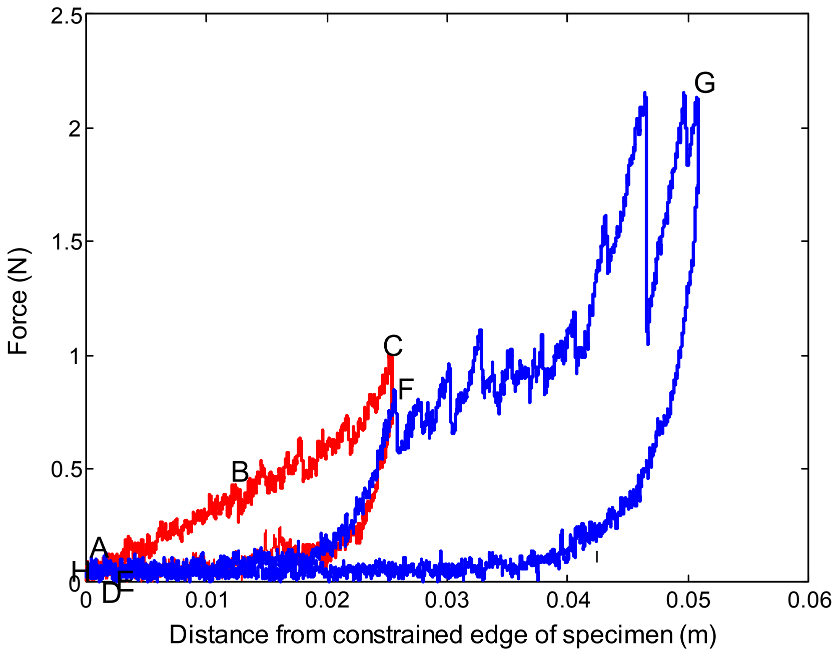

Figure 6.6 The force and displacement profiles during two cycles of forward-backward travel of the cutting blade.

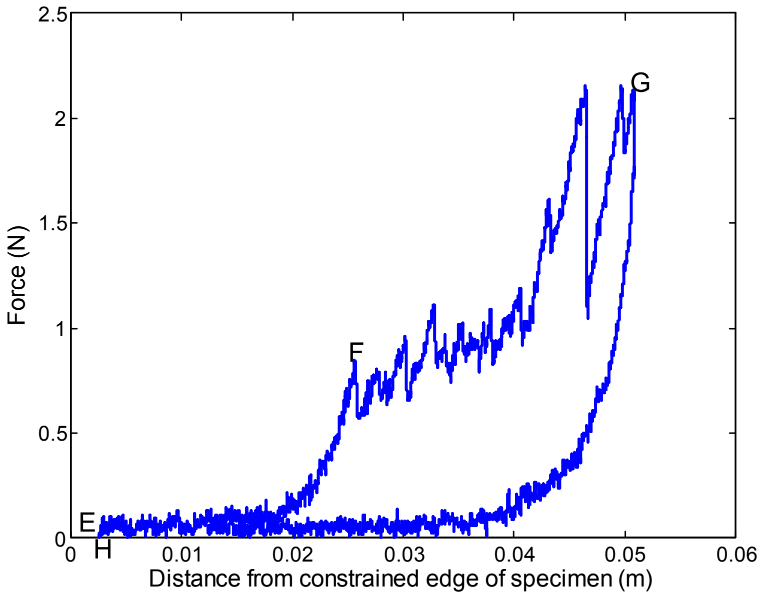

Figure 6.7: The force and displacement profile during the second cycle of the two forward-backward travel cycles of the cutting blade

In the second cycle, during the first inch of travel when the blade traveled forward in the crack, the blade experienced the same magnitude and variation of frictional force as it had experienced during the backward travel in the crack in the first cycle. After the first inch of travel in the crack, the force versus displacement curve reached approximately the unloading point of the first cycle. The subsequent cutting during the next inch of blade travel resulted in a loading force-displacement curve continuing approximately where the loading part of the first cycle left off.

To compare with previous work in determining fracture resistance of biological tissue, we summarized in table 6.2 the toughness of biological tissue found based on various method such as cyclic tension test and cutting with scissor. None of the previous work in the past studied fracture resistance of soft biological using scalpel cutting. We believe our work is the first to explore the tissue interaction with the scalpel blade.

Authors	Specimen	Test	Criterion	Linear/Nonlinear	Toughness (kJ/m²)
Doran etc.	Chicken skin	Cutting	energy	Linear	2.32±0.40
Mahvash etc.	Liver	Cutting	energy	Linear	n/a
Adeeb etc.	Tendon	tension(cyclic)	stress intensity	Linear	n/a
Pereira etc.	(four kinds)	Cutting	energy	Linear	(four values)
Oyen-Tiesma etc.	Cultured neocartilage	tension(cyclic)	energy	nonlinear (cycle by cycle)	0.32±0.17
Chin-Purcell etc.	Articular cartilage	tension(MSEN)	stress intensity	Linear	1.07±0.08
Chin-Purcell etc.	Articular cartilage	trouser tear	energy	Linear	1.10±0.29
Purslow etc.	rat skin	Tear	energy	nonlinear	19.5±1.99
Simha etc.	Cartilage	indentation/ penetration	energy	nonlinear	0.98±0.14

Table 6.2: Fracture resistance from various experiments

6.3 Discussion

We presented the experiments and methods to determine the fracture characteristics of soft deformable liver tissue in scalpel cutting. Using an energy balance approach to fracture mechanics, the resistance to fracture (the toughness) of the soft tissue was quantified by the measure R defined as the amount of mechanical work needed to extend the cut for a unit length in a soft-tissue sample of unit thickness. In this approach, the fracture resistance R incorporated the effects of all the physical mechanisms taking place in the cracking process. No simplifying assumptions such as those limiting the deformation to be small, linear and time-independent were used. The experiments and method **are applicable for all soft tissue.** The specific magnitude of the fracture resistance and its trend reported here were derived from experiments using pig liver for soft-tissue samples.

Chapter 7: Displacement field by tracking beads using C-arm fluoroscopes

To verify that our finite element model works properly, we performed an experiment to track the movement of the embedded beads inside the liver specimen during a particular cutting path. Dual C-arm fluoroscopes were used to capture the motion of the embedded radio-opaque markers inside the liver specimen. Fluoroscopy allows the real time image captured of the embedded beads and the motion was post analyzed using Matlab image processing toolbox.

7.1 Experimental Method

The cutting experiment was setup under the dual C-arm fluoroscopes for real time x-ray imaging. The C-arms were positioned in which the imaging planes were orthogonal to each other.

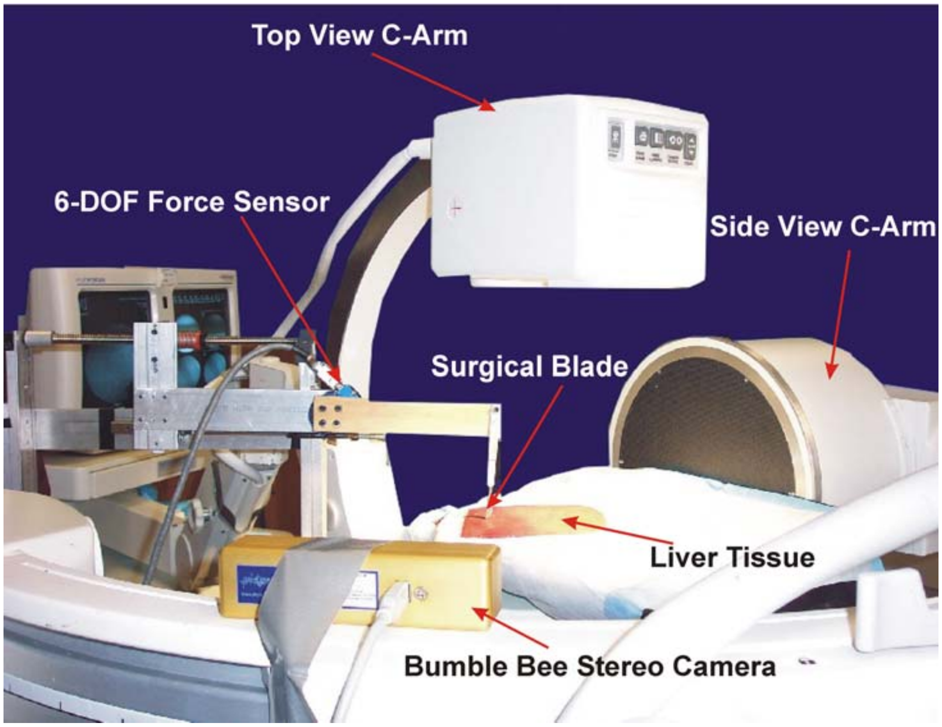

Figure 7.1: Experimental set up with dual C-arm fluoroscope

The video from each C-arm was captured onto a hard disk using a video capture device (Pinnacle Systems) at 29.97 frames per second at a resolution of 720x480 pixels. Before the experiment, the 1 mm diameter stainless steel beads were inserted into the specimen. The beads are radiopacity and the size along with the weight of the beads is small enough not to affect the property of the liver tissue. The pattern that the beads were inserted was a 7x14 grid and each bead is approximately 1 cm apart. The experimental set up along with the cutting machine is shown in Figure 7.1. The liver specimen was placed on a flat plate and clamped on one end of the specimen. It is necessary for the setup to be radiolucent therefore the clamp was held secure onto the tissue using surgical tape. The C-arms were used to image implanted markers inside the tissue on both top view and side view (Figure 7.2).

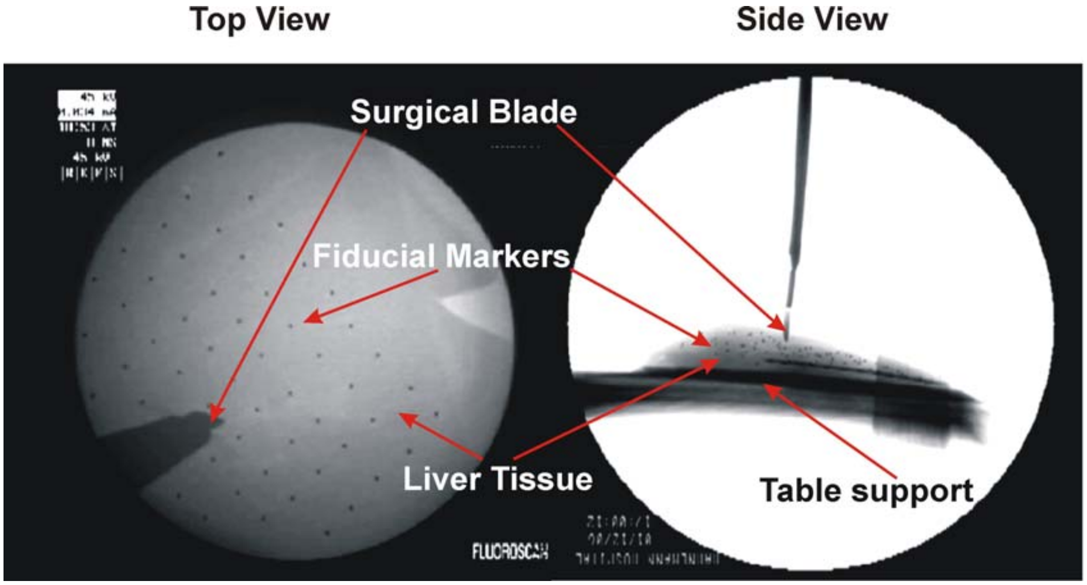

Figure 7.2: Images of the top and the side view of the liver specimen from C-arms fluoroscopes

After obtained the image from C-arm fluoroscope, we perform a sketch of the liver specimen from the side image. We used Pro Engineer to trace the profile of the liver specimen and obtained a solid model. The model was imported and meshed using ABAQUS finite element software. The images of the liver specimen along with the fiducials were shown in figure 7.2. To track the fiducial during a particular cutting experiment, the process was done through Matlab image processing toolbox.

7.2 Image calibration

To extract the accurate motion of the beads under the dual C-arm fluoroscopes, we have to take into account the two effects which are pincushion distortion and the magnification correction [11]. The accuracy of the image tracking based on C-arm images is suffered by the two main causes of distortions: the pincushion and S curve distortion. Pincushion distortion is a consequence of mapping of a flat surface onto a curved input phosphor of the image intensifier (detector). The S curve distortion is caused by the deflection of the electrons due to the earth's magnetic field and it is dependent on the angle of the image intensifier in the magnetic field. Both C-arm fluoroscopes for top view and side view were calibrated by imaging the calibration grid followed by determination of the distance from the centroid of the grid image (Figure 7.3-a) and the centroid of the pattern holes (red dot) at each location away from the center. The patter in the center of the image is undistorted and therefore the radial distance from the closest hole to the centroid was used as the true distance. The error was plotted versus the radial distance from the center of the image as shown in Figure 7.4.

To take into account the pincushion effect, the distance between the centroid of each red circle along the radius was measured (Figure7.3-a). The distance between two circles then was compared to the radius between the circle in the middle of the image and the closest circle (the true distance). As we moved along the radius outward the circular boundary, we found the error increased (due to distortion). The error between the distorted distance and true distance (Figure 7.4) was plotted and fitted with a polynomial curve fitting. For each C-arm fluoroscope, the equation for correction the pincushion distortion are as follow:

$$\text{Top view}: \quad y = 8(10^{-5})x^2 - 0.0079x + 0.4729 \tag{7.1}$$

$$\text{Side view}: \quad y = 6(10^{-4})x^2 - 0.0706x + 1.6171 \tag{7.2}$$

where y is the pixel errors and x is the radial distance from the image centroid.

a) Before pincushion correction

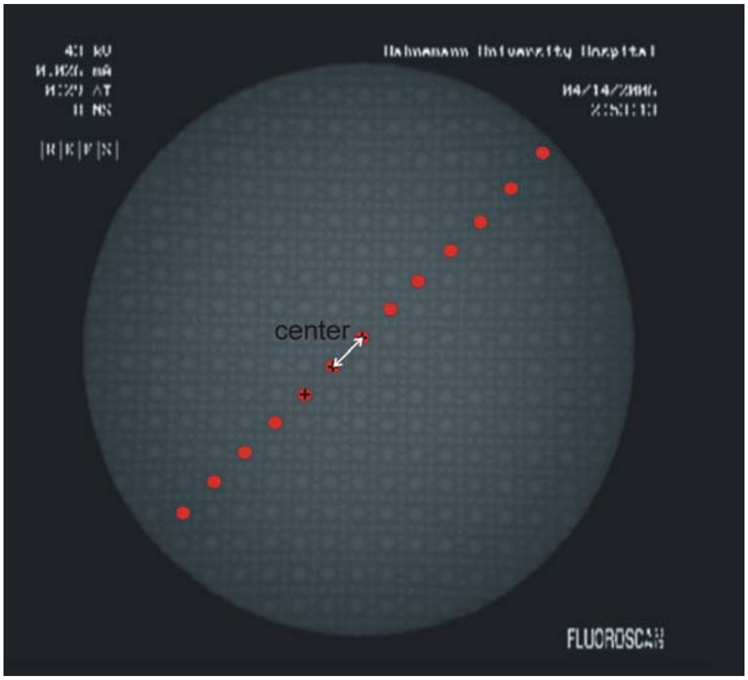

b) After pincushion

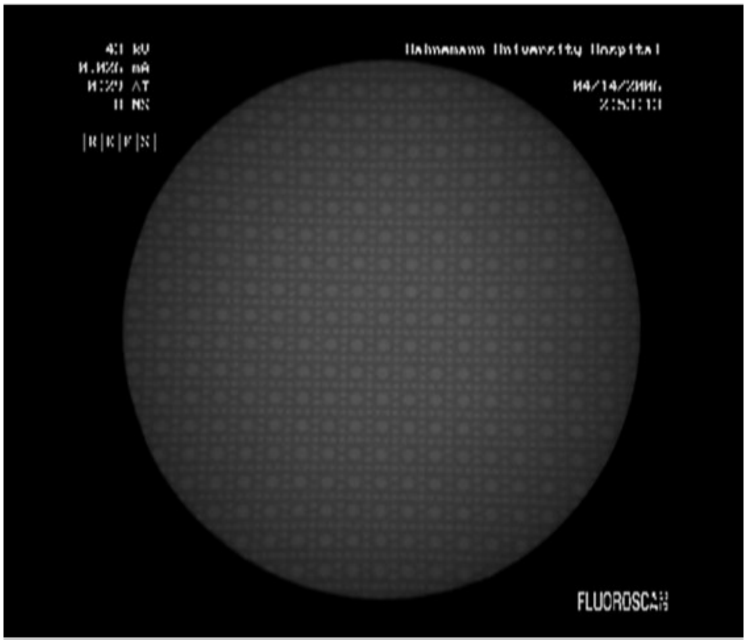

Figure 7.3: The grid images used during C-arm calibration a) the radial errors from the center of the imaged were used to perform the pincushion correction b) image after pincushion correction

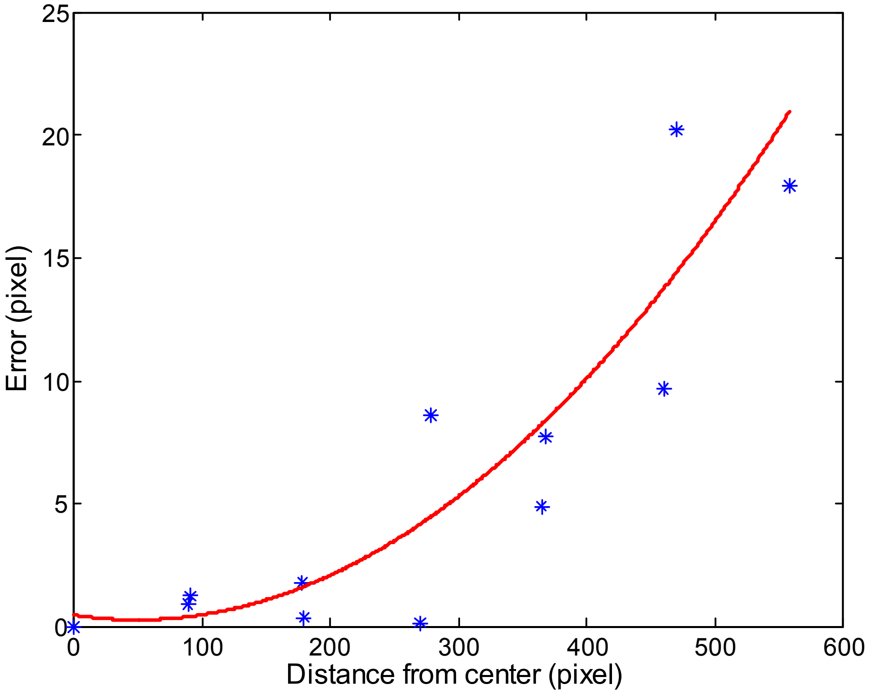

Figure 7.4: Polynomial fit between the error along the distance away from the centroid of the image for calibration of the top view C-arm

Each C-arm required separate correction for both pincushion distortion and the magnification. Magnification calibration of the C-arm fluoroscopes was done by imaging a radio-opaque ruler at various distances from the x-ray source. As for the distance from the x-ray source increases, the pixel to mm conversion was fit with linear (Figure 7.5) for the top view C-arm and a second order polynomial for the C-arm used for side view (OEC9600). Magnification calibration is as follow:

$$\text{Top view}: \quad m = -0.0008d + 0.3411 \qquad (7.3)$$

$$\text{Side view}: \quad m = 0.000784d^2 - 0.1093d + 5.1358 \qquad (7.4)$$

where m is the magnification of the image along with d which is the distance from the fluoroscope detector.

The correlation of the beads appeared in the images between the top view and the side view was done through the full rotation of the C-arm from 90 to 180 degrees. During the rotation, each bead was tracked as it moved in the image from the top view to the side view. The rotation was done prior to the cutting experiment.

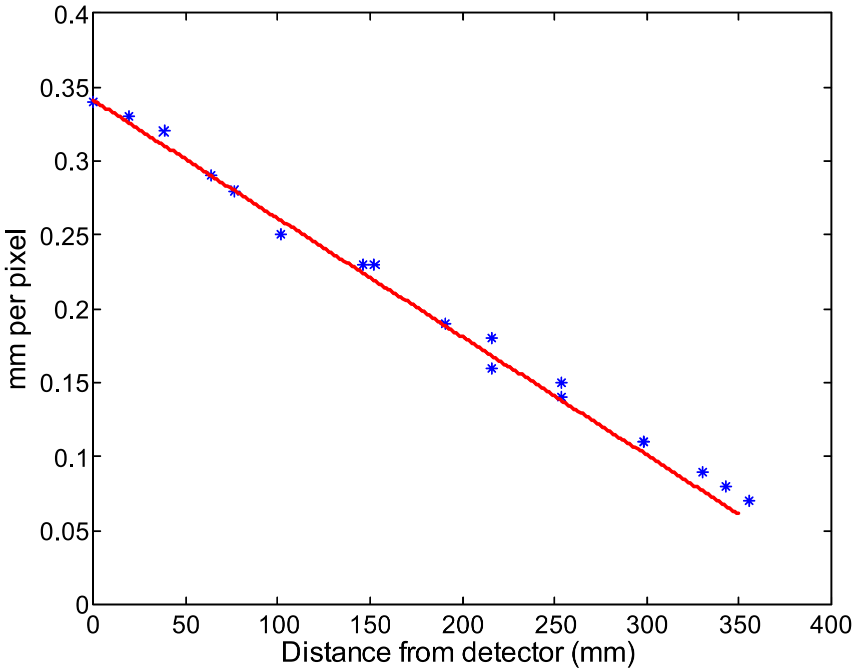

Figure 7.5: Linear fit of the magnification calibration for the C-arm at distance away from the x-ray source

After the registration and C-arm calibration, the cutting experiment was performed as described early in chapter 6. The depth of the cut was also observed through the Bumble Bee stereo camera system along with the force and displacement during the cutting process.

7.3 Result

The cutting experiment was done at 0.1cm/sec cutting speed at 90 degrees angle cutting. The real time x-ray images obtained from the C-arm was analyzed post experiment for the purpose of model verification. During a particular cutting experiment, the cutting force was segmented into each local deformation and followed by determination of the local effective modulus (LEM) as similar to what was done in Chapter 3.

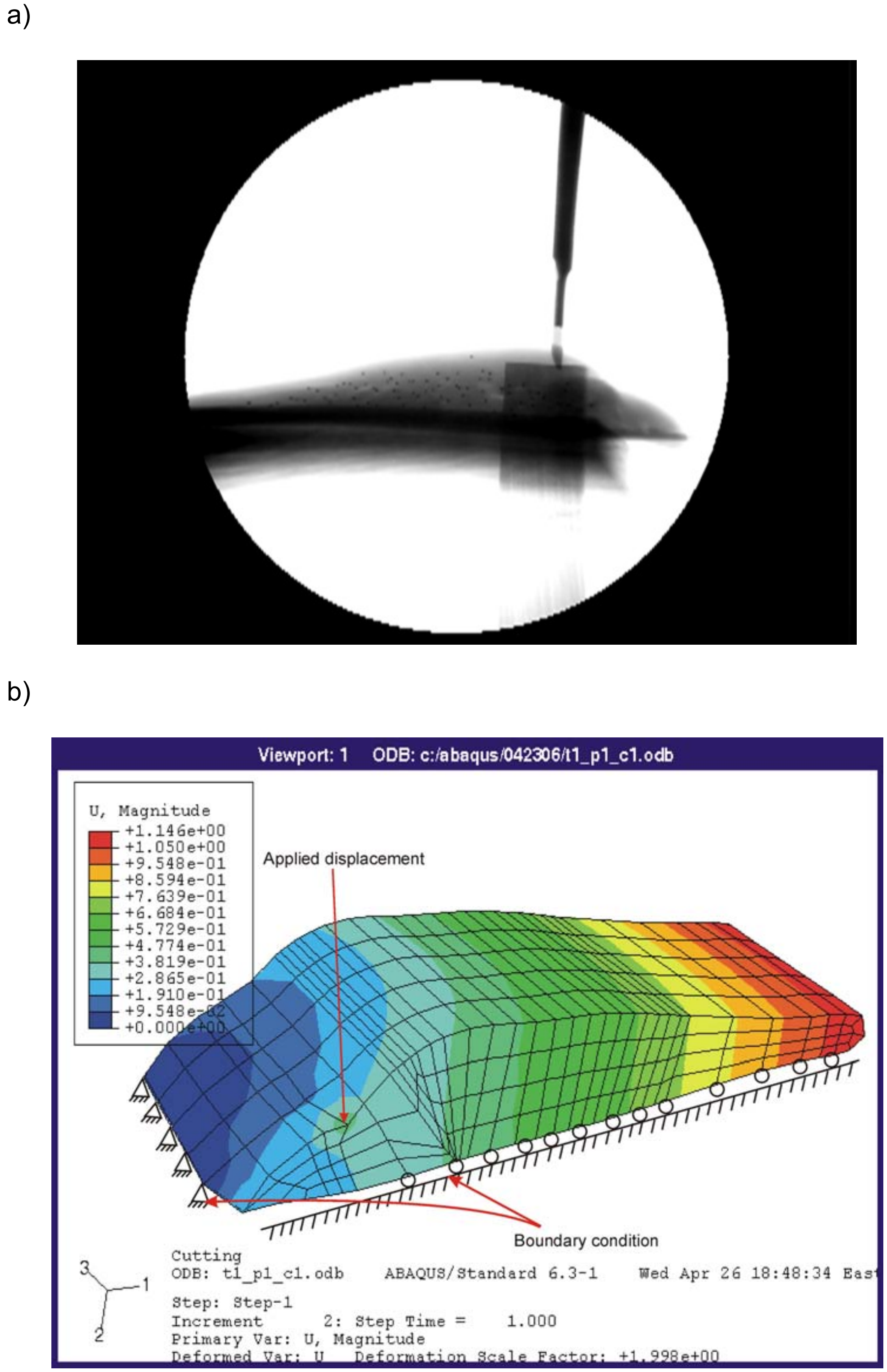

```
Cutting
ODB: t1_p1_c1.odb    ABAQUS/Standard 6.3-1    Wed Apr 26 18:48:34 Eas

Step: Step-1
Increment      2: Step Time =     1.000
Primary Var: U, Magnitude
Deformed Var: U   Deformation Scale Factor: +1.998e+00
```

Figure 7.6: a) Side view image of the liver specimen from the C-arm. b) Finite element model replicate half symmetric model of the liver specimen used in the experiment.

7.3.1 Finite element model

The finite element model used to determine the LEM was the replication of the liver specimen used during the experiment as was reconstructed through the images and Pro Engineering software. The model as rendered through the Pro-Engineering software was then imported to ABAQUS for meshing (Figure 7.6). The mesh used in the analysis is the 3D linear element. Since each deformation along a particular cutting path resulted in different LEM, the finished model was therefore partitioned into sections (Figure 7.7) as assigned the LEM as obtained from each local deformation.

Based on the finished model (Figure 7.7), the cutting force and displacement during of a particular deformation section from the cutting profile was applied to the model. The node displacement of the FE model was compared to the experimental observed displacement of the beads.

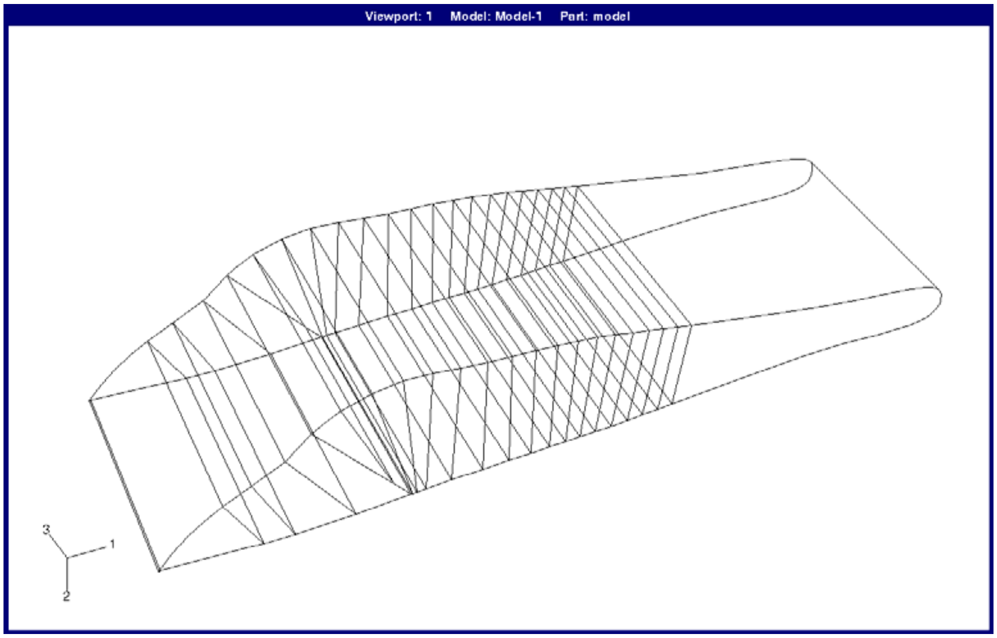

Figure 7.7: LEMs were assigned on each local deformation during a particular cutting path as the model was analyzed in ABAQUS

7.3.2 Bead movement based on C-arm images

The movement of the beads was observed through image analysis using Matlab imaging toolbox. Figure 7.8 shows the top view of a particular bead near the cutting path (in pixel) and the 3D view on the global coordinate (in centimeter) is shown in Figure 7.9.

Tracking the same bead in finite element model, the movement of the bead in x-y-z direction along with the magnitude plot is shown in Figure 7.10. The experimentally observed displacement is compared to the finite element displacement (Figure 7.11) shows the displacement of that particular bead is the same trend as the finite element calculation.

Figure 7.11 shows the experimentally observed bead displacement compared with the finite element model, while the results in table 7.1 shows the agreement between the experiment and the simulated results. As observed from table 7.1, beads closest to the cutting path appeared with the largest range of movement while the movement of beads farther away from the cutting path was less.

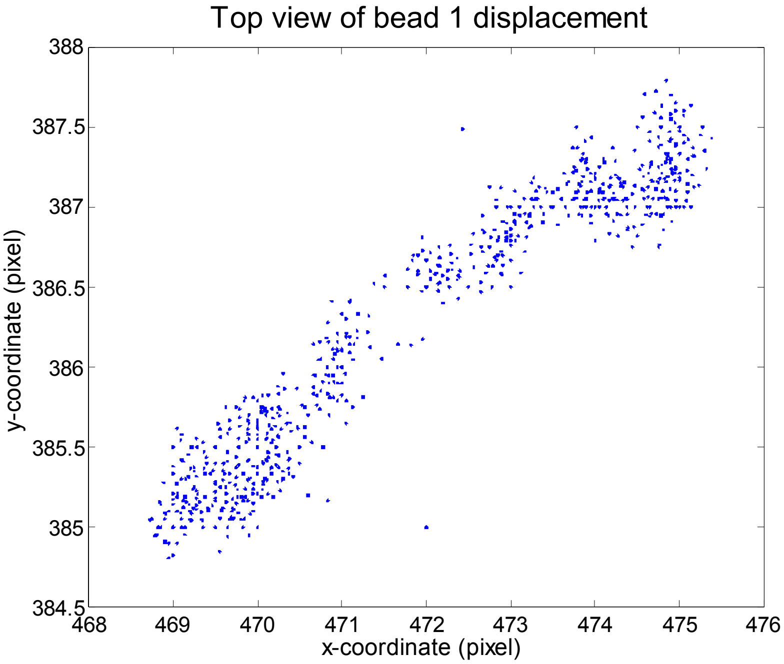

Figure 7.8: Top view of a particular bead during a cutting path of approximately 7cm

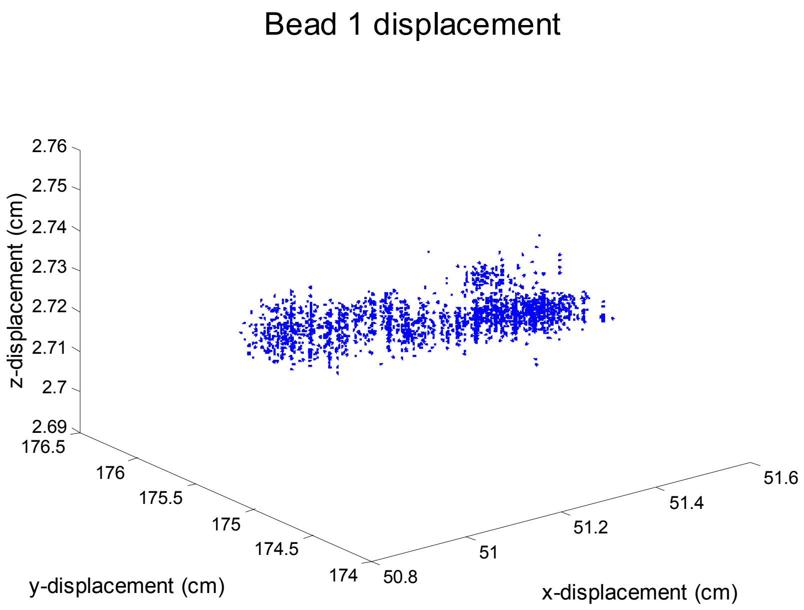

Figure 7.9: The movement of a bead as shown in x-y-z direction

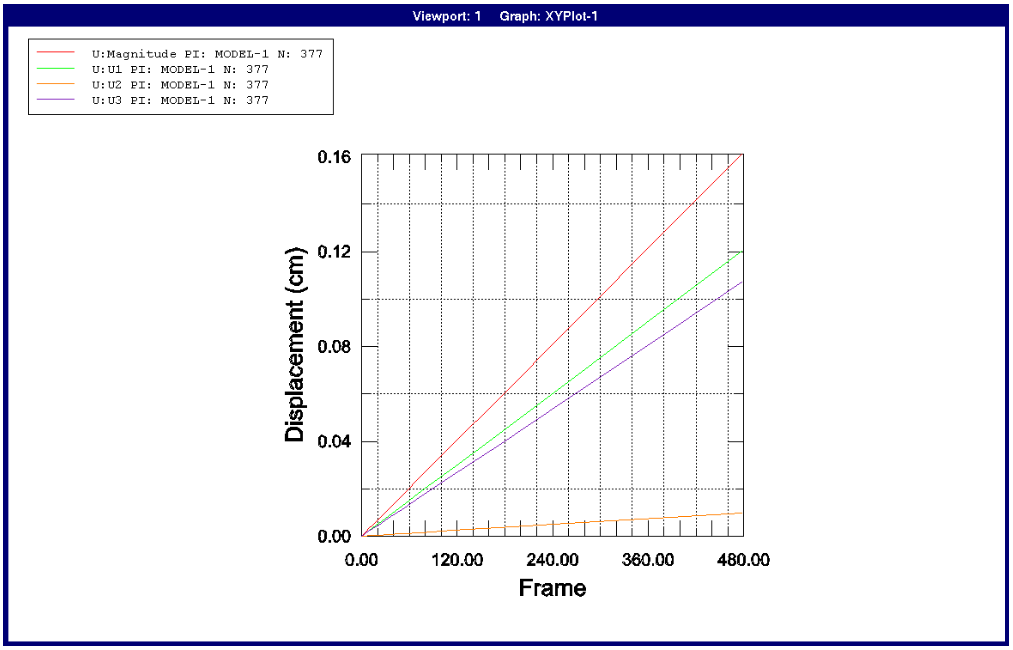

Figure 7.10: Displacement of a bead in x-y-z direction during a local deformation

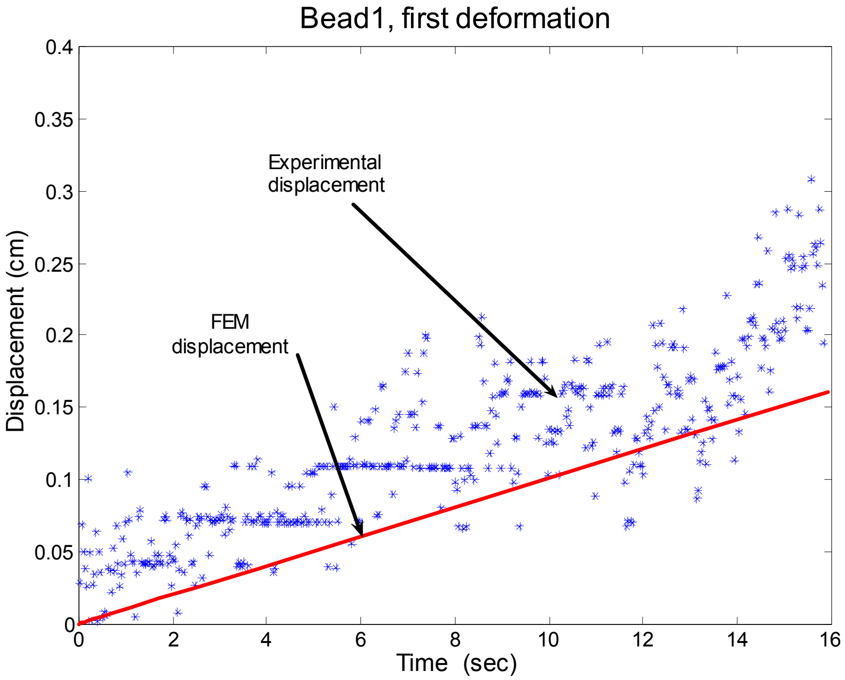

Figure 7.11: The experimental measured movement of the a bead during the first deformation section compared to FEM result

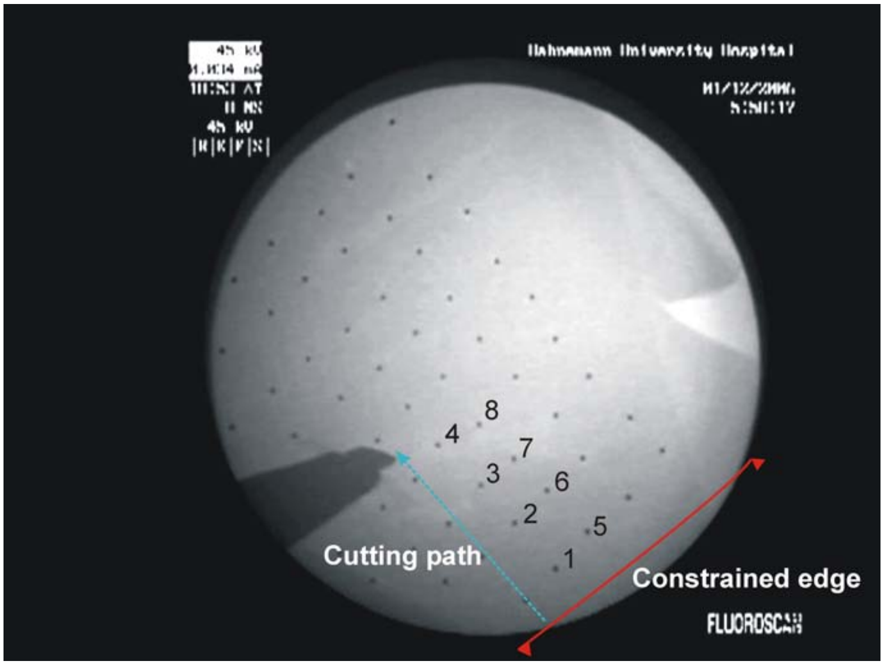

Figure 7.12: Schematic diagram for bead number

Bead #	FEM displacement (cm)	Experimental displacement (cm)
1	0.16	0.21
2	0.24	0.30
3	0.27	0.30
4	0.30	0.60
5	0.15	0.20
6	0.18	0.42
7	0.22	0.01
8	0.26	0.03

Table 7.1 Experimental and finite element simulated movement of the beads

7.4 Simplified model with the assigned LEM_{avg}

To prove the concept of applying the local effective modulus or the LEM In this part, we performed 6 cutting experiments at 0.1cm/sec cutting speed. Based on 5 cuts using the same pig liver, we determined the average LEM (LEM_{avg} = $81\text{x}10^3$ N/m^2). At the 6th cut, we determined the loading deformation sections to determine ΔF^{EXP} and ΔU^{exp} which are the change of force and the displacement. We applied ΔU^{exp} along with ABAQUS 2D model and the LEM_{avg} to simulate for the ΔF^{FEM} and compared that to ΔF^{EXP}.

As shown in Figure7.12-a, the normalized force versus displacement profile obtained from an experiment is relatively close to the forces determined through finite element model (ΔF^{FEM}) and LEM_{avg}. Then, we performed a cut on the liver specimen which obtained from different pig. Using the experimental normalized force and displacement profile, we compared to the result obtained from finite element model (Figure7.13-b) based on the same LEM_{avg}. The LEM based on the liver from the same pig (Figure7.13-a) is a better approximation compared to LEM a)

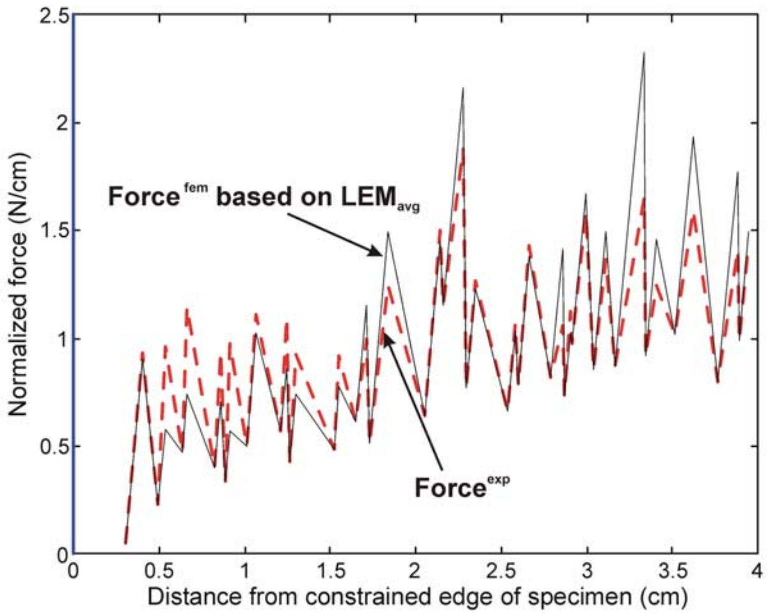

b)

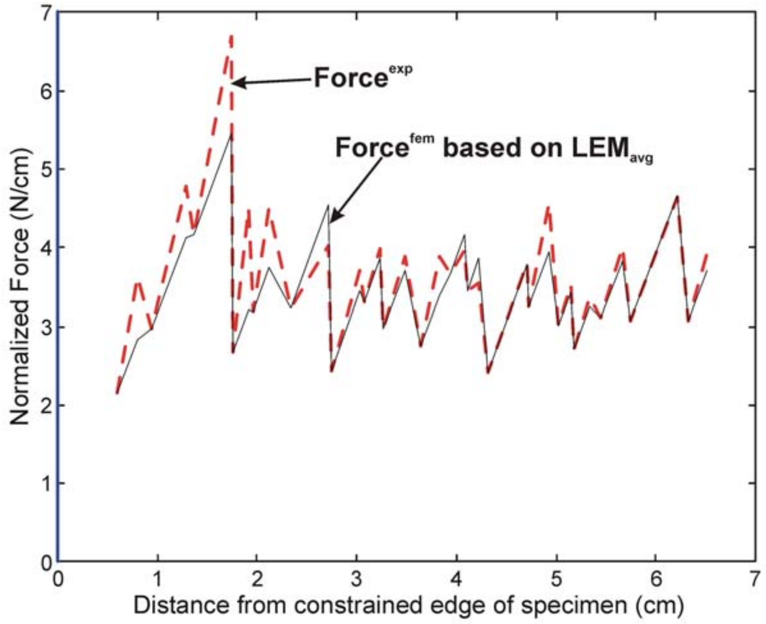

Figure 7.13: a) The plot of normalized force versus displacement of a particular cut compared to the simulated results based on LEM_{avg}. b) The plot of normalized force/displacement of a particular cut from different liver specimen compared to force/displacement profile obtained based on the LEM_{avg}.

determined from liver from different pig (Figure7.13-b). The F^{exp} and displacement profile matches better with the F^{FEM} and displacement profile when the specimen is from the same pig. This assures the property of the pig liver varied widely from one pig liver to another.

7.5 Discussion

Image analysis based on real-time x-ray image by dual C-arm fluoroscopes was used for tracking the beads inside the liver tissue during cutting experiment. The bead tracking is part of the model verification which shows the internal displacement field of the model compared to the experimental measured displacement.

Finally, we applied the average LEM determined from a liver specimen along with the displacement to the finite element model. The force computed based on average LEM appears to be relatively close to the force profile obtained from the experiment. This implies the average LEM from one liver specimen can be a good approximation for the global modulus of the same liver specimen.

Chapter 8: Concluding remarks and future works

Results from experiments reveal that the cutting force versus displacement curves exhibit a characteristic pattern: repeating units formed by a segment of linear loading (deformation of tissue) immediately followed by a segment of sudden unloading (localized crack extension in the tissue). This thesis addresses the characterization of the deformation resistance during the deformation segment and the fracture resistance during the localized crack extension segment. A local effective modulus (LEM) which is self-consistent with the finite element model has been computed to characterize the deformation resistance during the monotonic deformation segment of each repeating unit of the cutting force-displacement curve. This phenomenological measure of the apparent resistance to deformation lumps the overall effects of complex physical mechanisms of tissue deformation encountered by the cutting blade. It would be ideal if we can seek model the details of anisotropic elastic and visco-elastic responses, with time varying frictional-sliding contact, and incorporating locally large strains at tool-tissue interaction points (surface) and other physical mechanisms occurring in the soft tissue cutting process. However, with the current state of limited knowledge, it is prudent to proceed to build up one block at a time. We used the effective measure of apparent deformation resistance, the LEM, as a vehicle to enable using simple elastic finite element analysis to capture and reproduce the experimentally measured overall force-displacement characteristics caused by complex mechanisms.

For real-time or near-real-time medical simulation requiring accurate haptic feedback, it is important to have reality-based models that are fast (computationally non-intensive) but still preserve the actual overall force-displacement behavior. Several 3D and 2D finite element models with three levels of model order reduction were studied. These model order reductions simplify the internal complexities of the model while preserving the overall input-output (displacement-force) behavior. All these models can determine the local effective modulus equally well, and the results of the 3D model are bracketed by results from the 2D plane-stress model and 2D plane-strain model.

With regard to computation effort required, there is a significant difference among these models. The computation effort required for the 2D-quadratic-element model is one order of magnitude less than that required for the 3D-quadratic-element model. The computation effort for the 2D-linear-element model is two orders of magnitude smaller than that of the 3D-quadratic-element model.

Results show that the LEM varies with cutting speed and the angle of cut. The deformation resistance decreases as cutting speed increases. The deformation resistance varies linearly with cutting speed for 90^o cutting angle, and so does the results from 45^o cutting angle. For a fixed cutting speed, the resistance to deformation is lower at 45^o cutting angle than at 90^o cutting angle. This is consistent with visual observation that there was physically more tissue deformation encountered by the blade when the blade was perpendicular to the tissue surface (90^o cutting angle).

The values for LEM obtained with plane-stress finite element model and plane-strain finite element model were very close to each other, thereby justifying the use of a two-dimensional model to simulate a three dimensional process in reality. The deformation resistance as characterized via LEM can be used in future finite element models to simulate the deformation segment occurring prior to the onset each localized cut (crack) growth.

The local effective modulus (LEM) lumps the overall effects of complex physical mechanisms into one “effective” characterizing parameter. It is useful in tasks consistent with of its assumption: for computational models to capture and reproduce overall force-displacement characteristics as actually felt by the scalpel (or hand of the surgeon). It is however not appropriate to be used to discern the details of spatial distribution of local stress and strain field, the sliding friction-contact of tool-tissue interaction, and variation due to localized inhomogeneous and anisotropic tissue properties.

The finite element models developed can be used for Poisson's ratios covering the entire range of tissue compressibility. The actual compressibility of a soft tissue depends on the level of pressure applied and the condition of the tissue. Results for other Poisson's ratio can be routinely generated.

Finally, the concept of local effective modulus was verified through the internal beads tracking using dual C-arm fluoroscopes. The displacement of the beads embedded inside the liver specimen during a particular cutting path was compared to the displacement of the point node in finite element and the result shows a good approximation of the finite element which LEM was assigned.

8.1 Thesis contribution

- Developed cutting equipment which capable of real-time measuring of force and displacement along with an image processing algorithm to track the depth of cut during cutting experiment in real-time using stereo-vision for soft tissue characterization.
- Cutting soft tissue consists of sequence of local deformation followed by crack growth. The property of soft tissue is studied based on tool (surgical blade)-tissue interaction. The property "Local effective modulus" or the LEM is valid only local area and the property itself is consistent with the finite element model used to calculate the LEM.
- Reduced order finite element model is applicable for faster simulation for force feedback computation during surgical simulation. Along with that, 2D plane stress and plane strain models provide good approximation for 3D model.
- The resistance of the liver tissue to the cutting blade appeared to be less during faster cutting speed compared to slow cutting speed. In addition, cutting at 90 degrees blade/tissue angle result is less resistance.

- Fracture resistance of soft tissue was determined based on energy approach. The resistance to fracture of pig's liver tissue appeared to be independent of the crack length.
- Model verification was done using C-arm fluoroscopes. The displacement field determined through finite element model and the experimentally determined displacement of the beads prove that finite element model along with the local effective modulus could be used as a tool to determine the realistic force feedback during simulation.

8.2 Future work

The main focus of this thesis is on characterizing soft tissue during cutting. There are limitations of the work in this thesis. The local effective modulus (LEM) lumps the overall effects of complex physical mechanisms into one "effective" characterizing parameter. It is useful in tasks consistent with of its assumption: for computational models to capture and reproduce overall force-displacement characteristics as actually felt by the scalpel (or hand of the surgeon). It is however not appropriate to be used to discern the details of spatial distribution of local stress and strain field, the sliding friction-contact of tool-tissue interaction, and variation due to localized inhomogeneous and anisotropic tissue properties.

- The local effective modulus (LEM) of the liver tissue was determined by cutting it partially in the thickness dimension. The uncut layer located underneath the cutting path of the liver specimen affects the tissue resistance to the cutting blade. In this thesis, we did not take into account the influence of the uncut layer to the resistance of the liver tissue. Further study should consider taking into account the resistance of the liver tissue in the uncut layer or carefully examine the boundary criterion of the liver specimen while determining the LEM.

- To determine the local effective modulus, the analysis was done based on quasi-static analysis assuming the cutting speed is relatively slow. However, in real surgery, normal cutting speeds vary among surgeons. During the determination of the fracture resistance of the liver tissue, the cutting speed will appear in term of kinetic energy in the energy balance approach. Therefore, a further study should take into account the crack growth of liver tissue cutting at higher cutting speed.
- In order to determine the fracture resistance of the liver tissue, we performed the analysis based on quasi-static analysis, and total external force was used up as strain energy released during crack growth. These are reasonable assumptions while there is no proof that the assumption is true for all soft deformable tissue.
- The results reported here are from a pig liver sample without blood circulation. Results for a living tissue with blood circulation may differ. Further study should include comparison of the mechanical response of soft tissue samples without blood circulation with that from living tissue with blood circulation.
- Like many soft tissue, the real mechanical properties of liver is anisotropic. The degree of anisotropy depends on local microstructure and condition of the liver, and will vary from liver to liver. The actual force-displacement curve measured in the experiment has incorporated the real material response, but the model to determine LEM has not considered anisotropy. In a crude way, this LEM may be considered as a spatial average of the actual anisotropic moduli. More study needs be conducted if one wishes to discern anisotropic response of the liver.

List of References

1. Daigo Y, Masanori Y, Homa O, et al. A Comparison between electrocautery and scalpel plus scissor in breast conserving surgery. Oncology Reports 2003; 10:1729-1732.

2. Mendoza C, Laugier C. Tissue Cutting Using Finite Elements and Force Feedback. Lecture Notes in Computer Science 2003; 2673:175-182.

3. Cotin S, Delingette H, Ayache N. Real Time Elastic Deformations of Soft Tissue for Surgery Simulation. IEEE Transactions on Visualization and Computer Graphics 1999; 5(1):62-73.

4. Hirota K, Tanaka A, Kaneko T. Representation of force in cutting operation. Proceedings of IEEE Virtual Reality 1999:77.

5. Bruyns C, Ottensmeyer MP. Measurements of Soft-Tissue Mechanical Properties to Support Development of a Physically Based Virtual Animal Model. Proceedings of the Fourth International Conference on Medical Image Computing and Computer-Assisted Intervention 2002; 1:283-289.

6. Cotin S, Delingette H, Ayache N. A Hybrid Elastic Model allowing Real Time Cutting, Deformations and Force-Feedback for Surgery Training and Simulation. Virtual Computer journal 2000; 16(8):437-452.

7. Gopalakrishnan G, Devarajan V. StapSim: a virtual reality-based stapling simulator for laparoscopic hemiorrhaphy. Stud Health Technol Inform 2004; 98:111-3.

8. Szekely G, Brechbuhler C, Hutter R, et al. Modeling of Soft Tissue Deformation for Laparoscopic Surgery Simulation. Medical Image Analysis 2000; 4:57-66.

9. Seymour NE, Gallagher AG, Roman SA, et al. Virtual reality training improves operating room perfoamce: Results of a randomized, double-blined study. Annals of Surgery 2002; 236(4):458-464.

10. Okamura AM, Simone C, O'Leary MD. Force Modeling for Needle Insertion into Soft Tissue. IEEE Transactions on Biomedical Engineering 2004; 50(10):1707-1716.

11. Hing J, Brooks A, Desai JP. Reality-based estimation of Needle and Soft-tissue interaction for accurate haptic feedback in prostate brachytherapy simulation. International Symposium of Robotics Research. San Francisco, CA, 2005.

12. Hing JT, Brooks AD, Desai JP. Reality-Based Needle Insertion Simulation for Haptic Feedback in Prostate Brachytherapy. Accepted for publication at the IEEE International Conference on Robotics and Automation. Orlando, Florida, 2006.

13. Aloisio G, Barone L, Bergamasco M, et al. Computer-based simulator for catheter insertion training. Stud Health Technol Inform 2004; 98:4-6.

14. Alterovitz R, Pouliot R, Taschereau R, et al. Simulating Needle Insertion and Radioactive Seed Implantation for Prostate Brachytherapy. Medicine Meets Virtual Reality 11, Vol. 11, 2003. pp. 19-25.

15. DiMaio SP, Salcudean SE. Simulated interactive needle insertion. Proceedings of the 10th Symposium on Haptic Interfaces for Virtual Environment and Teleoperator Systems 2002:344-351.

16. DiMaio SP, Salcudean S. Needle insertion modeling and simulation. IEEE International Conference on Robotics and Automation, 2002. pp. 2098-2105.

17. Gobbetti E. Catheter Insertion Simulation with Co-registered Direct Volume Rendering and Haptic Feedback. Medicine Meets Virtual Reality 2000:96-98.

18. Gasson P, Lapeer RJ, Linney AD. Modeling Techniques for Enhanced Realism in an Open Surgery Simulation. Eight International Conference on Information Visualisation (IV'04). London, UK, 2004.

19. Hu J, Chang C-Y, Tardella N, et al. Effectiveness of Haptic Feedback in Open Surgery Simulation and Training System. Studies in Health Technology and Informatics 2005; 119:23-218.

20. Bielser D, Gross MH. Open surgery simulation. Stud Health Technol Inform 2002; 85:57-63.

21. Webster RW, Zimmerman DI, Mohler BJ, et al. A prototype haptic suturing simulator. Studies in Health Technology and Informatics 2001; 81:567-569.

22. Barba M, Fastenmeier K, Hartung R. Electrocautery: Principles and Practice. Journal of Endourology 2003; 17(8):541-555.

23. Walsh JT, Deutsch TF. Pulsed CO2 Laser Ablation of Tissue: Effect of Mechanical Properties. IEEE Transactions on Biomedical Engineering 1989; 36(12):1195-1201.

24. Fung YC. Biomechanics: Mechanical properties of living tissues. Second edition ed. New York: Springer-Verlag, 1993.

25. Fung YCB. Elasticity of soft tissues in simple elongation. American Journal of Physiology 1967; 213:1532-1544.

26. Nasseri S, Bilston LE, Phan-Thien N. Viscoelastic properties of pig kidney in shear, experimental results and modelling. Rheol Acta 2002; 41:180-192.

27. Miller K. Constitutive modeling of abdominal organs. Journal of Biomechanics 2000; 33:367-373.

28. Hu T, Desai JP. A biomechanical model of the liver for reality-based haptic feedback. Medical Image Computing and Computer Assisted Intervention (MICCAI). Montreal, Canada, 2003.

29. Kerdok AE. Soft Tissue Characterization: Mechanical Property Determination from Biopsies to Whole Organs. Whitaker Foundation Biomedical Research Conference 2001.

30. Miller K. Constitutive model of brain tissue suitable for finite element analysis of surgical procedures. Journal of Biomechanics 1999; 32:531-597.

31. Chui C, Kobayashi E, Chen X, et al. Combined compression and elongation experiments and non-linear modelling of liver tissue for surgical simulation. Medical & Biological Engineering & Computing 2004; 42:787-798.

32. Greenish S, Hayward V, Steffen T, et al. Measurement, Analysis and Display of Haptic Signals During Surgical Cutting. *Presence* 2002.

33. Dubois P, Thommen Q, Jambon AC. In Vivo Measurement of Surgical Gestures. IEEE Transactions on Biomedical Engineering 2002; 49(1):49-54.

34. Tay BK, Stylopoulos N, De S, et al. Measurement of in-vivo force response of intra-abdominal soft tissues for surgical simulation. Stud Health Technol Inform 2002; 85:514-9.

35. Ottensmeyer MP, Ben-Ur E, J.K. S. Input and Output for Surgical Simulation: devices to measure tissue properties in vivo and a haptic interface for laparoscopy simulators. Medicine Meets Virtual Reality 2000.

36. Ottensmeyer MP. In vivo measurement of solid organ viscoelastic properties. Medicine Meets Virtual Reality 2002; 2(10):328-333.

37. Hu T, Desai JP. Characterization of soft-tissue material properties: Large deformation analysis. Second International Symposium on Medical Simulation - Emerging Science|Enabling Technologies. Boston, MA, 2004.

38. Hu T, Desai JP. Modeling Large Deformation in Soft-tissues: Experimental results and Analysis. Eurohaptics. Germany, 2004.

39. Hu T, Desai JP. Soft-tissue material properties under large deformation: Strain rate effect. 26th Annual International Conference: IEEE Engineering in Medicine and Biology Society. San Francisco, CA, 2004.

40. Menciassi A, Scalari G, Eisinberg A, et al. An Instrumented Probe for Mechanical Characterization of Soft Tissues. Biomedical Microdevices 2001; 3(2):149-156.

41. Menciassi A, Eisinberg A, Scalari G, et al. Force feedback-based microinstruments for measuring tissue properties and pulse in microsurgery. IEEE International Conference on Robotics and Automation, Vol. 1, 2001. pp. 626-631.

42. Vacalebri P, Lazzarini R, Roccella S, et al. A Robotic System for Soft Tissue Characterization. Proceedings of the ICORR 2003 (The Eight International Conference on Rehabilitation Robotics). Kaist, Korea, 2003.

43. Nava A, Mazza E, Kleinermann F, et al. Evaluation of the mechanical properties of human liver and kidney through aspiration experiments. Technol Health Care 2004; 12(3):269-80.

44. Carter FJ, Frank TG, Davies PJ, et al. Measurements and modeling of the compliance of human and porcine organs. Medical Image Analysis 2001; 5:231-236.

45. Zhang M, Zheng YP, Mak AFT. Estimating the effective Young's modulus of soft tissues from indentation tests - nonlinear finite element analysis of effects of friction and large deformation. Medical Engineering and Physics 1997; 19(6):512-517.

46. Kerdok AE, Ottensmeyer MP, Howe RD. Effects of perfusion on the viscoelastic characteristics of liver. Journal of Biomechanics 2006; In Press.

47. Greenleaf JF, Fatemi M, Insana M. Selected Methods for Imaging Elastic Properties of Biological Tissues. Annual Review of Biomedical Engineering 2003; 5:57-78.

48. d'Aulignac D, Balaniuk R, Laugier C. A Haptic Interface for a Virtual Exam of the Human Thigh. Proceedings of the IEEE International Conference on Robotics & Automation 2000:2452-2456.

49. Kennedy CW, Hu T, Desai JP. Combining Haptic and Visual Servoing for Cardiothoracic Procedures. IEEE International Conference on Robotics and Automation. Washington D. C., 2002.

50. Kennedy CW, Hu T, Desai JP, et al. A Novel approach to Robotic Cardiac Surgery using Haptics and Vision. Cardiovascular Engineering: An International Journal, 2002 2002.

51. Brouwer I, Ustin J, Bentley L, et al. Measuring In Vivo Animal Soft Tissue Properties for Haptic Modeling in Surgical Simulation. Medicine Meets Virtual Reality 2001; 2001:69-74.

52. Kerdok AE, Cotin SM, Ottensmeyer MP, et al. Truth cube: Establishing physical standards for real time soft tissue simulation. Medical Image Analysis 2003; 7:283-291.

53. Arbogast KB, Thibault KL, Pinheiro BS, et al. A High-Frequency shear device for testing soft biologicial tissues. Journal of Biomechanics 1997; 30(7):757-759.

54. Manduca A, Lake DS, Ehman RL. Spatio-Temporal Directional Filtering for Improved Inversion of MR Elastography Images. Proceedings of the Fifth International Conference on Medical Image Computing and Computer Assisted Intervention, 2002. pp. 293-299.

55. Halperin HR, Tsitlik JE, Gelfand M, et al. Servo-Controlled Indenter for determining the transverse stiffness of ventricular muscle. IEEE Transactions on Biomedical Engineering 1991; 38(6):602-607.

56. Dokos S, LeGrice JJ, Smaill BH. A Triaxial-Measurement Shear-Test Device for Soft Biological Tissues. Journal of Biomechanical Engineering 2000; 122:471-478.

57. LeGrice IJ, Takayama Y, Covell JW. Transverse Shear Along Myocardial Cleavage Planes provides a mechanism for normal systolic wall thickening. Circulation Research 1995; 77:182-193.

58. Ho CB, Srinivasan MA, Small SD, Dawson SL. Force Interaction in Laparoscopic Simulation: Haptic Rendering Soft Tissues. Medicine Meets Virtual Reality, 1998.

59. Picinbono G, Delingette H, Ayache N. Nonlinear and anisotropic elastic soft tissue models for medical simulation. Proceedings of the IEEE International Conference on Robotics and Automation 2001; 2:1370-1375.

60. Bielser D, Gross MH. Interactive Simulation of Surgical Cuts. Proceedings of Pacific Graphics 2000, IEEE Computer Society Press 2000:116-125.

61. Greenish S. Acquisition and Analysis of Cutting Forces of Surgical Instruments for Haptic Simulation. Department of Electrical and Computer Engineering: McGill University, 1998.

62. Chial V, Greenish S, Okamura AM. On the Display of Haptic Recordings for Cutting Biological Tissues. IEEE Virtual Reality (Haptics Symposium) 2002.

63. Tholey G, Chanthasopeephan T, Hu T, et al. Measuring Grasping and Cutting Forces for Reality-Based Haptic Modeling. Computer Assisted Radiology and Surgery. London, UK, 2003.

64. Terzopoulos D, Fleischer K. Modeling inelastic deformation: viscoelasticity, plasticity, fracture. In Computer Graphics (SIGGRAPH '88 Proceedings), Vol. 22, 1988. pp. 269-178.

65. Mahvash M, Hayward V. Haptic Rendering of Cutting: A Fracture Mechanics Approach. Haptics-e, The Electronic Journal of Haptics Research (www.haptics-e.org) 2001; 2(3).

66. Srinivasan MA. Surface deflection of primate fingertip under line load. Journal of Biomechanics 1989; 22(4):343-349.

67. Basdogan C, Ho C, Srinivasan MA, et al. Force Interaction in Laparoscopic Simulation: Haptic Rendering Soft Tissues. Medicine Meets Virtual Reality 1998.

68. Dachille F, Qin H, Kaufman A, El-sana J. Haptic sculpting of dynamic surfaces. ACM Symposium of Interactive 3D graphics, 1999.

69. Edwards J, Luecke G. Physically based models for use in a force feedback virtual environment. Japan/USA Symposium on Flexible Automation, 1996. pp. 221-228.

70. Cover SA, Ezquerra NF, O'Brien J, et al. Interactively deformable models for surgery simulation. IEEE Computer Graphics and Applications 1993:65-78.

71. Lee Y, Terzopoulos D, Waters K. Realistic modeling for facial animation. Proceedings of the SIGGRAPH, 1995. pp. 55-62.

72. Ng HN, Grimsdale RL. Computer graphics techniques for modeling cloth. IEEE Computer Graphics and Applications 1996; 16:28-41.

73. Bathe K. Finite Element Procedures. Englewood Cliffs: Prentice Hall, 1996.

74. Cotin S, Delingette H, Clement J-M, et al. Geometric and Physical representations for a simulator for hepatic surgery. In Proceedings of Medicine meets Virtual Reality IV: IOS Press, 1996. pp. 139-151.

75. Basdogan C, Ho C, Srinivasan MA. Virtual environments for medical training: Graphical and Haptic simulation of common bile duct exploration. IEEE/ASME Transactions on Mechatronics 2001; 6(3):267-285.

76. James D, Pai D. ARTDEFO: Accurate real time deformable objects. Computer Graphics (SIGGRAPH), 1999.

77. De S, Kim J, Srinivasan MA. A meshless numerical technique for physically based real-time medical simulations. Medicine meets virtual reality, 2001. pp. 113-118.

78. Bro-Nielsen M. Fast Finite Elements for Surgery Simulation. Proceedings of Medicine Meets Virtual Reality V, 1997. pp. 395-400.

79. Bro-Nielsen M, Cotin S. Real time volumetric deformable models for surgery simulation using finite elements and condensation. Computer Graphics Forum 1996; 15(3):57-66.

80. Zhuang Y, Canny J. Real-time simulation of physically realistic global deformation. SIGGRAPH99 Sketches and Applications. Los Angeles, CA, 1999.

81. De S, Hong JW, Bathe KJ. On the method of finite spheres in applications: towards the use with ADINA and a surgical simulator. Computational Mechanics 2003; 31:27-37.

82. Zhuang Y, Canny J. Haptic interaction with global deformations. Proc. 2000 IEEE Internat. Conf. Robotics and Automation, 2000. pp. 2428-2433.

83. Gibson S, Samosky J, Mor A, et al. Simulating Arthroscopic Knee Surgery using Volumetric Object Representations, Real-Time Volume Rendering and Haptic Feedback.

84. Kauer M, Vuskovic V, Dual J, et al. Inverse Finite Element Characterization of Soft Tissues. Medical Image Analysis 2002; 6:275-287.

85. Moulton MJ, Creswell LL, Actis RL, et al. An Inverse Approach to Determining Myocardial Material Properties. Journal of Biomechanics 1995; 28(8):935-948.

86. Basdogan C, De S, Kim J, et al. Haptics in Minimally Invasive Surgical Simulation and Training. IEEE Computer Graphics and Applications 2004:56-64.

87. Anderson TL. Fracture Mechanics: Fundamentals and Applications. 2nd edition ed: CRC Press, 1994.

88. Doran CF, McCormack BAO, Macey A. A Simplified Model to Determine the Contribution of Strain Energy in the Failure Process of Thin Biological Membranes during Cutting. Strain International Journal for Strain Measurement 2004; 40(4):173.

89. Oyen-Tiesma M, Cook RF. Technique for estimating fracture resistance of cultured neocartilage. Journal of Materials Science: Material in Medicine 2001; 12:327-332.

90. Purslow PP. Fracture of non-linear biological materials: some observations from practice relevant to recent theory. Journal of Physics D: Applied Physics 1989; 22(6):854-856.

91. Kendall K, Fuller KNG. J-Shaped stress/strain curves and crack resistance of biological materials. Journal of Physics D: Applied Physics 1987; 20:1596-1600.

92. Atkins AG, Mai YW. Elastic and Plastic Fracture: metals, polymers, ceramics, composites, biological materials: Ellis Horwood Limited, 1985.

93. Darvell BW, Lee PKD, Yuen TDB, Lucas PW. A portable fracture toughness tester for biological materials. Measurement Science and Technology 1996; 7:954-962.

94. Pereira BP, Lucas PW, Swee-Hin T. Ranking the Fracture Toughness of Thin Mammalian Soft Tissue Using the Scissors Cutting Test. Journal of Biomechanics 1997; 30(1):91-94.

95. Ahsan T, Sah RL. Biomechanics of integrative cartilage repair. Journal of OsteoArthritis Research Society International 1999; 7:29-40.

96. Chin-Purcell MV, Lewis JL. Fracture of Articular Cartilage. Journal of Biomechanical Engineering 1996; 118:545-555.

97. Adeeb SM, Zec ML, Thornton GM, et al. A Novel Application of the Principles of Linear Elastic Fracture Mechanics (LEFM) to the Fatigue Behavior of Tendon Tissue. Journal of Biomechanical Engineering 2004; 126:641-650.

98. Simha NK, Carlson CS, Lewis JL. Evaluation of fracture toughness of cartilage by micropennetration. Journal of Materials Science: Material in Medicine 2003; 12:631-639.

99. Bruyns CD, Montgomery K. Generalized Interactions Using Virtual Tools Within the Spring Framework: Probing, Piercing, Cauterizing, and Ablating. Medicine Meets Virtual Reality (MMVR02). Newport Beach, CA, 2001.

100. Nienhuys H, van der Stappen F. Interactive needle insertions in 3D nonlinear material. 2003.

101. Gray H. Gray's Anatomy: General Publishing Co. Ltd., 1901.

102. Fung YC. Biomechanics: Mechanical Properties of Living Tissues. 1 ed. New York Heidelberg Berlin: Springer-Verlag, 1981.

Appendix A

Plane stress and Plane strain model

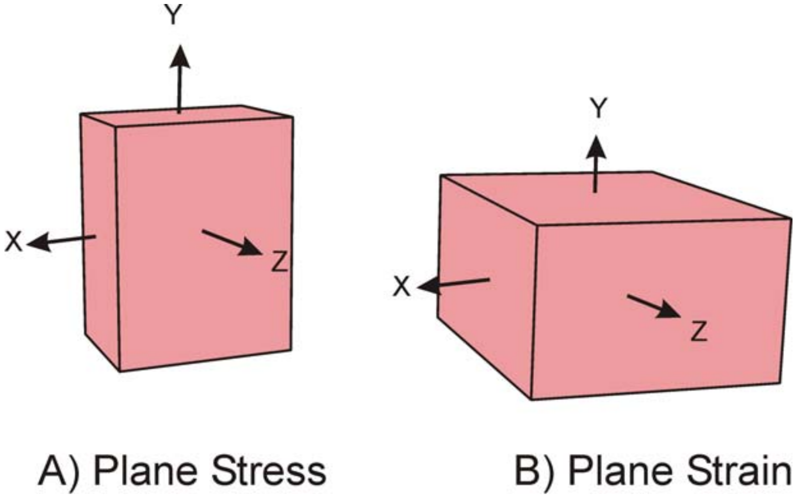

In case of the material is isotropic and is described by the Young's modulus of "E" and Poisson's Ratio of "v".

Plane stress is suitable for thin specimen because the through thickness is small. The stress in the through thickness direction cannot vary (σ_{zz} , σ_{yz} , σ_{xz} = 0). The stiffness matrix of plane stress is given by:

$$\begin{bmatrix} \sigma_{xx} \\ \sigma_{yy} \\ \sigma_{xy} \end{bmatrix} = \frac{E}{1-\upsilon^2} \begin{bmatrix} 1 & \upsilon & 0 \\ \upsilon & 1 & 0 \\ 0 & 0 & 1-\upsilon \end{bmatrix} \begin{bmatrix} \varepsilon_{xx} \\ \varepsilon_{yy} \\ \varepsilon_{xy} \end{bmatrix}$$

Plane strain is good for thick specimen. The body is constrained in the z direction which implies e_{zz}, e_{xz}, e_{yz} = 0. The stiffness matrix for plane strain is:

$$\begin{bmatrix} \sigma_{xx} \\ \sigma_{yy} \\ \sigma_{xy} \end{bmatrix} = \frac{E}{(1+\upsilon)(1-2\upsilon)} \begin{bmatrix} 1-\upsilon & \upsilon & 0 \\ \upsilon & 1-\upsilon & 0 \\ 0 & 0 & 1-2\upsilon \end{bmatrix} \begin{bmatrix} \varepsilon_{xx} \\ \varepsilon_{yy} \\ \varepsilon_{xy} \end{bmatrix}$$

Appendix B

Compressible versus Incompressible material

The displacement based finite element method is a simple and yet effective way to solve. However, in the case of incompressible material and the analysis of plates and shells, the displacement-based finite element is not sufficiently effective.

Poisson's ratio represents material property in term of compressible and incompressible. The Poisson's ratio usually varies between –1 to 0.5. Most steel has Poisson's ratio of 0.33 and completely incompressible has Poisson's ratio of 0.5.

Vita

Teeranoot Chanthasopeephan (citizen of Thailand)

Education

Drexel University, Philadelphia, PA, USA	2006
Doctor of Philosophy in Mechanical Engineering and Mechanics	
Advisors: Dr. Jaydev P. Desai and Dr. Alan C.W Lau	
University of Michigan, Ann Arbor, MI, USA	
Master of Science in Mechanical Engineering	2001
University of Pennsylvania, Philadelphia, PA, USA	
Bachelor of Science in Mechanical Engineering	2000
Minor: Mathematics	

Awards and Honors

• Link Foundation Fellowship for Advanced simulation	2005-2006
• Royal Thai Government Scholar	1995-2005
• Graduate Student Research award, College of Engineering, Drexel University	2005
• Poster Award for Emerging Technology (Honorable Mention) Drexel University Research Day	2004,2005
• The William K. Gemill Memorial Award for Outstanding Creativity in an Engineering Design Project Mechanical Engineering Department, University of Pennsylvania	2000

Publications

Archival Journals:

1) **Teeranoot Chanthasopeephan**, Jaydev P. Desai, and Alan C.W. Lau, "Measuring Forces in Liver Cutting: New Equipment and Experimental Results," Annals of Biomedical Engineering, 2003 Dec; 31(11): 1372-82.

2) **Teeranoot Chanthasopeephan**, Jaydev P. Desai, and Alan C.W. Lau, "Modeling Soft-Tissue Deformation prior to Cutting for Surgical Simulation: Finite Element Analysis and Study of Cutting Parameter", IEEE Transactions on Biomedical Engineering, (Accepted for publication).

Conference Proceedings:

1) **Teeranoot Chanthasopeephan**, Jaydev P. Desai and Alan C.W. Lau, "Determining Fracture Characteristics in Scalpel Cutting of Soft Tissue," *Biorob2006, Pisa, Italy, February 20-22, 2006*

2) **Teeranoot Chanthasopeephan**, Jaydev P. Desai, and Alan C.W. Lau, "3D and 2D Finite Element Analysis in Soft Tissue Cutting for Haptic Display," *The 12th International Conference on Advanced Robotics (ICAR) Seattle, Washington, USA, July 18th-20th, 2005*

3) **Teeranoot Chanthasopeephan**, Jaydev P. Desai, and Alan C.W. Lau, "Determining Deformation Resistance in Cutting Soft Tissue with Non-Uniform Thickness," *26th Annual International Conference of the IEEE Engineering in Medicine and Biology Society, San Francisco, CA, 2004*

4) **Teeranoot Chanthasopeephan**, Jaydev P. Desai, and Alan C.W. Lau, "Deformation Resistance in Soft Tissue Cutting: A Parametric Study," *The 12th Symposium on Haptic interfaces for virtual environment and teleoperator systems, Chicago IL, March 2004*

5) **Teeranoot Chanthasopeephan**, Jaydev P. Desai, and Alan C.W. Lau, "Study of Soft Tissue Cutting Forces and Cutting Speeds," *The 12th Annual Medicine Meets Virtual Reality Conference, Newport Beach CA January 15-17 2004*

6) **Teeranoot Chanthasopeephan**, Jaydev P. Desai, and Alan C.W. Lau, "Measuring Forces in Liver Cutting for Reality-Based Haptic Display," *International Conference of Intelligent Robots and Systems (IROS), Las Vegas, Nevada October 27-31 2003.*

7) Gregory Tholey, **Teeranoot Chanthasopeephan**, Tie Hu, Jaydev P. Desai, and Alan C.W. Lau, "Measuring Grasping and Cutting Forces for Reality-Based Haptic Modeling," *Computer Assisted Radiology and Surgery, 17th International Congress and Exhibition, London U.K, June 25-28 2003*